This is to certify that the
dissertation entitled

ELECTROMAGNETIC MATERIAL CHARACTERIZATION OF A PEC BACKED LOSSY SIMPLE MEDIA USING A RECTANGULAR WAVEGUIDE RESONANT SLOT TECHNIQUE

presented by

ANDREW ERIC BOGLE

has been accepted towards fulfillment
of the requirements for the

Doctoral degree in Electrical Engineering

Major Professor's Signature

16 Aug 2007

Date

ELECTROMAGNETIC MATERIAL CHARACTERIZATION OF A PEC BACKED LOSSY SIMPLE MEDIA USING A RECTANGULAR WAVEGUIDE RESONANT SLOT TECHNIQUE

By

Andrew Eric Bogle

A DISSERTATION

Submitted to
Michigan State University
in partial fulfillment of the requirements
for the degree of

DOCTOR OF PHILOSOPHY

Electrical and Computer Engineering

2007

ABSTRACT

ELECTROMAGNETIC MATERIAL CHARACTERIZATION OF A PEC BACKED LOSSY SIMPLE MEDIA USING A RECTANGULAR WAVEGUIDE RESONANT SLOT TECHNIQUE

By

Andrew Eric Bogle

Electromagnetic material characterization is the process of determining the complex constitutive parameters of a certain media. The motivation here is the development of a non-destructive material characterization technique for a lossy, simple-media (linear, homogeneous and isotropic) backed by a perfect electric conductor (PEC). In order to extract both the permittivity and permeability of the media, two independent experimental interrogations of the material are required. For a rectangular waveguide the experimental interrogations take the form of either reflection or transmission coefficients. The experimental data is then compared iteratively to the formulation, resulting in the extraction of the complex constitutive parameters for the media.

This dissertation will demonstrate, through the use of a transverse slot cut in the bottom wall of a rectangular waveguide, how waveguide scattering parameters are used to effectively extract both the permittivity and permeability of a lossy simple-media backed by a PEC. A two-dimensional Newton's complex root search algorithm is used to iteratively solve for the complex constitutive parameters. Results for a magnetic radar absorbing material are compared to measurements using a partially-filled rectangular waveguide technique to verify the formulation.

For Erica and Derby

ACKNOWLEDGMENTS

I would first like to thank my wife Erica. Her support, understanding and tolerance of me during this important period of our lives has been nothing short of amazing. I love her with everything I am and look forward to the rest of our lives together.

Thank you to Leo for believing in and supporting me during my entire graduate career. His patience and guidance have been invaluable in achieving this goal.

Thank you to Mike for all his time and effort. Especially on round table sessions and last second measurements, without which I would not be graduating.

Thank you to Dennis, Ed, and Shanker for all their time, teachings and guidance. They made my time with the EM group a wonderful experience.

Thank you to all the fellow graduate students over the years for helping me through the good, bad and extremely difficult times.

Thank you to my parents! There unquestionable love and support over the years has been more than I could ever dreamed of.

Finally, Thank you to all my family members for all their support!

I would also like to thank the AFOSR (through Dr. Charles Lee and the grants F-496-2002-10196 and FA9550-06-1-0023) for sponsoring this research, and the NSF CAREER program (ECS 0134236) for partial sponsorship of this research.

TABLE OF CONTENTS

CHAPTER 5

CHAPTER 6

APPENDIX A

APPENDIX B

APPENDIX C

LIST OF FIGURES

KEY TO SYMBOLS AND ABBREVIATIONS

BS1: Boundary S1

BS2: Boundary S2

CV: Cavity

dB: Decibels

ET: Electric Type

EM: Electromagnetic

HS: Half-Space

IE: Integral Equation

IDE: Integro-Differential Equation

LHP: Lower Half Plane

MFIE: Magnetic Field Integral Equation

MFIDE: Magnetic Field Integro-Differential Equation

MagRAM: Magnetic Radar Absorbing Material

MT: Magnetic Type

MoM: Method of Moments

NRW: Nicolson-Ross-Weir

NDE: Non-Destructive Evaluation

PP: Parallel-Plate

PEC: Perfect Electric Conductor

UHP: Upper Half Plane

VNA: Vector Network Analyzer

WG: Waveguide

CHAPTER 1

INTRODUCTION AND BACKGROUND

Electromagnetic (EM) material characterization is the process of determining the constitutive parameters of a specific medium. The parameters typically sought are the bulk permittivity and permeability, which are specific values that describe an EM materials susceptibility to becoming polarized or magnetized when exposed to either an impressed electric or magnetic field, respectively. For time-harmonic representations, both of these constitutive parameters can be complex values, where the real parts are related to the energy storage of the material, and the imaginary parts are related to the loss mechanisms that convert incident electromagnetic radiation into heat. As the number of applications for EM materials continues to grow, so does the need to accurately characterize them.

A number of disciplines rely extensively on the characterization of EM materials, including stealth, integrated circuits and agricultural technologies. For example, stealth uses the permittivity and permeability to describe how effective a material is at absorbing an incoming radar signal [1]-[3]. Whereas agricultural technologies uses the complex constitutive parameters to aid farmers in deciding when to harvest their crops [4]. A common thread to all of the applications is the increasing demand for better accuracy to achieve the desired results. This has lead to new challenges and increased levels of complexity for the material characterization field as a whole.

No matter what the complexity level though, the desired result is still the constitutive parameters. Two distinct evaluation methods, destructive and non-destructive, exist for extracting the permittivity and permeability of a specific medium. The major difference between the evaluation methods is how the sample is handled. For a destructive evaluation the sample may be altered to fit the desired testing device, whereas for the non-destructive evaluation (NDE) the testing device must be built around the existing operational environment of the desired sample. Destructive evaluations are typically measured in a small scale laboratory setting, since this generally keeps the cost low and the environmental control high, both of which are desirable traits when attempting to characterize any material. NDEs are generally not afforded either of these luxuries, and must be done in the existing operational environment at significant cost.

Still there is a need to perform NDEs of EM materials. The same basic steps in comparing the measured and theoretical data are usually used to find the permittivity and permeability in either the laboratory or operational setting. First, a material sample or testing device is built in the machine shop to facilitate the desired evaluation. Then the testing device is connected to a vector network analyzer (VNA) in order to obtain experimentally measured data. Finally, numerical algorithms are used to extract the complex constitutive parameters of the sample from the experimental data.

One of the most widely used algorithms is the Nicolson-Ross-Weir (NRW) technique, because it has the advantageous ability to directly solve for the material parameters in closed form [5]-[6]. However, for the NRW technique to be properly applied, the test samples must be linear, homogeneous and isotropic with coplanar front and back surfaces [7]. Essentially this means the testing device must not excite higher order modes, which unfortunately is not always possible.

Several NDE techniques have been developed to allow full-characterization of conductor-backed materials [8]-[11]. Three techniques, free-space, coaxial probe, and rectangular waveguide probe, are the most prevalent characterization methods. The free-space techniques have some unique advantages when compared to the other methods. For instance, the characterization may be done having no physical contact with the material sample. They may also be characterized as a function of incident angle or vertical and/or horizontal polarization [12]-[15]. However, they are not very effective outside the laboratory setting since significant errors are introduced when the numerous assumptions associated with the technique cannot be met in the operational environment.

Probe methods tend to have less restrictions associated with them, thus making them better fits for the operational environment characterization methods. To date, the majority of work investigated involves just single probe methods. These maybe grouped based on how they radiate electromagnetic fields: antenna probes; open-ended coaxial line probes; and open-ended waveguide probes. Antenna probes are essentially a combination of free-space and waveguide techniques, thus they still have a number of the drawbacks due to free-space component of the measurement [16]-[17].

Coaxial line probe methods make good NDE techniques since they have a wider measurement bandwidth and a higher accuracy than antenna probes [18]-[22]. The major drawback associated with these methods is the lack of ruggedness the coaxial lines have when used in an operational environment. Also, it is very difficult to ensure that no air-gaps are present between the center conductor of the open-ended portion of the coaxial line and the material sample.

Waveguide probe methods ultimately offer physical and EM advantages over coaxial probes. Physically, waveguides are more rugged than coaxial lines, making them smart choices for tests performed in operational environments. Since the accuracy between waveguide and coaxial probes is similar, the EM advantages of waveguide probes are in characteristics such as; wave impedance, radiation and linear polarization. Allowing for more accurate characterization of low permittivity materials, deeper penetration in lossy materials, and measurement of anisotropy, respectively [23]-[40].

The potential drawbacks of waveguide probes include their limited bandwidth and bulky size at lower frequencies. The concern of bulk sized waveguides is negated by using higher frequency waveguides. For instance, the WR90 X-band waveguide has dimensions 0.9" by 0.4", which make it very practical for use as a hand-held device. The concern of limited bandwidth has been investigated and solved by dielectrically loading the waveguide, enabling operation of the given waveguide at lower frequency ranges [10].

Recently, dual probe (collinear aperture) waveguide methods have been investigated [41]. These techniques are able to obtain multiple independent interrogations of the medium, without altering the experimental setup, which leads to the ability to simultaneously extract both of the complex constitutive parameters. This ability is especially significant in NDEs where alternate experimental setups are extremely difficult to develop. The dual probe techniques also help save time, reduce cost and remove the error associated with multiple measurements, all by simplifying the overall procedure necessary in the operational environment.

Slot apertures are another possibility for a collinear aperture waveguide method [42]-[45]. Extensive investigation of antennas involving slot apertures in waveguide walls has been done [46]-[56]. However, no investigation has yet been done to extend these antennas to a material characterization technique. This leads to the motivation for this dissertation, develop a NDE technique to characterize an EM material permanently affixed to a perfectly electric conducting (PEC) surface. More specifically, full characterization of the complex constitutive parameters, permittivity and permeability, for a lossy simple-medium (linear, homogeneous and isotropic) backed by a PEC surface using a slot aperture cut in the bottom wall of a rectangular waveguide.

Chapter 2 presents the integral equation (IE) technique that finds the theoretical scattering parameters for a rectangular waveguide radiating through a transverse slot, with finite thickness, into a half-space (HS). This is a well known antenna problem that will provide confidence in the waveguide (WG) and cavity (CV) portions of the formulation presented in Chapter 4, that will ultimately be used for extracting the complex constitutive parameters of the medium.

Chapter 3 develops the Green's function, which will be used in Chapter 4, for an EM field within a parallel-plate (PP) environment. Chapter 4 presents the IE technique that finds the theoretical scattering parameters for a rectangular waveguide radiating through a transverse slot, with finite thickness, into a lossy, homogeneous and isotropic medium backed by a PEC surface. These scattering parameters are then compared to experimental results in order to extract the desired results, permittivity and permeability.

Chapter 5 shows results of the complex constitutive parameter extraction for a magnetic radar absorbing material (MagRAM). The extraction is done using a complex two-dimensional Newton's root-searching algorithm, since the measurement technique developed violates the assumptions of the NRW technique. Chapter 6 presents conclusions and recommendations for future work.

CHAPTER 2

RECTANGULAR WAVEGUIDE RADIATING THROUGH A TRANSVERSE SLOT INTO A HALF-SPACE

2.1 Introduction

The formulation of a finite-thickness transverse slot centered in the broad wall of a rectangular waveguide, radiating into half-space, is considered in this chapter. Specifically, the reflection and transmission coefficients for the rectangular waveguide are sought. This is because they are ultimately used to perform the complex constitutive parameter extraction in Chapter 5, where the half-space is replaced by the PEC parallel-plate structure that is analyzed in Chapter 3. Understanding this well-studied problem provides an important form of confidence since the problem has been previously studied, well known results are available for referencing with the formulation presented here.

The first step in the formulation is to develop representations of the fields in the three different regions (WG, CV, and HS). Next, a set of coupled IEs are developed by satisfying the continuity of the tangential fields at the two interfaces (boundary S1 (BS1) and boundary S2 (BS2)) between the three regions. The final step is to solve the coupled IEs using a method of moments (MoM) technique for the unknown slot voltages, which in turn identify the scattered fields in the rectangular waveguide and ultimately the reflection and transmission coefficients desired.

2.2 Geometrical Configuration

Consider a rectangular waveguide, backed by an infinite ground plane, with a transverse slot cut in the lower broad-wall as shown in Figure 2.1. The waveguide has fixed dimensions for width $-a/2 < x < a/2$, height $t < z < b_1$ and length $y_I < y < y_T$, where $b_1 - t = b$ and the width (a) is in general greater than twice the height (b). The slot, shown in Figure 2.2, has fixed dimensions for width $-L < x < L$, height $0 < z < t$ and length $-W < y < W$, where the height (t) corresponds to the wall thickness of the waveguide and infinite ground plane. BS1 is located at $\vec{r_1} = (x_1, y_1, t)$ and is the interface between regions I and II. Similarly, BS2 is located at $\vec{r_2} = (x_2, y_2, 0)$ and is the interface between regions II and III.

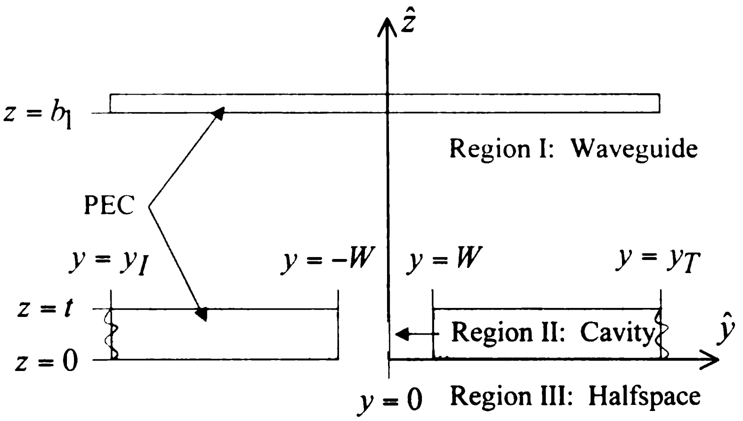

Figure 2.1. Geometrical Configuration: Rectangular waveguide radiating through a transverse slot into a half space

2.3 Field Representations

In order to develop the desired IEs, a representation of the fields in the three regions is needed. However, to generate the appropriate set of field equations a knowledge of the sources is necessary, thus the first section solves for the equivalent currents that maintain the fields in the three regions.

2.3.1 Equivalent Currents

To develop the equivalent currents for this formulation, a discussion of the excitation of the geometrical configuration in Figure 2.1 is helpful. The system is excited by the TE_{10}^{y} mode, which propagates down the guided-wave structure until it encounters the transverse slot in the broad wall of the waveguide, disrupting the current along the waveguide wall. An impressed field is then maintained in the slot aperture, inducing a voltage across the slot that subsequently maintains scattered waves in the rectangular waveguide. Thus, it is the impressed slot-fields that lead to the equivalent currents used to represent the fields in the three regions of this formulation.

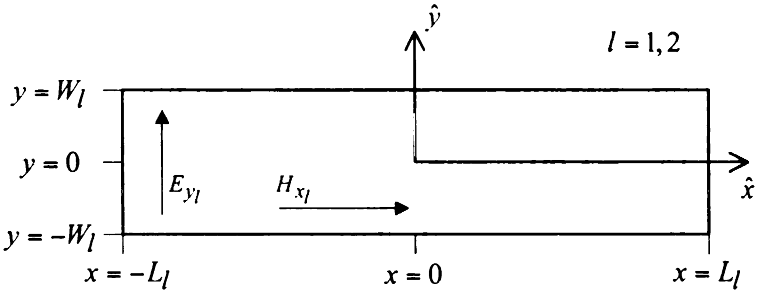

Figure 2.2. Geometrical Configuration: Top view of the transverse slot cut in broad wall of rectangular waveguide

Noting that the dimensions of the slot are long and narrow (i.e. ratio of slot length to slot width equals 1/20), then the electric-field in the slot is assumed to be strictly longitudinal (y-directed), which in turn assumes that the magnetic current in the slot is strictly transverse (x-directed). These assumptions mainly serve to simplify the overall complexity of the formulation and have also been proven very accurate [47]. Under these assumptions, the use of Love's equivalence principle [57] leads to the following four equivalent magnetic currents as seen in Figure 2.3.

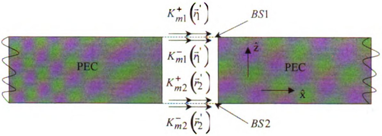

Figure 2.3. Equivalent currents for slot electric-fields at BS1 and BS2

$$K^+_{m1}\left(\vec{r_1}'\right) = -\hat{n}\times\vec{E}_1^+\left(\vec{r_1}'\right) = -\left(\hat{z}\right)\times\hat{y}E^+_{y1}\left(\vec{r_1}'\right) = \hat{x}E^+_{y1}\left(\vec{r_1}'\right) \tag{2.1}$$

$$K^-_{m1}\left(\vec{r_1}'\right) = -\hat{n}\times\vec{E}_1^-\left(\vec{r_1}'\right) = -\left(-\hat{z}\right)\times\hat{y}E_1^-\left(\vec{r_1}'\right) = -\hat{x}E^-_{y1}\left(\vec{r_1}'\right) \tag{2.2}$$

$$K^+_{m2}\left(\vec{r_2}'\right) = -\hat{n}\times\vec{E}_2^+\left(\vec{r_2}'\right) = -\left(\hat{z}\right)\times\hat{y}E^+_{y2}\left(\vec{r_2}'\right) = \hat{x}E^+_{y2}\left(\vec{r_2}'\right) \tag{2.3}$$

$$K^-_{m2}\left(\vec{r_2}'\right) = -\hat{n}\times\vec{E}_2^-\left(\vec{r_2}'\right) = -\left(-\hat{z}\right)\times\hat{y}E^-_{y2}\left(\vec{r_2}'\right) = -\hat{x}E^-_{y2}\left(\vec{r_2}'\right) \tag{2.4}$$

Where (2.1) corresponds to the waveguide equivalent magnetic current, (2.2) and (2.3) to the cavity equivalent magnetic currents at BS1 and BS2 respectively, and (2.4) is the half-space equivalent magnetic current. Note that all the equivalent currents have only a x-directed component.

2.3.2 General Field Relations

Since all the sources are equivalent magnetic currents, the general field relations are those based on Maxwell's equations due a magnetic source. These general field relations in terms of magnetic-type (MT) Hertzian potentials (details in Appendix A) are written as follows

$$\vec{E}\left(\vec{r}\right) = -j\omega\mu\nabla\times\vec{\pi}_h\left(\vec{r}\right) \tag{2.5}$$

$$\vec{H}\left(\vec{r}\right) = \nabla\left(\nabla\cdot\vec{\pi}_h\left(\vec{r}\right)\right) + k^2\vec{\pi}_h\left(\vec{r}\right) \tag{2.6}$$

where the MT Hertzian wave-equation is

$$\left(\nabla^2 + k^2\right) \vec{\pi}_h\left(\vec{r}\right) = -\frac{\vec{K}_m\left(\vec{r}'\right)}{j\omega\mu} \tag{2.7}$$

and the solution to this wave-equation in terms of the MT Hertzian potential may be written as

$$\vec{\pi}_h\left(\vec{r}\right) = \int_{S_a} \overleftrightarrow{G}\left(\vec{r}|\vec{r}'\right) \cdot \frac{\vec{K}_m\left(\vec{r}'\right)}{j\omega\mu} dS'_a \tag{2.8}$$

where $\overleftrightarrow{G}$ is the dyadic Green's function.

2.3.2.1 Total Fields in each Region

Using the knowledge that there are only x-directed components of the sources, and the principle of superposition [58], the magnetic field in equation (2.6) is now written in terms of only the x-component as follows

$$H_x\left(\vec{r}\right) = \left(\frac{\partial^2}{\partial x^2} + k^2\right) \pi_{h_x}\left(\vec{r}\right) \tag{2.9}$$

where π_{h_x} is the x-component of the MT Hertzian potential given as

$$\pi_{h_x}\left(\vec{r}\right) = \int_{S_a} G_{xx}\left(\vec{r}|\vec{r}'\right) \frac{K_{m_x}\left(\vec{r}'\right)}{j\omega\mu} dS'_a \tag{2.10}$$

with G_x as the x-component of the dyadic Green's function and K_{m_x} as the equivalent magnetic current for each specific region.

This allows the total magnetic field in region 1 to be written as

$$H_x^{region1}\left(\vec{r_1}\right) = H_x^{inc}\left(\vec{r_1}\right) + H_x^{WGS}\left(\vec{r_1}\right) \tag{2.11}$$

where H_x^{inc} is the incident wave in the rectangular waveguide, and H_x^{WGS} is the waves scattered by the transverse slot in the rectangular waveguide. In a similar manner, the total magnetic field in region 2 is

$$H_x^{region2}(\vec{r_l}) = H_x^{CV1}(\vec{r_l}) + H_x^{CV2}(\vec{r_l}) \quad \cdots for \quad l = 1, 2 \tag{2.12}$$

where H_x^{CV1} is the waves scattered by the transverse slot at $z = t$ in the cavity region, and H_x^{CV2} is the waves scattered by the transverse slot at $z = 0$. Finally, the total magnetic field in region 3 is

$$H_x^{region3}(\vec{r_2}) = H_x^{HS}(\vec{r_2}) \tag{2.13}$$

where H_x^{HS} is the waves scattered by the transverse slot into the half-space.

2.3.2.2 MT Hertzian Potentials in terms of Equivalent Currents

All that remains to fully represent the fields in each region is to define the MT Hertzian potentials associated with the total fields in equations (2.11-2.13). This is accomplished by substituting equations (2.1-2.4) into equation (2.10) and defining the Green's functions for each region, leading to

$$\pi_{h_x}^{WGS}(\vec{r_1}) = \int_{S_1} G_{WG}(\vec{r_1}|\vec{r_1}') \frac{E_{y1}^{+}(\vec{r_1}')}{j\omega\mu_0} dS_1' \tag{2.14}$$

$$\pi_{h_x}^{CV1}(\vec{r_l}) = \int_{S_1} -G_{CV}(\vec{r_l}|\vec{r_1}') \frac{E_{y1}^{-}(\vec{r_1}')}{j\omega\mu_0} dS_1' \tag{2.15}$$

$$\pi_{h_x}^{CV2}(\vec{r_l}) = \int_{S_2} G_{CV}(\vec{r_l}|\vec{r_2}') \frac{E_{y2}^{+}(\vec{r_2}')}{j\omega\mu_0} dS_2' \tag{2.16}$$

$$\pi_{h_x}^{HS}(\vec{r_2}) = \int_{S_2} -G_{HS}(\vec{r_2}|\vec{r_2}') \frac{E_{y2}^{-}(\vec{r_2}')}{j\omega\mu_0} dS_2' \tag{2.17}$$

where (2.15-2.16) are observed at either BS1 or BS2. The Green's function for the rectangular waveguide due to a transverse slot is given by

$$\begin{aligned} G_{WG}\left(\vec{r_1}|\vec{r_1}'\right) = & \tfrac{1}{ab}\textstyle\sum_\gamma \frac{\epsilon_\gamma}{jk_{y_\gamma}} \sin\left[k_{x_\gamma}\left(x_1 - a/2\right)\right] \sin\left[k_{x_\gamma}\left(x_1' - a/2\right)\right] \\ & \cdot e^{-jk_{y_\gamma}\left|y_1 - y_1'\right|} \cos\left[k_{z_\gamma}\left(z_1 - t\right)\right] \cos\left[k_{z_\gamma}\left(z_1' - t\right)\right] \end{aligned} \tag{2.18}$$

while, the Green's function for the rectangular cavity is

$$\begin{aligned} G_{CV}\left(\vec{r_l}|\vec{r_l}'\right) = & \tfrac{-2}{a_c b_c}\textstyle\sum_\Gamma \frac{\epsilon_\Gamma}{k_{z_\Gamma}\sin\left(k_{z_\Gamma} c_c\right)} \\ & \cdot \sin\left[k_{x_\Gamma}\left(x_l - a_c/2\right)\right] \sin\left[k_{x_\Gamma}\left(x_l' - a_c/2\right)\right] \\ & \cdot \cos\left[k_{y_\Gamma}\left(y_l - b_c/2\right)\right] \cos\left[k_{y_\Gamma}\left(y_l' - b_c/2\right)\right] \\ & \cdot \begin{bmatrix} \cos\left[k_{z_\Gamma}\left(z_l - c_c\right)\right]\cos\left(k_{z_\Gamma} z_l'\right) & for & z_l > z_l' \\ \cos\left(k_{z_\Gamma} z_l\right)\cos\left[k_{z_\Gamma}\left(z_l' - c_c\right)\right] & for & z_l < z_l' \end{bmatrix} \end{aligned} \tag{2.19}$$

and the well known half-space Green's function is

$$G_{HS}\left(\vec{r_2}|\vec{r_2}'\right) = \frac{e^{-jk_0 R}}{2\pi R} \tag{2.20}$$

where the distance R is defined as

$$R = \sqrt{\left(x_2 - x_2'\right)^2 + \left(y_2 - y_2'\right)^2 + \left(z_2 - z_2'\right)^2} \tag{2.21}$$

The wavenumbers and the Neumann's number [56] for both the rectangular waveguide and cavity are given as

$$k_{x_{(\gamma,\Gamma)}} = \frac{\alpha_{(wg,cv)}\pi}{a_{(wg,cv)}}, \alpha_{(wg,cv)} = 1, 2, 3, ...$$
$$k_{z_{(\gamma,\Gamma)}} = \frac{\beta_{(wg,cv)}\pi}{b_{(wg,cv)}}, \beta_{(wg,cv)} = 0, 1, 2, ...$$
$$k^2_{c_{(\gamma,\Gamma)}} = k_0^2 - k^2_{y_{(\gamma,\Gamma)}} = k^2_{x_{(\gamma,\Gamma)}} + k^2_{z_{(\gamma,\Gamma)}} \tag{2.22}$$

and

$$\epsilon_{(\gamma,\Gamma)} = \begin{cases} 1 & for \quad \beta_{(wg,cv)} = 0 \\ 2 & for \quad \beta_{(wg,cv)} \neq 0 \end{cases} \tag{2.23}$$

respectively. Details of equations (2.18) and (2.19) are found in Appendix B. These field representations for the three regions are now used to develop IEs in the next section.

2.4 Development of the Coupled MFIEs

In this section, a pair of coupled IEs are developed (for unknown slot-voltages (V_1, V_2) at BS1 and BS2 respectively) by invoking boundary conditions at the two interfaces. The continuity of both the electric and magnetic fields ensures a unique solution for the desired unknowns. The fact that magnetic fields are used leads to the formulation being called a MFIE.

2.4.1 Development of the MFIDEs

Since the MT Hertzian potentials involve and integral over the slot apertures, the first integral equations developed are actually magnetic field integro-differential equations (MFIDE). Standard techniques are then used to solve the resulting second-order partial-differential equations, ultimately resulting in the desired MFIEs.

2.4.1.1 BS1

The MFIDE at BS1 is developed by invoking the continuity of tangential magnetic fields at the interface ($z = t$) giving

$$H_x^{region1}(\vec{r_1}) = H_x^{region2}(\vec{r_1}) \tag{2.24}$$

then, substituting equations (2.11) and (2.12) into equation (2.24) leads to

$$H_x^{inc}(\vec{r_1}) + H_x^{WGS}(\vec{r_1}) = H_x^{CV1}(\vec{r_1}) + H_x^{CV2}(\vec{r_1}) \tag{2.25}$$

finally, substituting (2.10) into (2.9) and then (2.14-2.16) into the respective magnetic field representation, leads to the first MFIDE result

$$\begin{aligned}\left(\frac{\partial^2}{\partial x^2} + k_0^2\right)\Bigg\{\int_{S_1} \frac{E_{y1}(\vec{r_1}')}{j\omega\mu_0} G_{WC}(\vec{r_1}|\vec{r_1}')\, dS_1' \\ - \int_{S_2} \frac{E_{y2}(\vec{r_2}')}{j\omega\mu_0} G_{CV}(\vec{r_1}|\vec{r_2}')\, dS_2'\Bigg\} = -H_x^{inc}(\vec{r_1})\end{aligned} \tag{2.26}$$

where

$$G_{WC}(\vec{r_1}|\vec{r_1}') = G_{WG}(\vec{r_1}|\vec{r_1}') + G_{CV}(\vec{r_1}|\vec{r_1}') \tag{2.27}$$

Note that the continuity of the electric fields across the two interfaces is enforced by making $E_{y1}^{+} = E_{y1}^{-}$ and $E_{y2}^{+} = E_{y2}^{-}$.

2.4.1.2 BS2

Similarly, the MFIDE at BS2 is developed by invoking the continuity of tangential magnetic fields at the interface ($z = 0$) giving

$$H_x^{region2}(\vec{r_2}) = H_x^{region3}(\vec{r_2}) \tag{2.28}$$

where substitution of equations (2.12) and (2.13) into equation (2.28) gives

$$H_x^{CV1}(\vec{r_2}) + H_x^{CV2}(\vec{r_2}) = H_x^{HS}(\vec{r_2}) \tag{2.29}$$

and finally, substituting (2.10) into (2.9) and then (2.15-2.17) into the respective magnetic field representation, leads to the second MFIDE result

$$\begin{aligned}\left(\frac{\partial^2}{\partial x^2} + k_0^2\right) \Bigg\{ \int_{S_1} & \frac{E_{y1}(\vec{r_1}')}{j\omega\mu_0} G_{CV}(\vec{r_2}|\vec{r_1}')\, dS_1' \\ & - \int_{S_2} \frac{E_{y2}(\vec{r_2}')}{j\omega\mu_0} G_{CH}(\vec{r_2}|\vec{r_2}')\, dS_2' \Bigg\} = 0\end{aligned} \tag{2.30}$$

where

$$G_{CH}(\vec{r_2}|\vec{r_2}') = G_{CV}(\vec{r_2}|\vec{r_2}') + G_{HS}(\vec{r_2}|\vec{r_2}') \tag{2.31}$$

2.4.2 Solving the Second-Order Partial-Differential Equation

By inspection, it is seen that the MFIDEs developed in the last section are integro-differential equations. These integro-differential equations are converted into purely integral equations by superposing the homogeneous and inhomogeneous solutions to the second-order partial-differential equations [56]. Thus, further simplifying the complexity of the overall problem.

The solution of the homogeneous equation is solved using the method of undetermined coefficients [59], where sine and cosine functions are chosen as the complementary solutions. To solve the inhomogeneous equation, the forced response to the inhomogeneous one-dimensional Helmholtz equation

$$\Psi(x) = \frac{1}{k} \int_a^x s(x') \sin\left[k(x - x')\right] dx' \tag{2.32}$$

is used as the particular solution [60]. The superposition of the complementary and particular solutions leads to the strictly integral equations desired. These MFIEs are complements of Hallen's integral equation for a dipole antenna [56], given the fact that the slots are assumed to lie in a PEC plane.

2.4.2.1 MFIE at BS1

The integro-differential equation (2.26) is written as

$$\left(\frac{\partial^2}{\partial x^2} + k_0^2\right) F_1\left(\vec{r_1}\right) = A_1\left(\vec{r_1}\right) \tag{2.33}$$

where

$$\begin{aligned} F_1\left(\vec{r_1}\right) = & \int_{S_1} \frac{E_{y1}\left(\vec{r_1}'\right)}{j\omega\mu_0} G_{WC}\left(\vec{r_1}|\vec{r_1}'\right) dS_1' \\ & - \int_{S_2} \frac{E_{y2}\left(\vec{r_2}'\right)}{j\omega\mu_0} G_{CV}\left(\vec{r_1}|\vec{r_2}'\right) dS_2' \end{aligned} \tag{2.34}$$

is in the form of the MT Hertzian potential and

$$A_1\left(\vec{r_1}\right) = -H_x^{inc}\left(\vec{r_1}\right) = -A_{10}\left[(\pi/a)^2 - k_0^2\right] \cos\left(\pi x_1/a\right) e^{-jk_{y10}y_1} \tag{2.35}$$

is the forcing term based on the x-component of the incident magnetic field.

The solution to equation (2.33) is written as

$$F_1\left(\vec{r_1}\right) = F_1^C\left(\vec{r_1}\right) + F_1^P\left(\vec{r_1}\right) \tag{2.36}$$

where the complementary solution is given as

$$F_1^C\left(\vec{r_1}\right) = C_1\left(y_1\right)\cos\left(k_0 x_1\right) + D_1\left(y_1\right)\sin\left(k_0 x_1\right) \tag{2.37}$$

and the particular solution, in terms of the forced response of equation (2.32) and the

x-component of the incident magnetic field from equation (2.35), is

$$F_1^P(\vec{r_1}) = -\frac{A_{10}\left[(\pi/a)^2 - k_0^2\right] e^{-jk_{y10}y_1}}{k_0} \int_0^{x_1} \sin\left[k_0(x_1 - \overline{x}_1)\right] \cos(\pi\overline{x}_1/a) d\overline{x}_1 \quad (2.38)$$

Solving the forced response integral, and performing some algebraic manipulation, gives the following form of the particular solution

$$F_1^P(\vec{r_1}) = -A_{10}e^{-jk_{y10}y_1}\left[\cos(k_0x_1) - \cos(\pi x_1/a)\right] \quad (2.39)$$

Finally, substituting equations (2.34), (2.38), and (2.39) into equation (2.36) and combining complementary solutions, leads to the MFIE at BS1

$$\int_{S_1} \frac{E_{y1}(\vec{r_1}')}{j\omega\mu_0} G_{WC}(\vec{r_1}|\vec{r_1}')\, dS_1' - \int_{S_2} \frac{E_{y2}(\vec{r_2}')}{j\omega\mu_0} G_{CV}(\vec{r_1}|\vec{r_2}')\, dS_2'$$
$$= \tilde{C}_1(y_1)\cos(k_0x_1) + D_1(y_1)\sin(k_0x_1) + A_{10}e^{-jk_{y10}y_1}\cos(\pi x_1/a) \quad (2.40)$$

2.4.2.2 MFIE at BS2

Similarly for BS2, the integro-differential equation (2.30) is written in the form

$$\left(\frac{\partial^2}{\partial x^2} + k_0^2\right) F_2(\vec{r_2}) = A_2(\vec{r_2}) \quad (2.41)$$

where

$$\begin{aligned} F_2(\vec{r_2}) = &\int_{S_1} \frac{E_{y1}(\vec{r_1}')}{j\omega\mu_0} G_{CV}(\vec{r_2}|\vec{r_1}')\, dS_1' \\ &- \int_{S_2} \frac{E_{y2}(\vec{r_2}')}{j\omega\mu_0} G_{CH}(\vec{r_2}|\vec{r_2}')\, dS_2' \end{aligned} \quad (2.42)$$

and

$$A_2(\vec{r_2}) = 0 \quad (2.43)$$

The forcing term A_2 is equal to zero since there is no incident field at BS2, thus the solution to equation (2.41) has only a complementary portion given as

$$F_2^C(\vec{r_2}) = C_2(y_2)\cos(k_0x_2) + D_2(y_2)\sin(k_0x_2) \tag{2.44}$$

Substituting equations (2.42) and (2.44) into equation (2.41), gives the MFIE at BS2

$$\begin{aligned}\int_{S_1} \frac{E_{y1}(\vec{r_1}')}{j\omega\mu_0} G_{CV}(\vec{r_2}|\vec{r_1}')\, dS_1' - \int_{S_2} \frac{E_{y2}(\vec{r_2}')}{j\omega\mu_0} G_{CH}(\vec{r_2}|\vec{r_2}')\, dS_2' \\ = C_2(y_2)\cos(k_0x_2) + D_2(y_2)\sin(k_0x_2)\end{aligned} \tag{2.45}$$

2.5 MoM Technique

In this section, a MoM technique is applied to solve the MFIEs developed in the last section. The steps taken to apply the MoM technique, along with a summary of the solution, is discussed here in.

2.5.1 Expansion of Fields In Terms of unknown Slot Voltages

In order to solve equations (2.40) and (2.45) using a MoM technique the slot electric-fields are expanded in terms of the unknown slot voltages. Based on the discussion in section 2.3.1, the slot electric-field is assumed to have only a longitudinal component. Using this assumption, it is appropriate to separately expand the slot electric-field into longitudinal and transverse components as follows

$$E_{yl}(\vec{r_l}) = V_l(x_l)\, f_l(y_l) \quad for \quad l = 1, 2 \tag{2.46}$$

where the voltage rise across the slot width is interpreted as

$$V_l(x_l) = -\int_{W_l}^{-W_l} E_{yl}(\vec{r_l})\, dy_l = \int_{-W_l}^{W_l} E_{yl}(\vec{r_l}))dy_l \tag{2.47}$$

The distribution f_l is chosen to ensure the integral over the y-dependence is equal to one. This is so the only contribution to the slot field, due to the expansion, is from the unknown slot voltage. The following expansion of the slot electric field is obtained

$$E_{yl}\left(\vec{r_l}\right) = V_l\left(x_l\right) = V_l\left(x_l\right) \int\limits_{-W_l}^{W_l} dy_l f_l\left(y_l\right) \tag{2.48}$$

where a constant distribution is chosen leading to the function

$$f_l\left(y_l\right) = \frac{1}{2W_l} \tag{2.49}$$

2.5.1.1 Expanded MFIE at BS1

Applying the slot electric-field expansion in equation (2.48) to equation (2.40) leads to the expanded version of the MFIE at BS1

$$\begin{aligned} &\int\limits_{-L_1}^{L_1} dx_1' V_1\left(x_1'\right) K_{WC}\left(x_1, y_1 | x_1'\right) - \int\limits_{-L_2}^{L_2} dx_2' V_2\left(x_2'\right) K_{CV2}\left(x_1, y_1 | x_2'\right) \\ &= \tilde{C}_1\left(y_1\right)\cos\left(k_0 x_1\right) + D_1\left(y_1\right)\sin\left(k_0 x_1\right) + A_{10} e^{-jk_{y10} y_1}\cos\left(\pi x_1 / a\right) \end{aligned} \tag{2.50}$$

where the kernels at BS1 are defined as

$$K_{WC}\left(x_1, y_1 | x_1'\right) = \int\limits_{-W_1}^{W_1} dy_1' \frac{f_1\left(y_1'\right)}{j\omega\mu_0} G_{WC}\left(\vec{r_1} | \vec{r_1}'\right) \tag{2.51}$$

$$K_{CV2}\left(x_1, y_1 | x_2'\right) = \int\limits_{-W_2}^{W_2} dy_2' \frac{f_2\left(y_2'\right)}{j\omega\mu_0} G_{CV}\left(\vec{r_1} | \vec{r_2}'\right) \tag{2.52}$$

2.5.1.2 Expanded MFIE at BS2

Similarly, substituting the same slot electric field expansion from equation (2.48) into equation (2.45) leads to the expanded version of the MFIE at BS2

$$\int_{-L_1}^{L_1} dx_1' V_1(x_1') K_{CV1}(x_2, y_2|x_1') - \int_{-L_2}^{L_2} dx_2' V_2(x_2') K_{CH}(x_2, y_2|x_2') = C_2(y_2)\cos(k_0 x_2) + D_2(y_2)\sin(k_0 x_2) \qquad (2.53)$$

where the kernels at BS2 are defined as

$$K_{CV1}(x_2, y_2|x_1') = \int_{-W_1}^{W_1} dy_1' \frac{f_1(y_1')}{j\omega\mu_0} G_{CV}(\vec{r_2}|\vec{r_1}') \qquad (2.54)$$

$$K_{CH}(x_2, y_2|x_2') = \int_{-W_2}^{W_2} dy_2' \frac{f_2(y_2')}{j\omega\mu_0} G_{CH}(\vec{r_2}|\vec{r_2}') \qquad (2.55)$$

2.5.2 Application of the MoM Technique

The coupled MFIEs in equations (2.50) and (2.53) are classified as inhomogeneous Fredholm IEs of the first kind, and are solved using a MoM technique. There are two steps associtated with the MoM technique. They are the expansion of the unknowns and the application of a testing operator, using an appropriate set of expansion and testing functions, respectively.

The choice of these functions is usually strongly influenced by the physical and mathematical characteristics of the IEs. From the physical point of view, the expansion functions should closely model the behavior of the unknowns, so that a minimum number of expansions is necessary to obtain accurate results. In addition, a prudent choice of the expansion and testing functions could allow the various integrals to be computed in closed form. It is not necessary to obtain closed-form integrals; however, they do significantly reduce the computational efforts. However, experience with the moment method has indicated that simple basis functions, which expedite the computation of the matrix elements, are usually a suitable choice [60].

The slot under analysis in this formulation was chosen to be resonant at the mid-frequency of the rectangular waveguide. Using the knowledge that the slot is the complementary problem of the strip dipole, a reasonable approximation for the behavior of the slot voltage is a sinusoidal distribution. Thus, it would seem a sinusoidal expansion function is the best fit from a physical standpoint. However, based on the discussion at the end of the last paragraph a pulse function expansion is likely a more convenient choice, and therefore is chosen in this formulation. Also for convenience point matching at the center of each cell is used for the testing operator.

Applying the following point-matching testing operator

$$\int_{-W_l}^{W_l} \int_{-L_l}^{L_l} dx_l dy_l \delta \left(x_l - x_{l_{m_l}} \right) \delta \left(y_l \right) \quad for \quad m_l = 1, 2, ..., N_l \tag{2.56}$$

($l = 1, 2$ depending on which interface the testing is taking place at) to equations (2.49) and (2.52) respectively, leads to

$$\int_{-L_1}^{L_1} dx_1' V_1 \left(x_1' \right) K_{WC} \left(x_{1_{m_1}}, 0 | x_1' \right) - \int_{-L_2}^{L_2} dx_2' V_2 \left(x_2' \right) K_{CV2} \left(x_{1_{m_1}}, 0 | x_2' \right)$$
$$= \tilde{C}_1 \left(0 \right) \cos \left(k_0 x_{1_{m_1}} \right) + D_1 \left(0 \right) \sin \left(k_0 x_{1_{m_1}} \right) + A_{10} \cos \left(\pi x_{1_{m_1}} / a \right)$$
$$for \quad m_1 = 1, 2, ..., N_1 \tag{2.57}$$

for BS1, and

$$\int_{-L_1}^{L_1} dx'_1 V_1\left(x'_1\right) K_{CV1}\left(x_{2m_2}, 0|x'_1\right) - \int_{-L_2}^{L_2} dx'_2 V_2\left(x'_2\right) K_{CH}\left(x_{2m_2}, 0|x'_2\right)$$
$$= C_2\left(0\right)\cos\left(k_0 x_{2m_2}\right) + D_2\left(0\right)\sin\left(k_0 x_{2m_2}\right)$$
$$for \quad m_2 = 1, 2, ..., N_2 \qquad (2.58)$$

for BS2. These equations are then expanded in terms of the unknown slot-voltages, using the pulse-function expansion shown in Figure 2.4 and given as

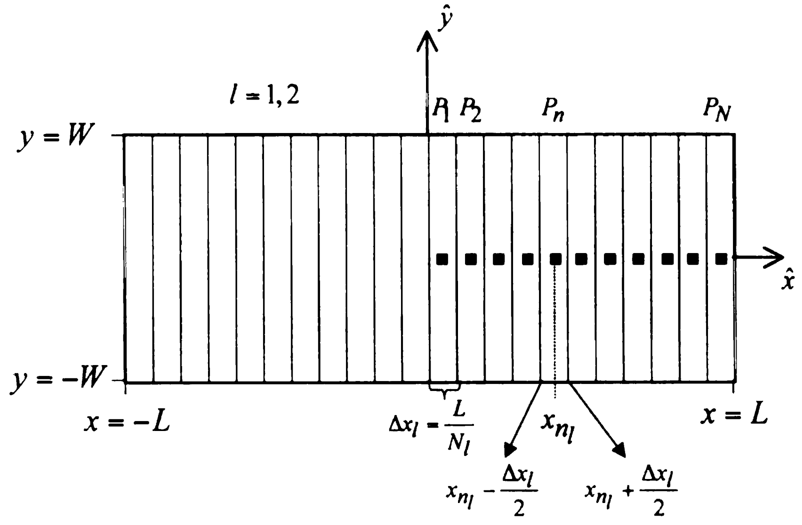

Figure 2.4. Pulse function expansion for the MoM technique

$$V_l\left(x_l\right) = \sum_{n_l=1}^{N_l} V_{ln_l} p_{ln_l}\left(x_l\right) \qquad (2.59)$$

where the individual segment length and location respectively are

$$\triangle x_l = 2L_l/N_l \quad ; \quad x_{l_{n_l}} = -L_l + (n_l - 1/2)\triangle x_l \tag{2.60}$$

and the pulse function is defined as

$$p_{l_{n_l}}(x_l) = \begin{cases} 1 & \ldots \left(x_{l_{n_l}} - \frac{\triangle x_l}{2}\right) < x_l < \left(x_{l_{n_l}} + \frac{\triangle x_l}{2}\right) \\ 0 & \ldots \quad otherwise \end{cases} \tag{2.61}$$

Substituting the expression for the pulse-function expansion into equations (2.57) and (2.58) respectively, gives

$$\begin{aligned} &\sum_{n_1=1}^{N_1} V_{1_{n_1}} \int_{x_{1_{n_1}}-\frac{\triangle x_1}{2}}^{x_{1_{n_1}}+\frac{\triangle x_1}{2}} dx_1' K_{WC}\left(x_{1_{m_1}}, 0 | x_1'\right) \\ &- \sum_{n_2=1}^{N_2} V_{2_{n_2}} \int_{x_{2_{n_2}}-\frac{\triangle x_2}{2}}^{x_{2_{n_2}}+\frac{\triangle x_2}{2}} dx_2' K_{CV2}\left(x_{1_{m_1}}, 0 | x_2'\right) \\ = \tilde{C}_1(0)\cos\left(k_0 x_{1_{m_1}}\right) &+ D_1(0)\sin\left(k_0 x_{1_{m_1}}\right) + A_{10}\cos\left(\pi x_{1_{m_1}}/a\right) \\ &\qquad for \quad m_1 = 1, 2, \ldots, N_1 \end{aligned} \tag{2.62}$$

for BS1, and

$$\sum_{n_1=1}^{N_1} V_{1_{n_1}} \int\limits_{x_{1_{n_1}}-\frac{\Delta x_1}{2}}^{x_{1_{n_1}}+\frac{\Delta x_1}{2}} dx_1' K_{CV1}\left(x_{2_{m_2}},0|x_1'\right)$$

$$-\sum_{n_2=1}^{N_2} V_{2_{n_2}} \int\limits_{x_{2_{n_2}}-\frac{\Delta x_2}{2}}^{x_{2_{n_2}}+\frac{\Delta x_2}{2}} dx_2' K_{CH}\left(x_{2_{m_2}},0|x_2'\right)$$

$$= C_2\left(0\right)\cos\left(k_0 x_{2_{m_2}}\right) + D_2\left(0\right)\sin\left(k_0 x_{2_{m_2}}\right)$$

$$for \quad m_2 = 1,2,...,N_2 \tag{2.63}$$

for BS2. These equations represent the MoM solution, for the unknown slot voltages (V_1, V_2), to the MFIEs of section 2.4. However, four constants (C_1, D_1, C_2, D_2) still remain unsolved. These constants get evaluated by invoking the boundary conditions

$$V_{l_{1,N_l}} = 0 \quad for \quad l = 1,2 \tag{2.64}$$

which leads to the final expressions for the MoM solution

$$\sum_{n_1=2}^{N_1-1} V_{1_{n_1}} \int\limits_{x_{1_{n_1}}-\frac{\Delta x_1}{2}}^{x_{1_{n_1}}+\frac{\Delta x_1}{2}} dx_1' K_{WC}\left(x_{1_{m_1}},0|x_1'\right)$$

$$-\sum_{n_2=2}^{N_2-1} V_{2_{n_2}} \int\limits_{x_{2_{n_2}}-\frac{\Delta x_2}{2}}^{x_{2_{n_2}}+\frac{\Delta x_2}{2}} dx_2' K_{CV2}\left(x_{1_{m_1}},0|x_2'\right)$$

$$= \tilde{C}_1\left(0\right)\cos\left(k_0 x_{1_{m_1}}\right) + D_1\left(0\right)\sin\left(k_0 x_{1_{m_1}}\right) + A_{10}\cos\left(\pi x_{1_{m_1}}/a\right)$$

$$for \quad m_1 = 1,2,...,N_1 \tag{2.65}$$

at BS1 and

$$\sum_{n_1=2}^{N_1-1} V_{1_{n_1}} \int_{x_{1_{n_1}}-\frac{\triangle x_1}{2}}^{x_{1_{n_1}}+\frac{\triangle x_1}{2}} dx_1' K_{CV1}\left(x_{2_{m_2}},0|x_1'\right)$$
$$-\sum_{n_2=2}^{N_2-1} V_{2_{n_2}} \int_{x_{2_{n_2}}-\frac{\triangle x_2}{2}}^{x_{2_{n_2}}+\frac{\triangle x_2}{2}} dx_2' K_{CH}\left(x_{2_{m_2}},0|x_2'\right)$$
$$= C_2(0)\cos\left(k_0 x_{2_{m_2}}\right) + D_2(0)\sin\left(k_0 x_{2_{m_2}}\right)$$
$$for \quad m_2 = 1,2,...,N_2 \tag{2.66}$$

at BS2.

2.5.3 MoM Solution in Matrix Form

Equations (2.65) and (2.66) are summarized in matrix form as

$$\sum_{n=1}^{N} a_{m,n} C_m = b_m \quad for \quad m = 1,2,3,...,N \tag{2.67}$$

where $N = N_1 + N_2$ and

$$b_m = \begin{cases} A_{10}\cos\left(\pi x_{1_m}/a\right) & for \quad m = 1,2,...,N_1 \\ 0 & for \quad m = N_1+1, N_1+2,...,N \end{cases} \tag{2.68}$$

is the forcing vector due to the incident x-directed component of the magnetic field. The unknown slot voltages and constants are defined as

$$C_m = \begin{cases} C_1 & for \quad m = 1 \\ V1_m & for \quad m = 2, 3, ..., N_1 - 1 \\ D_1 & for \quad m = N_1 \\ C_2 & for \quad m = N_1 + 1 \\ V2_{m-N_1} & for \quad m = N_1 + 2, N_1 + 3, ..., N - 1 \\ D_2 & for \quad m = N \end{cases} \tag{2.69}$$

and finally, a summary of the moment method admittance matrix elements

$$a_{m,n} = \begin{cases} -\cos\left(k_0 x_{1_m}\right) & for \left\{\begin{array}{ll} m & = 1,2,\ldots,N_1 \\ n & = 1 \end{array}\right. \\ -\sin\left(k_0 x_{1_m}\right) & for \left\{\begin{array}{ll} m & = 1,2,\ldots,N_1 \\ n & = N_1 \end{array}\right. \\ -\cos\left(k_0 x_{2_{m-N_1}}\right) & for \left\{\begin{array}{ll} m & = N_1+1, N_1+2,\ldots,N \\ n & = N_1+1 \end{array}\right. \\ -\sin\left(k_0 x_{2_{m-N_1}}\right) & for \left\{\begin{array}{ll} m & = N_1+1, N_1+2,\ldots,N \\ n & = N \end{array}\right. \\ 0 & for \left\{\begin{array}{ll} m & = 1,2,\ldots,N_1 \\ n & = N_1+1, N \end{array}\right. \\ 0 & for \left\{\begin{array}{ll} m & = N_1+1, N_1+2,\ldots,N \\ n & = 1, N_1 \end{array}\right. \\ l^{WC}_{m,n} & for \left\{\begin{array}{ll} m & = 1,2,\ldots,N_1 \\ n & = 2,3,\ldots,N_1-1 \end{array}\right. \\ -l^{C1}_{m,n-N_1} & for \left\{\begin{array}{ll} m & = 1,2,\ldots,N_1 \\ n & = N_1+2, N_1+3,\ldots,N-1 \end{array}\right. \\ l^{C2}_{m-N_1,n} & for \left\{\begin{array}{ll} m & = N_1+1, N_1+2,\ldots,N \\ n & = 2,3,\ldots,N_1-1 \end{array}\right. \\ -l^{CH}_{m-N_1,n-N_1} & for \left\{\begin{array}{ll} m & = N_1+1, N_1+2,\ldots,N \\ n & = N_1+2, N_1+3,\ldots,N-1 \end{array}\right. \end{cases} \tag{2.70}$$

2.5.3.1 Matrix Element Definitions

The solutions for the various admittance matrix elements (details in Appendix C) are given here. For the first quadrant of matrix elements, the combination of the waveguide and cavity self terms at BS1 is

$$l^{WC}_{m_1,n_1} = l^{WG}_{m_1,n_1} + l^{CV11}_{m_1,n_1} \tag{2.71}$$

where

$$l^{WG}_{m_1,n_1} = \frac{-2j}{\omega\mu_0 abW_1} \sum_{\gamma} \frac{\epsilon_\gamma}{k_{x_\gamma} k^2_{y_\gamma}} \sin\left[k_{x_\gamma}\left(x_{1_{m_1}} - a/2\right)\right] \sin\left[k_{x_\gamma}\left(x_{1_{n_1}} - a/2\right)\right]$$
$$\cdot \sin\left(k_{x_\gamma}\Delta x_1/2\right)\left[e^{-jk_{y_\gamma}W_1} - 1\right] \quad for \quad \begin{cases} \alpha = 1,2,3,\ldots \\ \beta = 0,1,2,\ldots \end{cases} \tag{2.72}$$

and

$$l^{CV11}_{m_1,n_1} = \frac{j}{\omega\mu_0 LW^2} \sum_{\Gamma} \frac{\epsilon_\Gamma}{k_{x_\gamma} k_{y_\Gamma} k_{z_\Gamma}} \sin\left(k_{x_\gamma}\Delta x_1/2\right)$$
$$\cdot \sin\left[k_{x_\Gamma}\left(x_{1_{m_1}} - L\right)\right] \sin\left[k_{x_\Gamma}\left(x_{1_{n_1}} - L\right)\right]$$
$$\cdot \cos^2\left(k_{y_\Gamma}W\right) \sin\left(k_{y_\Gamma}W\right) \cot\left(k_{z_\Gamma}t\right) \tag{2.73}$$

For the second quadrant of the matrix elements, the coupled cavity terms at BS1 are

$$l^{C1}_{m_1,n_2} = l^{CV12}_{m_1,n_2} = \frac{j}{\omega\mu_0 LWW_2} \sum_{\Gamma} \frac{\epsilon_\Gamma}{k_{x_\gamma} k_{y_\Gamma} k_{z_\Gamma} \sin\left(k_{z_\Gamma}t\right)}$$
$$\cdot \sin\left(k_{x_\gamma}\Delta x_2/2\right) \sin\left[k_{x_\Gamma}\left(x_{1_{m_1}} - L\right)\right] \sin\left[k_{x_\Gamma}\left(x_{2_{n_2}} - L\right)\right]$$
$$\cdot \cos^2\left(k_{y_\Gamma}W\right) \sin\left(k_{y_\Gamma}W_2\right) \tag{2.74}$$

For the third quadrant of the matrix elements, the coupled cavity terms at BS2 are

$$l^{C2}_{m_2,n_1} = l^{CV21}_{m_2,n_1} = \frac{j}{\omega\mu_0 L W^2}\sum_{\Gamma}\frac{\epsilon_\Gamma}{k_{x_\gamma}k_{y_\Gamma}k_{z_\Gamma}\sin\left(k_{z_\Gamma}t\right)}$$
$$\cdot\sin\left(k_{x_\gamma}\Delta x_1/2\right)\sin\left[k_{x_\Gamma}\left(x_{2m_2}-L\right)\right]\sin\left[k_{x_\Gamma}\left(x_{1n_1}-L\right)\right]$$
$$\cdot\cos^2\left(k_{y_\Gamma}W\right)\sin\left(k_{y_\Gamma}W\right) \qquad (2.75)$$

Finally, for the fourth quadrant of matrix elements, the combination of the cavity and halfspace self terms at BS2 is given as

$$l^{CH}_{m_2,n_2} = l^{CV22}_{m_2,n_2} + l^{HS}_{m_2,n_2} \qquad (2.76)$$

where

$$l^{CV22}_{m_2,n_2} = \frac{j}{\omega\mu_0 L W W_2}\sum_{\Gamma}\frac{\epsilon_\Gamma\cos\left(k_{z_\Gamma}t\right)}{k_{x_\gamma}k_{y_\Gamma}k_{z_\Gamma}\sin\left(k_{z_\Gamma}t\right)}$$
$$\cdot\sin\left(k_{x_\gamma}\Delta x_2/2\right)\sin\left[k_{x_\Gamma}\left(x_{2m_2}-L\right)\right]\sin\left[k_{x_\Gamma}\left(x_{2n_2}-L\right)\right]$$
$$\cdot\cos^2\left(k_{y_\Gamma}W\right)\sin\left(k_{y_\Gamma}W_2\right) \qquad (2.77)$$

and

$$l^{HS}_{m_2,n_2} = \begin{cases} \frac{-j\Delta x_2}{\omega\mu_0 2\pi}\frac{e^{-jk_0\left|x_{2m_2}-x_{2n_2}\right|}}{\left|x_{2m_2}-x_{2n_2}\right|} & for \quad m_2 \neq n_2 \\ \frac{-j}{\omega\mu_0\pi W_2}\left[\frac{\Delta x_2}{2}\sinh^{-1}\left(\frac{2W_2}{\Delta x_2}\right)\right. \\ \left. \quad +W_2\sinh^{-1}\left(\frac{\Delta x_2}{2W_2}\right)\right] & for \quad m_2 = n_2 \end{cases} \qquad (2.78)$$

2.6 Rectangular Waveguide Scattering Parameters

The objective of this section is to obtain expressions for the rectangular waveguide scattering parameters S_{11}^{thy} and S_{21}^{thy}. This is accomplished by comparing the ratio of scattered to incident electric field intensities at specific interfaces in the rectangular waveguide [58]. The effect of various slot dimensions on the scattering parameters is also discussed.

2.6.1 Reflection and Transmission Coefficients

A general formulation for computing the reflection and transmission coefficients in a rectangular waveguide is as follows. First, the reflection and transmission coefficients are defined as

$$\Gamma = S_{11}^{thy} \quad ; \quad T = S_{21}^{thy} \tag{2.79}$$

where the ratio of scattered field intensity to incident field intensity for the reflection coefficient is given as

$$\Gamma = \left. \frac{E_z^{s^-}(\overrightarrow{r})}{E_z^{inc}(\overrightarrow{r})} \right|_{y=y_I} \tag{2.80}$$

and the ratio incident and scattered field intensities for the transmission coefficient is given as

$$T = \frac{\left. \left[E_z^{inc}(\overrightarrow{r}) + E_z^{s^+}(\overrightarrow{r}) \right] \right|_{y=y_T}}{\left. E_z^{inc}(\overrightarrow{r}) \right|_{y=y_I}} \tag{2.81}$$

where the incident and scattered fields are added together because both fields are measured at the transmission plane.

The incident field intensity is then given by the TE_y^{10} mode of the electric-field. Based on the modal fields found in section B.2.2.1, this is defined as

$$E_z^{inc}(\overrightarrow{r}) = A_{z_{10}} e_{z_{10}}(x, z)\, e^{-jk_{y_{10}} y} \tag{2.82}$$

The scattered field intensities, based on the mode expansion fields of section B.3.1.1 are

$$E_z^s(\overrightarrow{r}) = -\sum_{\gamma} B_\gamma A_{z_\gamma} e_{z_\gamma}(x, z)\, e^{jk_{y_\gamma} y} \quad \ldots \quad y < -W_1 \tag{2.83}$$

$$E_z^s(\vec{r}) = \sum_{\gamma} C_{\gamma} A_{z_{\gamma}} e_{z_{\gamma}}(x,z)\, e^{-jk_{y_{\gamma}}y} \quad \ldots \quad y > W_1 \tag{2.84}$$

where B_{γ} and C_{γ} are the mode expansion coefficients.

Since the incident electric field is a known TE_{10} mode, along with the properties of mode orthogonality and band-limited guided wave structures, the only mode of interest in the scattered electric fields is also the TE_{10} mode. Thus, equations (2.83) and (2.84) are written in terms of the TE_{10} mode as

$$E_z^s(\vec{r}) = -B_{10} A_{z_{10}} e_{z_{10}}(x,z)\, e^{jk_{y10}y} \quad \ldots \quad y < -W_1 \tag{2.85}$$

$$E_z^s(\vec{r}) = C_{10} A_{z_{10}} e_{z_{10}}(x,z)\, e^{-jk_{y10}y} \quad \ldots \quad y > W_1 \tag{2.86}$$

where solving for the mode expansion coefficients B_{10} and C_{10} gives the desired scattered field intensities. Substituting (2.82), (2.85), and (2.86) into (2.80) and (2.81) respectively, leads to

$$\Gamma = -B_{10} e^{jk_{y10}2y_I} \tag{2.87}$$

and

$$T = e^{-jk_{y10}(y_T - y_I)}\left[1 + C_{10}\right] \tag{2.88}$$

the reflection and transmission coefficients in terms of mode expansion coefficients B_{10} and C_{10} respectively.

Now the mode expansion coefficients, given in equations (B.54) and (B.55), are solved by substituting the slot voltages (determined by the solution to the MoM technique) into these equations and rearranging the solutions so that

$$B_{10} = C_{10} = \frac{\Delta x_1 \sin\left(k_{y_{10}} W_1\right)}{W_1 ab\omega\mu_0 k_{y_{10}}^2} \sum_{n_1=1}^{N_1} V_1\left(x_{1_{n_1}}\right)\cos\left(k_{x_{10}} x_{1_{n_1}}\right) \tag{2.89}$$

where N_1 is the number of slot partitions at BS1.

Substitution of (2.89) into (2.87) and (2.88) gives respectively, the reflection coefficient

$$\Gamma(x,y) = e^{jk_{y10}2y_I}\Gamma(x) \tag{2.90}$$

where

$$\Gamma(x) = -\frac{\Delta x_1 \sin\left(k_{y10}W_1\right)}{W_1 ab\omega\mu_0 k_{y10}^2} \sum_{n_1=1}^{N_1} V_1\left(x_{1n_1}\right)\cos\left(k_{x10}x_{1n_1}\right) \tag{2.91}$$

and the transmission coefficient

$$T(x,y) = e^{-jk_{y10}\left(y_T - y_I\right)}\left[1-\Gamma(x)\right] \tag{2.92}$$

Note that the reflection coefficient in 2.90 is directly related to the slot voltage in 2.91, and the transmission coefficient in 2.92 is related by one minus the same slot voltage. This has physical intuition, in that if the slot voltage goes to zero (ie. the slot is filled with PEC), then the waveguide is restored and complete transmission of the signal is obtained.

2.6.2 Analysis of Slot Dimensions

The purpose of this section is to understand the effect of various slot dimensions (length, width and height) on the rectangular waveguide scattering parameters.

2.6.2.1 Thickness of Slot

The thickness of a standard waveguide wall is approximately $\lambda/15$. Generally in electromagnetics distances of this magnitude have negligible effects on the system. However, the slot thickness due to the waveguide wall thickness, even when the size is small compared to the wavelength, exerts a noticeable effect on the slot admittance. Since the admittance of the slot is significant at non-resonant frequencies, the effect of the wall thickness is very noticeable on the scattering parameters over a given waveguide band. Figure 2.5 shows the effect of various slot thicknesses on the rectangular waveguide scattering parameters versus a frequency range of 8.2 - 12.4 GHz. Notice the upwards shift in resonance frequency and the decrease in bandwidth (increased Q of slot cavity) for the scattering parameters as the slot thickness increases. These results mirror those found by Oliner [47].

2.6.2.2 Length of Slot

The length of a strip dipole is associated with its resonant frequency [55]-[56]. Since the rectangular slot is the complementary problem of a strip dipole, the slot length is therefore also associated with its resonant frequency. Figure 2.6 shows the effect of various slot lengths on the rectangular waveguide scattering parameters versus a frequency range of 8.2 - 12.4 GHz. A constant slot length to width ratio of 1/20 and a slot thickness of 3.25 mm were used to ensure only the effects of the slot length are seen. Also, only 21 frequency points are used in both figures to save on computation time, a little accuracy is lost, but the overall concept is shown very well. The four slot lengths, 1.67 cm, 1.50 cm, 1.36 cm, and 1.25 cm, where chosen since they are resonant at frequencies of 9,10,11, and 12 GHz respectively. The results show the resonances to be just slightly less than the desired value as expected [55], as well as a slightly higher power loss as frequency increases.

2.6.2.3 Width of Slot

The dimensions of the slot are assumed to be long and narrow, with a ratio of one-twentieth chosen as a safe value for application purposes. Here the effect of various slot widths is studied by keeping the length of the slot fixed at 1.50 cm. Figure 2.7 shows the effect of various slot length to width ratios on rectangular waveguide scattering parameters versus a frequency range of 8.2 - 12.4 GHz. The four slot length to width ratios (1/25, 1/20, 1/15, 1/10) are chosen, and it is seen that as the slot width grows, so does the coupling through the slot. However, it is also seen that if the width becomes too great, the assumption of a strictly transverse directed slot electric-field begins to break down. Hence, there is a trade-off between coupling and complexity at around a length to width ratio of 1/15.

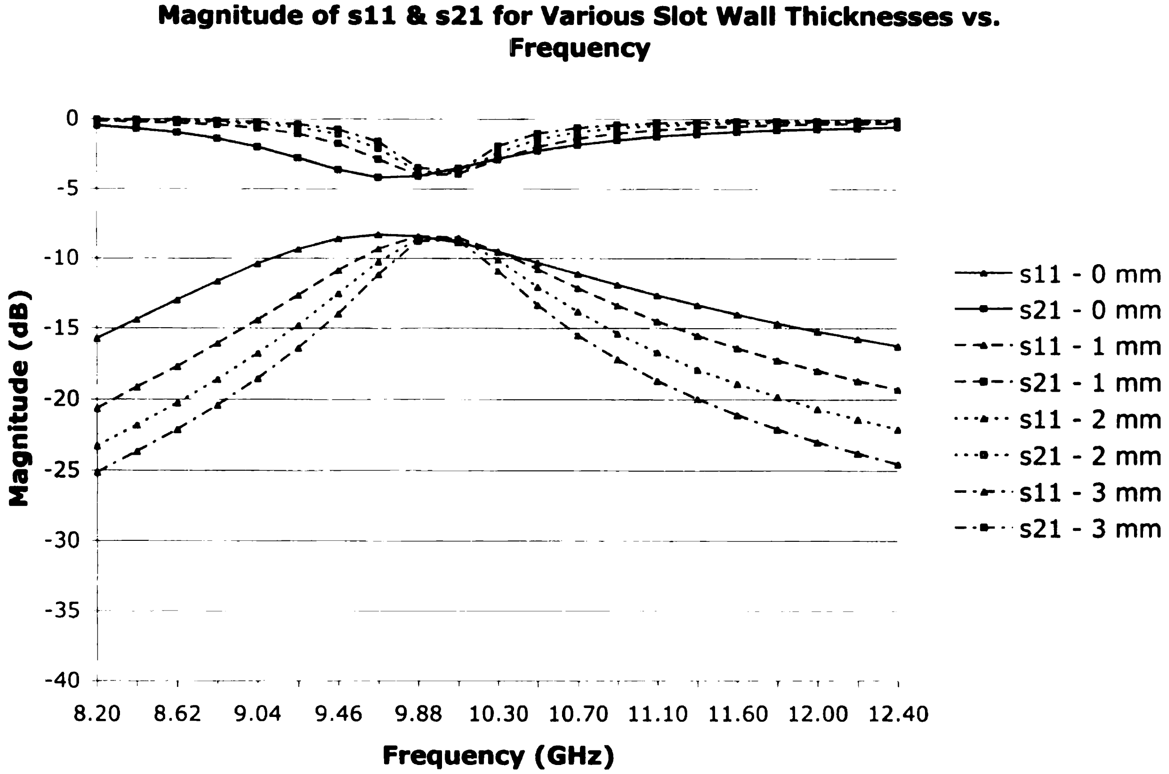

Figure 2.5. Effect of the slot wall thickness on the magnitude (dB) of the waveguide scattering parameters vs. frequency (GHz).

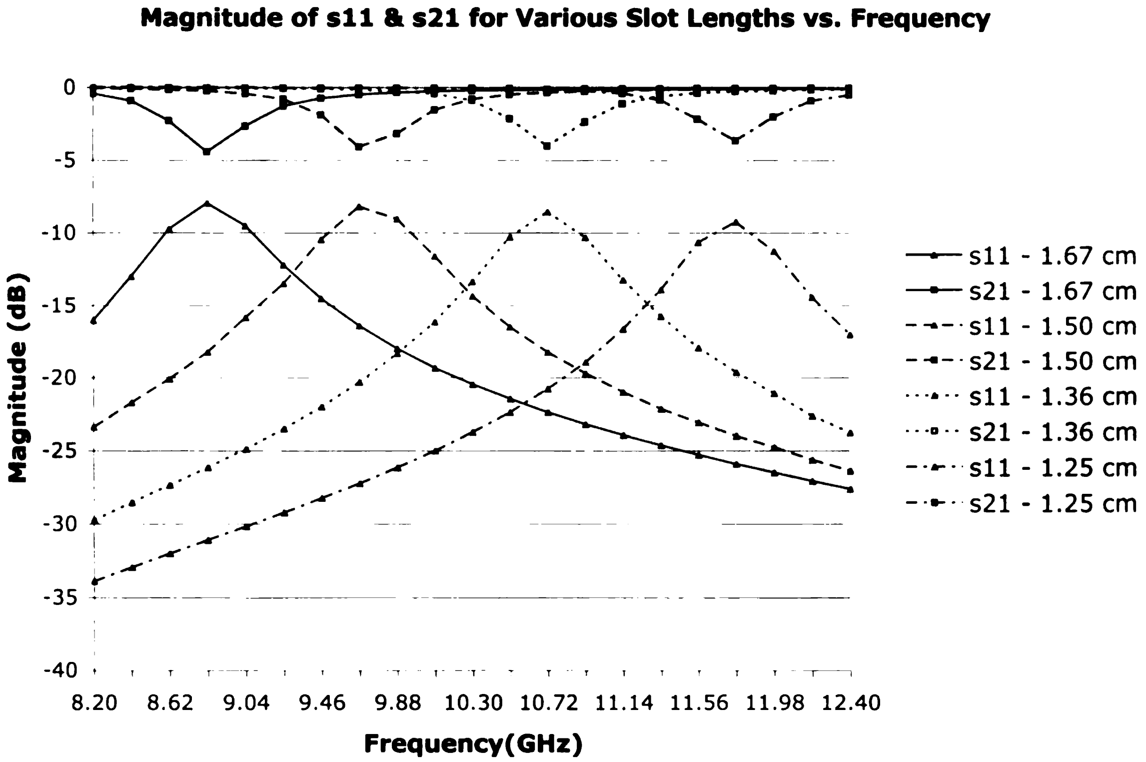

Figure 2.6. Effect of the slot length on the magnitude (dB) of the waveguide scattering parameters vs. frequency (GHz).

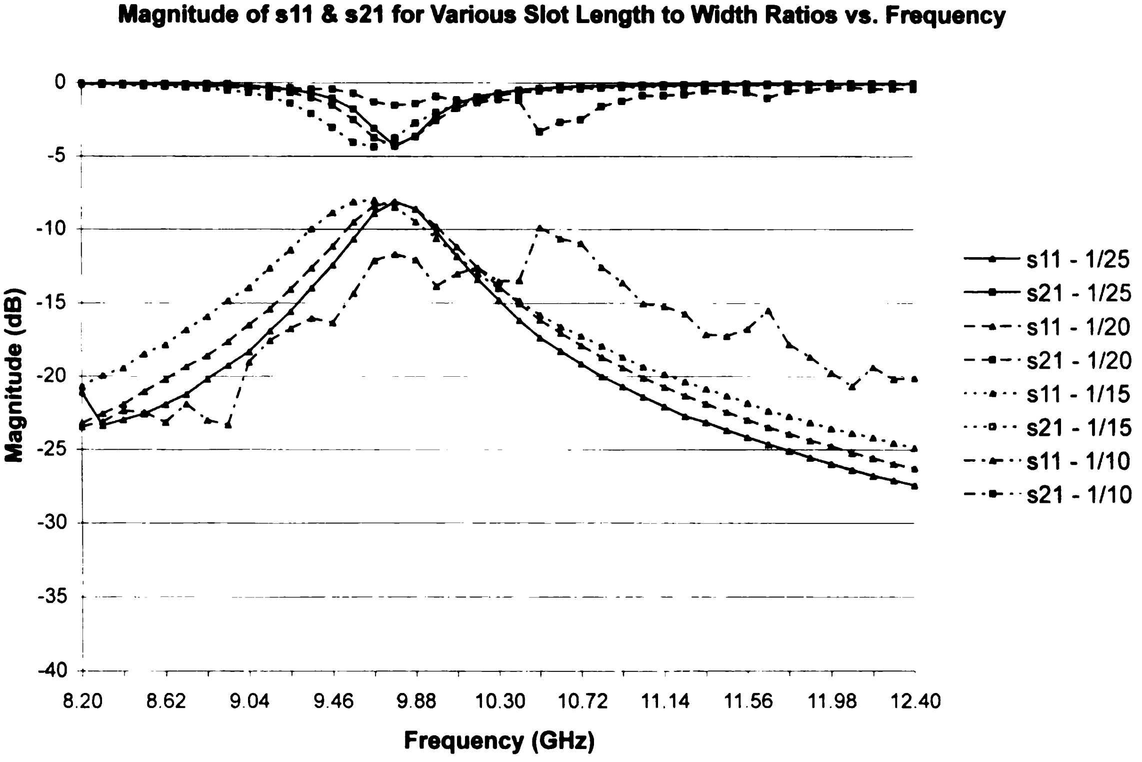

Figure 2.7. Effect of the slot width (using slot length to width ratios) on the magnitude (dB) of the waveguide scattering parameters vs. frequency (GHz).

CHAPTER 3

GREEN'S FUNCTION FOR EM FIELD WITHIN A PEC PARALLEL-PLATE ENVIRONMENT

3.1 Introduction

In this chapter, the MT Hertzian potential dyadic Green's function [61] is derived, for a general 3D current source immersed within a PEC parallel-plate environment. This analysis is utilized in Chapter 4, ultimately leading to the extraction of the constitutive parameters for a lossy PEC backed homogeneous, isotropic media in Chapter 5. Simple relationships are given to extend the MT Hertzian potential dyadic Green's function to electric and magnetic field forms.

3.2 Geometrical Configuration

Consider the PEC parallel-plate waveguide filled with a homogeneous, isotropic media, and excited by an impressed magnetic source as shown in Figure 3.1. The waveguide has fixed dimensions for height $-d < z < 0$ and is infinite in extent in the x, y-plane. The origin is placed at the center of the $z = 0$ PEC plate.

3.3 EM Fields and Helmholtz Equation for MT Hertzian Potential

Various methods are used to identify the electric and magnetic field dyadic Green's functions $\overleftrightarrow{G}^{e}(\vec{r}|\vec{r}')$ and $\overleftrightarrow{G}^{h}(\vec{r}|\vec{r}')$ [62]-[63]. One method involves identifying $\overleftrightarrow{G}^{e}$ and $\overleftrightarrow{G}^{h}$ by directly solving the wave equations for $\vec{E}$ and $\vec{H}$. This yields

$$\nabla^2\vec{E} + k^2\vec{E} = \nabla \times \vec{J}_m \tag{3.1}$$

$$\nabla^2\vec{H} + k^2\vec{H} = j\omega\epsilon\vec{J}_m + \frac{1}{j\omega\mu}\nabla\left(\nabla \cdot \vec{J}_m\right) \tag{3.2}$$

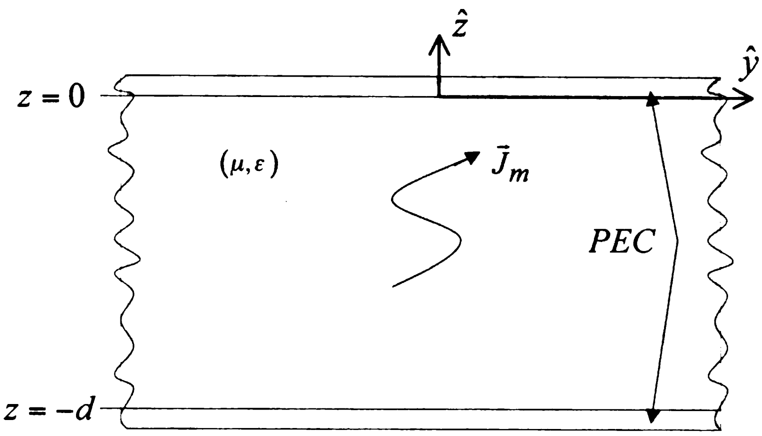

Figure 3.1. Geometrical Configuration: Parallel-plate waveguide filled with a simple media

which have relatively complicated relationships between $\vec{E}$, $\vec{H}$ and $\vec{J}$.

A second method involves using the MT Hertzian potential $\vec{\pi}_h$ as an intermediate step (see Appendix A for further details), which is advantageous since it produces a simpler relationship between $\vec{\pi}_h$ and $\vec{J}$. This relationship is known as the MT Hertzian potential wave equation and is given as

$$\nabla^2\vec{\pi}_h + k^2\vec{\pi}_h = -\frac{\vec{J}_m}{j\omega\mu} \tag{3.3}$$

where $\overleftrightarrow{G}^e$ and $\overleftrightarrow{G}^h$ are then identified by solving (3.3) for $\vec{\pi}_h$ and then computing $\vec{E}$ and $\vec{H}$ using

$$\vec{E} = -j\omega\mu\nabla \times \vec{\pi}_h \tag{3.4}$$

$$\vec{H} = k^2\vec{\pi}_h + \nabla\left(\nabla\cdot\vec{\pi}_h\right) \tag{3.5}$$

Another motivation for using the MT Hertzian potential is that $\vec{\pi}_h$ is less singular than $\vec{E}$ or $\vec{H}$. Thus, the MT Hertzian potential Green's function is derived, and is extended to $\vec{E}$ and $\vec{H}$ forms with equations (3.4) and (3.5) if desired.

3.4 Spectral Representation of Principal and Scattered Waves

In order to identify the MT Hertzian potential Green's function, a solution to the differential equation (3.3) is needed. This is done using the method of superposition where the solution is the addition of a complementary solution and a particular solution. The particular solution represents the principal wave $\vec{\pi}_h^P$ emanating from the magnetic source $\vec{J}_m$ in unbounded space, and the complementary solution represents the waves $\vec{\pi}_h^S$ scattered from boundaries at $z = 0, -d$ in the absence of the source. The total solution for $\vec{\pi}_h$ is therefore

$$\vec{\pi}_h = \vec{\pi}_h^P + \vec{\pi}_h^S \tag{3.6}$$

where $\vec{\pi}_h^P$ and $\vec{\pi}_h^S$ satisfy the respective MT Hertzian potential wave equations

$$\nabla^2 \vec{\pi}_h^P + k^2 \vec{\pi}_h^P = -\frac{\vec{J}_m}{j\omega\mu} \tag{3.7}$$

$$\nabla^2 \vec{\pi}_h^S + k^2 \vec{\pi}_h^S = 0 \tag{3.8}$$

and $k^2 = \omega^2 \mu\epsilon$.

Equations (3.7) and (3.8) are then decomposed into three separate scalar equations each as follows

$$\nabla^2 \pi_{h_\alpha}^P(\vec{r}) + k^2 \pi_{h_\alpha}^P(\vec{r}) = -\frac{J_{m_\alpha}(\vec{r})}{j\omega\mu} \tag{3.9}$$

$$\nabla^2 \pi_{h_\alpha}^S(\vec{r}) + k^2 \pi_{h_\alpha}^S(\vec{r}) = 0 \tag{3.10}$$

where $\alpha = x, y, z$. The solutions of these equations are found using the Fourier transform domain method. It is apparent that the structure is invariant along the x and y directions, thus prompting transformation of those variables using the 2D

Fourier transform pair

$$\Psi\left(\vec{r}\right) = \frac{1}{(2\pi)^2} \int\limits_{-\infty}^{\infty} \int\limits_{-\infty}^{\infty} \tilde{\Psi}\left(\vec{\lambda}, z\right) e^{j\vec{\lambda}\cdot\vec{r}} d^2\lambda \tag{3.11}$$

$$\tilde{\Psi}\left(\vec{\lambda}, z\right) = \int\limits_{-\infty}^{\infty} \int\limits_{-\infty}^{\infty} \Psi\left(\vec{r}\right) e^{-j\vec{\lambda}\cdot\vec{r}} dx dy \tag{3.12}$$

where $\vec{\lambda} = \hat{x}\xi + \hat{y}\eta \left(\Rightarrow \lambda^2 = \vec{\lambda}\cdot\vec{\lambda} = \xi^2 + \eta^2\right)$, $\vec{r} = \hat{x}x + \hat{y}y + \hat{z}z$ and $d^2\lambda = d\xi d\eta$. No transformation with respect to z is applied so boundary conditions may be enforced later at $z = 0, -d$. Applying the Fourier transform differentiation theorem, equations (3.9) and (3.10) become

$$\frac{\partial^2}{\partial z^2} \tilde{\pi}^{P}_{h\alpha}\left(\vec{\lambda}, z\right) - p^2 \tilde{\pi}^{P}_{h\alpha}\left(\vec{\lambda}, z\right) = -\frac{\tilde{J}_{m\alpha}\left(\vec{\lambda}, z\right)}{j\omega\mu} \tag{3.13}$$

$$\frac{\partial^2}{\partial z^2} \tilde{\pi}^{S}_{h\alpha}\left(\vec{\lambda}, z\right) - p^2 \tilde{\pi}^{S}_{h\alpha}\left(\vec{\lambda}, z\right) = 0 \tag{3.14}$$

where $p^2 = \lambda^2 - k^2$ and

$$\tilde{\pi}^{P}_{h\alpha}\left(\vec{\lambda}, z\right) = \int\limits_{-\infty}^{\infty} \int\limits_{-\infty}^{\infty} \pi^{P}_{h\alpha}\left(\vec{r}\right) e^{-j\vec{\lambda}\cdot\vec{r}} dx dy \tag{3.15}$$

$$\tilde{\pi}^{S}_{h\alpha}\left(\vec{\lambda}, z\right) = \int\limits_{-\infty}^{\infty} \int\limits_{-\infty}^{\infty} \pi^{S}_{h\alpha}\left(\vec{r}\right) e^{-j\vec{\lambda}\cdot\vec{r}} dx dy \tag{3.16}$$

$$\tilde{J}_{m\alpha}\left(\vec{\lambda}, z\right) = \int\limits_{-\infty}^{\infty} \int\limits_{-\infty}^{\infty} J_{m\alpha}\left(\vec{r}\right) e^{-j\vec{\lambda}\cdot\vec{r}} dx dy \tag{3.17}$$

The general form of the solution to equations (3.13) and (3.14) is investigated in sections 3.4.1 and 3.4.2.

3.4.1 Principal Wave Representation

The spectral-domain representation of the principal wave is obtained by solving equation (3.13), as dictated by the method of superposition. Since there are no boundaries present, the solution to this second-order partial differential equation is valid for all unbounded space. The solution to equation (3.13) is well-known and the details may be found in [7]. A quick overview of the steps involved is presented here along with the solution.

The first step involves the transformation of the last spatial variable z into the spectral domain. Then, along with the aid of the remaining differentiation theorem, solving for $\tilde{\tilde{\pi}}^P_{h_\alpha}$ gives

$$\tilde{\tilde{\pi}}^P_{h_\alpha}\left(\vec{\lambda},\zeta\right) = \frac{\tilde{\tilde{J}}_{m\alpha}\left(\vec{\lambda},\zeta\right)}{j\omega\mu\left(\zeta^2+p^2\right)} \tag{3.18}$$

Now, the inverse transform is taken to return to the complex λ-plane, ensuring that the z-variable is present for implementing the boundary conditions. After solving the complex ζ-plane analysis using Cauchy's Integral Theorem [64], the desired result for the representation for the principal wave in the complex λ-plane is

$$\tilde{\pi}^P_{h_\alpha}\left(\vec{\lambda},z\right) = \int_{z'} \tilde{G}^P\left(\vec{\lambda};z|z'\right)\frac{\tilde{J}_{m\alpha}\left(\vec{\lambda},z'\right)}{j\omega\mu}dz' \tag{3.19}$$

In this, the spectral-domain principal wave MT Hertzian potential Green's function is given by

$$\tilde{G}^P\left(\vec{\lambda};z|z'\right) = \frac{e^{-p\left|z-z'\right|}}{2p} \tag{3.20}$$

with z as the field point, z' as the source point and p is the spectral-domain propagation factor.

3.4.2 Scattered Wave Representation

The spectral-domain representation for the scattered waves is obtained from equation (3.14). The well-known solution of this second-order partial differential equation is

$$\tilde{\pi}_{h_\alpha}^{S}\left(\vec{\lambda}, z\right) = W_\alpha^{+}\left(\vec{\lambda}\right) e^{-pz} + W_\alpha^{-}\left(\vec{\lambda}\right) e^{pz} \tag{3.21}$$

where $W_\alpha^{\pm}$ are the complex amplitude coefficients of the up and down traveling reflected waves.

3.4.3 Total Wave Representation

The spectral-domain representation of the total wave is obtained by superposing the results from the previous two sections. This leads to the following result

$$\tilde{\pi}_{h_\alpha} = \tilde{\pi}_{h_\alpha}^{P} + \tilde{\pi}_{h_\alpha}^{S} = \int\limits_{z'} \frac{e^{-p\left|z-z'\right|}}{2p} \frac{\tilde{J}_{m_\alpha}}{j\omega\mu} dz' + W_\alpha^{+} e^{-pz} + W_\alpha^{-} e^{pz} \tag{3.22}$$

where functional dependence in the above equation has been dropped for notational convenience. Noting that the distance in the exponential for z-dependance integral has a sign change based on whether the observer location is greater or less than the source location, given as

$$\left|z - z'\right| = \begin{cases} z - z' & \ldots z > z' \\ z' - z & \ldots z < z' \end{cases} \tag{3.23}$$

allows equation (3.22) be written respectively as

$$\tilde{\pi}_{h_\alpha} = V_\alpha^{+} e^{-pz} + W_\alpha^{+} e^{-pz} + W_\alpha^{-} e^{pz} \quad \ldots z > z' \tag{3.24}$$

$$\tilde{\pi}_{h_\alpha} = V_\alpha^{-} e^{pz} + W_\alpha^{+} e^{-pz} + W_\alpha^{-} e^{pz} \quad \ldots z < z' \tag{3.25}$$

where

$$V_\alpha^\pm = V_\alpha^\pm\left(\vec{\lambda}\right) = \int_{z'} \frac{e^{\pm pz'}}{2p} \frac{\tilde{J}_{m\alpha}\left(\vec{\lambda}, z'\right)}{j\omega\mu} dz' \tag{3.26}$$

are associated with the up and down traveling waves launched by the source. This also helps simplify the notation when implementing the boundary conditions. To obtain a unique solution for the spectral-domain MT Hertzian potential, six boundary conditions are enforced to solve the the six unknown spectral-domain coefficients. These spectral coefficients are determined in the next section.

3.5 Computation of Spectral Coefficients

To determine the spectral coefficients $W_\alpha^\pm$, boundary conditions are enforced on the total wave representation of the spectral-domain MT Hertzian potential. Since the boundaries of the parallel-plate structure are PECs, the well-known relationship that the tangential electric field equals zero on the surface of the PEC [58] is used at the boundaries $z = 0, -d$. Leading to the expansion of equation (3.4) in terms of the tangential components E_x and E_y as

$$E_x = -j\omega\mu \left[\frac{\partial \pi_{h_z}}{\partial y} - \frac{\partial \pi_{h_y}}{\partial z}\right]; E_y = -j\omega\mu \left[\frac{\partial \pi_{h_x}}{\partial z} - \frac{\partial \pi_{h_z}}{\partial x}\right] \tag{3.27}$$

Now, using the educated conjecture that any J_{m_α}, for $\alpha = x, y, z$, leads only to the same π_{h_α}, and enforcing the previously stated boundary conditions at a PEC interface, the following set of boundary conditions on the spectral-domain MT Hertzian potential are found

$$\frac{\partial \pi_{h_\alpha}}{\partial z} = 0 \quad \cdots \alpha = x, y \tag{3.28}$$

$$\pi_{h_z} = 0 \tag{3.29}$$

where equation (3.28) is the tangential boundary conditions, and equation (3.29) is the normal boundary condition. These boundary conditions are implemented in sections 3.5.1 and 3.5.2.

3.5.1 Tangential Components ($\alpha = x, y$)

Enforcing the first tangential boundary condition (at the $z = 0$ interface) by substituting (3.24) into (3.28) leads to the following expression

$$p\left(-V_\alpha^+ - W_\alpha^+ + W_\alpha^-\right) = 0 \quad \cdots \alpha = x, y \tag{3.30}$$

where solving (3.30) for W_α^- gives

$$W_\alpha^- = V_\alpha^+ + W_\alpha^+ \quad \cdots \alpha = x, y \tag{3.31}$$

Then, implementing the second tangential boundary condition (at the $z = -d$ interface) by substituting (3.25) into (3.28) results in

$$p\left(V_\alpha^- e^{-pd} - W_\alpha^+ e^{pd} + W_\alpha^- e^{-pd}\right) = 0 \quad \cdots \alpha = x, y \tag{3.32}$$

where solving (3.32) for W_α^+ gives

$$W_\alpha^+ = e^{-2pd}\left(V_\alpha^- + W_\alpha^-\right) \quad \cdots \alpha = x, y \tag{3.33}$$

Now, the substitution of (3.31) into (3.33), combined with solving for W_α^+, leads to

$$W_\alpha^+ = \frac{e^{-pd}\left(V_\alpha^- + V_\alpha^+\right)}{e^{pd} - e^{-pd}} \quad \cdots \alpha = x, y \tag{3.34}$$

followed by substituting (3.34) into (3.31), and solving for W_α^-, giving

$$W_\alpha^- = \frac{V_\alpha^- e^{-pd} + V_\alpha^+ e^{pd}}{e^{pd} - e^{-pd}} \quad \cdots \alpha = x, y \tag{3.35}$$

where the tangential spectral-domain coefficients $W_\alpha^\pm$ are only in terms of known coefficients $V_\alpha^\pm$.

All that remains to find the tangential spectral-domain MT Hertzian potential is to substitute (3.34) and (3.35) into (3.22) and manipulate the expression into its final form, given as

$$\tilde{\pi}_{h_\alpha}\left(\vec{\lambda}, z\right) = \int_{-d}^{0} dz' \tilde{G}^t\left(\vec{\lambda}; z|z'\right) \frac{\tilde{J}_{m\alpha}\left(\vec{\lambda}, z\right)}{j\omega\mu} dz' \tag{3.36}$$

where $\tilde{G}^t$ is the tangential spectral-domain Green's function

$$\tilde{G}^t\left(\vec{\lambda}; z|z'\right) = \tilde{G}^P\left(\vec{\lambda}; z|z'\right) + \tilde{G}^{St}\left(\vec{\lambda}; z|z'\right) \tag{3.37}$$

which is split into principal $\tilde{G}^P$ and scattered $\tilde{G}^{St}$ portions as follows

$$\tilde{G}^P\left(\vec{\lambda}; z|z'\right) = \frac{e^{-p\left|z-z'\right|}}{2p} \tag{3.38}$$

$$\tilde{G}^{St}\left(\vec{\lambda}; z|z'\right) = \frac{e^{-p\left(z-z'+d\right)} + e^{-p\left(z+z'+d\right)} + e^{-p\left(-z+z'+d\right)} + e^{-p\left(-z-z'-d\right)}}{2p\left(e^{pd} - e^{-pd}\right)} \tag{3.39}$$

This form of the Green's function is very convenient for obtaining physical insight into its behavior (discussed in section 3.7), however, another form is presented in section 3.6 that is more practical for use in Chapter 4.

3.5.2 Normal Component ($\alpha = z$)

Enforcing the first normal boundary condition (at the $z = 0$ interface) by substituting (3.24) into (3.29) and solving for W_z^- leads to

$$W_z^- = -V_z^+ - W_z^+ \tag{3.40}$$

Then, implementing the second normal boundary condition (at the $z = -d$ interface) by substituting (3.25) into (3.29) and solving for W_z^+ this time gives

$$W_z^+ = -e^{-2pd}\left(V_z^- + W_z^-\right) \tag{3.41}$$

Now, in the same manner as the tangential components, substitution of (3.40) into (3.41), combined with solving for W_α^+, leads to

$$W_z^+ = \frac{e^{-pd}\left(-V_z^- + V_z^+\right)}{e^{pd} - e^{-pd}} \tag{3.42}$$

followed by substitution of (3.42) into (3.40), and solving for W_α^-, giving

$$W_z^- = \frac{V_z^- e^{-pd} - V_z^+ e^{pd}}{e^{pd} - e^{-pd}} \tag{3.43}$$

where the normal spectral-domain coefficients $W_z^\pm$ are only in terms of known coefficients $V_z^\pm$.

Again, similarly to the tangential components, all that remains to find the normal spectral-domain MT Hertzian potential is to substitute (3.42) and (3.43) into (3.22) and manipulate the expression into its finally form, given as

$$\tilde{\pi}_{h_z}\left(\vec{\lambda}, z\right) = \int_{-d}^{0} dz' \tilde{G}^n\left(\vec{\lambda}; z|z'\right) \frac{\tilde{J}_{m_z}\left(\vec{\lambda}, z\right)}{j\omega\mu} dz' \tag{3.44}$$

where $\tilde{G}^n$ is the normal spectral-domain Green's function

$$\tilde{G}^n\left(\vec{\lambda}; z|z'\right) = \tilde{G}^P\left(\vec{\lambda}; z|z'\right) + \tilde{G}^{Sn}\left(\vec{\lambda}; z|z'\right) \tag{3.45}$$

which is split into principal $\tilde{G}^P$ and scattered $\tilde{G}^{Sn}$ portions as follows

$$\tilde{G}^P\left(\vec{\lambda}; z|z'\right) = \frac{e^{-p\left|z-z'\right|}}{2p} \tag{3.46}$$

$$\tilde{G}^{Sn}\left(\vec{\lambda}; z|z'\right) = \frac{e^{-p\left(z-z'+d\right)} - e^{-p\left(z+z'+d\right)} + e^{-p\left(-z+z'+d\right)} - e^{-p\left(-z-z'-d\right)}}{2p\left(e^{pd} - e^{-pd}\right)} \tag{3.47}$$

3.6 Dyadic Green's Function

The purpose of this section is to present a more compact and practical version of the MT Hertzian potential dyadic Green's function for a PEC parallel-plate region. The lack of physical insight upon first looking at this form is the only consequence of expressing it in this manner. Since, in practical use the MT Hertzian potential is used in the space-domain, the dyadic Green's function presented is also in the space-domain. The space-domain MT Hertzian potential is represented as

$$\vec{\pi}_h\left(\vec{r}\right) = \int_V dV' \overleftrightarrow{G}\left(\vec{r}|\vec{r}'\right) \frac{\vec{J}_m\left(\vec{r}'\right)}{j\omega\mu} \tag{3.48}$$

where $\overleftrightarrow{G}$ is the space-domain dyadic Green's function [63], and is represented as follows

$$\overleftrightarrow{G}\left(\vec{r}|\vec{r}'\right) = \overleftrightarrow{I} G^\alpha\left(\vec{r}|\vec{r}'\right) = \hat{x} G^\alpha\left(\vec{r}|\vec{r}'\right)\hat{x} + \hat{y} G^\alpha\left(\vec{r}|\vec{r}'\right)\hat{y} + \hat{z} G^\alpha\left(\vec{r}|\vec{r}'\right)\hat{z} \tag{3.49}$$

$$G^\alpha\left(\vec{r}|\vec{r}'\right) = \frac{1}{(2\pi)^2} \int_{-\infty}^{\infty}\int_{-\infty}^{\infty} \tilde{G}^\alpha\left(\vec{\lambda}; z|z'\right) e^{j\vec{\lambda}\cdot\left(\vec{r}-\vec{r}'\right)} d^2\lambda \tag{3.50}$$

and $\tilde{G}^{\alpha}$ is the spectral-domain Green's function, given as

$$\tilde{G}^{\alpha}\left(\vec{\lambda}; z|z'\right) = \frac{\cosh p\left(d - |z - z'|\right) \pm \cosh p\left(d + z + z'\right)}{2p\sinh\left(pd\right)} \tag{3.51}$$

where the ± refers to the tangential (+) and normal (-) cases respectively.

It is noted that the dyad has only diagonal entries since no coupling between sources occurs. This is because the boundary condition at a PEC requires only the same potential component as the source component to satisfy the boundary condition.

3.7 Physical Observations

In this section, equations (3.37) and (3.45) are analyzed to gain physical insight into the behavior of the waves in the PEC parallel-plate region. It is noted that the exponentials in both (3.38),(3.39) and (3.46),(3.47) respectively, are the same, thus only the independent terms are analyzed. Referencing the geometry in Figure 3.2, consider first the wave that travels directly from the source point z' to the field point z while traversing a distance of $z - z'$. Since this wave does not reflect off either of the PEC walls it is associated with the principal wave in equations (3.38) and (3.46).

Next, the second wave reflects off both of the PEC walls while traveling a distance of $z - z' + 2d$, thus, it is associated with the first term of equations (3.39) and (3.47). The third wave is associated with the second term of the same equations since it only experiences one reflection and travels a distance of $z + z' + 2d$. Similar discussions show that the fourth and fifth waves are associated with the third and fourth terms the same equations as waves 2 and 3. Note that since waves 2-5 scatter off the top ($z = 0$) and/or bottom ($z = -d$) plates they are associated with the scattered waves.

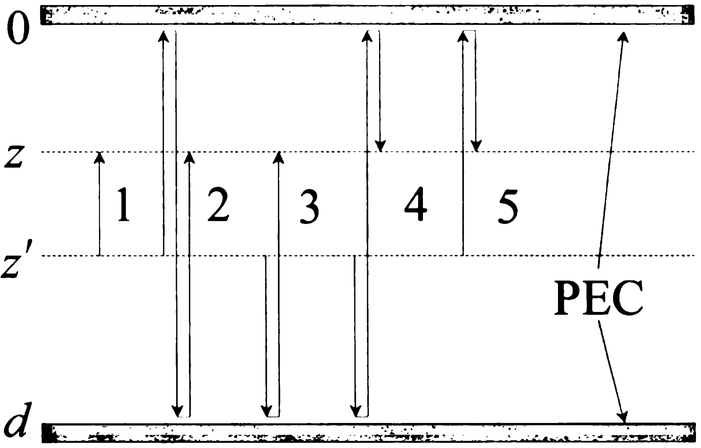

Figure 3.2. Physical observations of the waves within a parallel-plate waveguide

CHAPTER 4

RECTANGULAR WAVEGUIDE RADIATING THROUGH A TRANSVERSE SLOT INTO PARALLEL-PLATE WAVEGUIDE FILLED WITH A SIMPLE MEDIA

4.1 Introduction

The formulation for a finite-thickness transverse slot centered in the broad wall of a rectangular waveguide, radiating into a parallel-plate waveguide filled with a homogeneous, isotropic media, is considered in this chapter. Specfically, the reflection and transmission coefficients for the rectangular waveguide are sought. This is because they are ultimately used in Chapter 5 to perform the complex constitutive parameter extraction on the media in the parallel-plate waveguide. A majority of the formulation provided next mirrors the formulation provided in Chapter 2, thus not all details are repeated herein.

The first step in the formulation is to develop representations of the fields in the three different regions (WG, CV, and PP). Next, IEs are developed by satisfying the continutity of the tangential fields at the two interfaces (BS1 and BS2) between the three regions. The final step is to solve the coupled IEs using a MoM technique for the unknown slot voltages, which in turn identify the scattered fields in the rectangular waveguide and ultimately the desired reflection and transmission coefficients.

4.2 Geometrical Configuration

Consider a rectangular waveguide, on top of an infinite PEC parallel-plate waveguide filled with a homogeneous, isotropic media, with a transverse slot cut in the bottom wall as shown in Figure 4.1.

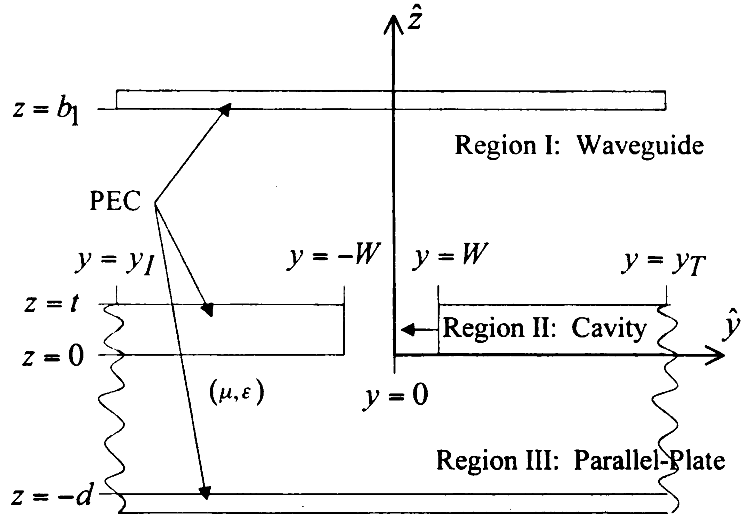

Figure 4.1. Geometrical Configuration: Rectangular waveguide radiating through a transverse slot into a parallel-plate waveguide filled with a simple media

4.3 Field Representations

In order to develop the desired IEs a representation of the fields in the three regions is needed. To generate the appropriate set of field equations a knowledge of the sources is necessary. The equivalent currents that maintain the fields in the three regions are therefore needed.

4.3.1 Equivalent Currents

The equivalent currents necessary to represent the fields in the three regions for this formulation, are exactly the same as those developed in Section 2.3.1 for the formulation in Chapter 2, and are given as

$$K_{m1}^{+}\left(\vec{r_1}'\right) = \hat{x}E_{y1}^{+}\left(\vec{r_1}'\right) \tag{4.1}$$

$$K_{m1}^{-}\left(\vec{r_1}'\right) = -\hat{x}E_{y1}^{-}\left(\vec{r_1}'\right) \tag{4.2}$$

$$K_{m2}^{+}\left(\vec{r_2}'\right) = \hat{x}E_{y2}^{+}\left(\vec{r_2}'\right) \tag{4.3}$$

$$K_{m2}^{-}\left(\vec{r_2}'\right) = -\hat{x}E_{y2}^{-}\left(\vec{r_2}'\right) \tag{4.4}$$

where (4.1) corresponds to the waveguide equivalent magnetic current, (4.2) and (4.3) to the cavity equivalent magnetic currents at BS1 and BS2 respectively, and (4.4) to the parallel-plate equivalent magnetic current. Note that all the equivalent currents have only an x-directed component.

4.3.2 Total Fields in each Region

Using the general field relations from Chapter 2 (reference section 2.3.2), the principle of superposition [58], and the knowledge that the equivalent currents have only an x-directed component, the magnetic field is written in terms of only the x-component as follows

$$H_x\left(\vec{r}\right) = \left(\frac{\partial^2}{\partial x^2} + k^2\right)\pi_{h_x}\left(\vec{r}\right) \tag{4.5}$$

where π_{h_x} is the x-component of the MT Hertzian potential given as

$$\pi_{h_x}\left(\vec{r}\right) = \int_{S_a} G_x\left(\vec{r}|\vec{r}'\right)\frac{K_{m_x}\left(\vec{r}'\right)}{j\omega\mu}dS_a' \tag{4.6}$$

with G_x as the x-component of the dyadic Green's function and K_{m_x} as the equivalent magnetic current for each specific region.

The total magnetic field in region 1 is then written as follows

$$H_x^{region1}\left(\vec{r_1}\right) = H_x^{inc}\left(\vec{r_1}\right) + H_x^{WGS}\left(\vec{r_1}\right) \tag{4.7}$$

where H_x^{inc} is the incident wave in the rectangular waveguide, and H_x^{WGS} is the waves scattered by the transverse slot in the rectangular waveguide. In a similar manner, the total magnetic field in region 2 is

$$H_x^{region2}\left(\vec{r_l}\right) = H_x^{CV1}\left(\vec{r_l}\right) + H_x^{CV2}\left(\vec{r_l}\right) \quad \cdots for \quad l = 1,2 \tag{4.8}$$

where H_x^{CV1} is the waves scattered by the tranverse slot at $z = t$ in the cavity region, and H_x^{CV2} is the waves scattered by the transverse slot at $z = 0$. Finally, the total magnetic field in region 3 is

$$H_x^{region3}\left(\vec{r_2}\right) = H_x^{PP}\left(\vec{r_2}\right) \tag{4.9}$$

where H_x^{PP} is the waves scattered by the transverse slot in the parallel-plate region.

4.3.3 MT Hertzian Potentials in terms of Equivalent Currents

All that remains to fully represent the fields in each region, is to define the MT Hertzian potentials associated with the total fields in equations (4.7-4.9). This is accomplished by substituting equations (4.1-4.4) into equation (4.6) and defining the Green's functions for each region, leading to

$$\pi_{h_x}^{WGS}\left(\vec{r_1}\right) = \int_{S_1} G_{WG}\left(\vec{r_1}|\vec{r_1}'\right)\frac{E_{y1}^{+}\left(\vec{r_1}'\right)}{j\omega\mu_0}dS_1' \tag{4.10}$$

$$\pi_{h_x}^{CV1}\left(\vec{r_l}\right) = \int_{S_1} -G_{CV}\left(\vec{r_l}|\vec{r_1}'\right)\frac{E_{y1}^{-}\left(\vec{r_1}'\right)}{j\omega\mu_0}dS_1' \tag{4.11}$$

$$\pi_{h_x}^{CV2}\left(\vec{r_l}\right) = \int_{S_2} G_{CV}\left(\vec{r_l}|\vec{r_2}'\right)\frac{E_{y2}^{+}\left(\vec{r_2}'\right)}{j\omega\mu_0}dS_2' \tag{4.12}$$

$$\pi_{h_x}^{PP}\left(\vec{r_2}\right) = \int_{S_2} -G_{PP}\left(\vec{r_2}|\vec{r_2}'\right)\frac{E_{y2}^{-}\left(\vec{r_2}'\right)}{j\omega\mu_0}dS_2' \tag{4.13}$$

where (4.11-4.12) is observed at either BS1 or BS2. The Green's function for the rectangular waveguide due to a transverse slot is given as

$$\begin{aligned} G_{WG}\left(\vec{r_1}|\vec{r_1}'\right) = {} & \tfrac{1}{ab}\textstyle\sum_\gamma \frac{\epsilon_\gamma}{jk_{y_\gamma}}\sin\left[k_{x_\gamma}\left(x_1 - a/2\right)\right]\sin\left[k_{x_\gamma}\left(x_1' - a/2\right)\right] \\ & \cdot e^{-jk_{y_\gamma}\left|y_1-y_1'\right|}\cos\left[k_{z_\gamma}\left(z_1 - t\right)\right]\cos\left[k_{z_\gamma}\left(z_1' - t\right)\right] \end{aligned} \tag{4.14}$$

The Green's function for the rectangular cavity is given by

$$\begin{aligned} G_{CV}\left(\vec{r_l}|\vec{r_l}'\right) = {} & \frac{-2}{a_c b_c} \sum\nolimits_{\Gamma} \frac{\epsilon_{\Gamma}}{k_{z_{\Gamma}} \sin\left(k_{z_{\Gamma}} c_c\right)} \\ & \cdot \sin\left[k_{x_{\Gamma}}\left(x_l - a_c/2\right)\right] \sin\left[k_{x_{\Gamma}}\left(x_l' - a_c/2\right)\right] \\ & \cdot \cos\left[k_{y_{\Gamma}}\left(y_l - b_c/2\right)\right] \cos\left[k_{y_{\Gamma}}\left(y_l' - b_c/2\right)\right] \\ & \cdot \left[\begin{array}{lll} \cos\left[k_{z_{\Gamma}}\left(z_l - c_c\right)\right] \cos\left(k_{z_{\Gamma}} z_l'\right) & for & z_l > z_l' \\ \cos\left(k_{z_{\Gamma}} z_l\right) \cos\left[k_{z_{\Gamma}}\left(z_l' - c_c\right)\right] & for & z_l < z_l' \end{array} \right] \end{aligned} \tag{4.15}$$

and the Green's function for the parallel-plate waveguide from Chapter 3 is

$$G_{PP}\left(\vec{r_2}|\vec{r_2}'\right) = \int_{-\infty}^{\infty} \int_{-\infty}^{\infty} d^2\lambda \frac{e^{j\vec{\lambda}\cdot\left(\vec{\rho_2} - \vec{\rho_2}'\right)} \cosh\left(pd\right)}{\left(2\pi\right)^2 p \sinh\left(pd\right)} \tag{4.16}$$

and the spectral wavenumber is

$$p^2 = \lambda^2 - k^2 = \xi^2 + \eta^2 - k^2 \tag{4.17}$$

The Neumann's number for the waveguide and cavity regions respectively is

$$\epsilon_{(\gamma,\Gamma)} = \begin{cases} 1 \quad for \quad \beta_{(wg,cv)} = 0 \\ 2 \quad for \quad \beta_{(wg,cv)} \neq 0 \end{cases} \tag{4.18}$$

and the wavenumbers for both the waveguide and cavity regions respectively are

$$\begin{aligned} k_{x_{(\gamma,\Gamma)}} &= \frac{\alpha_{(wg,cv)}\pi}{a_{(wg,cv)}}, \alpha_{(wg,cv)} = 1, 2, 3, \ldots \\ k_{z_{(\gamma,\Gamma)}} &= \frac{\beta_{(wg,cv)}\pi}{b_{(wg,cv)}}, \beta_{(wg,cv)} = 0, 1, 2, \ldots \\ k^2_{c_{(\gamma,\Gamma)}} &= k_0^2 - k^2_{y_{(\gamma,\Gamma)}} = k^2_{x_{(\gamma,\Gamma)}} + k^2_{z_{(\gamma,\Gamma)}} \end{aligned} \tag{4.19}$$

Details of equations (4.14) and (4.15) are found in Appendix B. These field representations for the three regions are now used to develop IEs in the next section.

4.4 Development of the Coupled MFIEs

The MFIEs at BS1 and BS2 are developed in a similar manner as those developed in Chapter 2 (reference section 2.4).

4.4.1 Development of the MFIDEs

MFIDEs are developed first, followed by solving the second-order partial-differenital equations, to arrive at the desired MFIEs.

4.4.1.1 BS1

The MFIDE at BS1 is developed by invoking the continutity of tangential magnetic fields at the interface ($z = t$) giving

$$H_x^{region1}(\vec{r_1}) = H_x^{region2}(\vec{r_1}) \tag{4.20}$$

then, substituting equations (4.7) and (4.8) into equation (4.20) leads to

$$H_x^{inc}(\vec{r_1}) + H_x^{WGS}(\vec{r_1}) = H_x^{CV1}(\vec{r_1}) + H_x^{CV2}(\vec{r_1}) \tag{4.21}$$

finally, substituting (4.6) into (4.5) and then (4.10-4.12) into the respective magnetic field representation, leads to the first MFIDE result

$$\left(\frac{\partial^2}{\partial x^2} + k_0^2\right)\left\{\int_{S_1} \frac{E_{y1}(\vec{r_1}')}{j\omega\mu_0} G_{WC}(\vec{r_1}|\vec{r_1}')\, dS_1' \right.$$
$$\left. - \int_{S_2} \frac{E_{y2}(\vec{r_2}')}{j\omega\mu_0} G_{CV}(\vec{r_1}|\vec{r_2}')\, dS_2' \right\} = -H_x^{inc}(\vec{r_1}) \tag{4.22}$$

where

$$G_{WC}(\vec{r_1}|\vec{r_1}') = G_{WG}(\vec{r_1}|\vec{r_1}') + G_{CV}(\vec{r_1}|\vec{r_1}') \tag{4.23}$$

Note that the continuity of the electric fields across the two interfaces is enforced by making $E_{y1}^{+} = E_{y1}^{-}$ and $E_{y2}^{+} = E_{y2}^{-}$.

4.4.1.2 BS2

Similarly, the MFIDE at BS2 is developed by invoking the continutity of the tangential magnetic field at the interface ($z = 0$) giving

$$H_x^{region2}\left(\vec{r_2}\right) = H_x^{region3}\left(\vec{r_2}\right) \tag{4.24}$$

where substitution of equations (4.8) and (4.9) into equation (4.24) gives

$$H_x^{CV1}\left(\vec{r_2}\right) + H_x^{CV2}\left(\vec{r_2}\right) = H_x^{PP}\left(\vec{r_2}\right) \tag{4.25}$$

Substituting (4.6) into (4.5) and then (4.11-4.13) into the respective magnetic field representation, leads to

$$\begin{aligned}
&\left(\frac{\partial^2}{\partial x^2} + k_0^2\right) \int_{S_1} -\frac{E_{y1}^{-}\left(\vec{r_1}'\right)}{j\omega\mu_0} G_{CV}\left(\vec{r_2}|\vec{r_1}'\right) dS_1' \\
&+ \left(\frac{\partial^2}{\partial x^2} + k_0^2\right) \int_{S_2} \frac{E_{y2}^{+}\left(\vec{r_2}'\right)}{j\omega\mu_0} G_{CV}\left(\vec{r_2}|\vec{r_2}'\right) dS_2' \\
&= \left(\frac{\partial^2}{\partial x^2} + k^2\right) \int_{S_2} -\frac{E_{y2}^{-}\left(\vec{r_2}'\right)}{j\omega\mu} G_{PP}\left(\vec{r_2}|\vec{r_2}'\right) dS_2'
\end{aligned} \tag{4.26}$$

By adding and subtracting k_0^2 to equation (4.26) and doing some simple mathematical manipulations, the MFIDE is written as

$$\begin{aligned}
&\left(\frac{\partial^2}{\partial x^2} + k_0^2\right) \left\{ \int_{S_1} \frac{E_{y1}\left(\vec{r_1}'\right)}{j\omega\mu_0} G_{CV}\left(\vec{r_2}|\vec{r_1}'\right) dS_1' \right. \\
&\left. - \int_{S_2} \frac{E_{y2}\left(\vec{r_2}'\right)}{j\omega} G_{CP}\left(\vec{r_2}|\vec{r_2}'\right) dS_2' \right\} = \bar{k}^2 \int_{S_2} \frac{E_{y2}\left(\vec{r_2}'\right)}{j\omega\mu} G_{PP}\left(\vec{r_2}|\vec{r_2}'\right) dS_2'
\end{aligned} \tag{4.27}$$

where

$$\bar{k}^2 = k^2 - k_0^2 \tag{4.28}$$

and

$$G_{CP}\left(\vec{r_2}|\vec{r_2}'\right) = \frac{G_{CV}\left(\vec{r_2}|\vec{r_2}'\right)}{\mu_0} + \frac{G_{PP}\left(\vec{r_2}|\vec{r_2}'\right)}{\mu} \tag{4.29}$$

This form is useful when solving the partial-differential equations in the next section.

4.4.2 Solving the Second-Order Partial-Differential Equation

The technique used to solve the second-order partial-differential equations in this section is also used in Chapter 2 (reference Section 2.4.2).

4.4.2.1 MFIE at BS1

The integro-differential equation (4.26) is written in the form

$$\left(\frac{\partial^2}{\partial x^2} + k_0^2\right) F_1\left(\vec{r_1}\right) = A_1\left(\vec{r_1}\right) \tag{4.30}$$

where

$$\begin{aligned} F_1\left(\vec{r_1}\right) = & \int_{S_1} \frac{E_{y1}\left(\vec{r_1}'\right)}{j\omega\mu_0} G_{WC}\left(\vec{r_1}|\vec{r_1}'\right) dS_1' \\ & - \int_{S_2} \frac{E_{y2}\left(\vec{r_2}'\right)}{j\omega\mu_0} G_{CV}\left(\vec{r_1}|\vec{r_2}'\right) dS_2' \end{aligned} \tag{4.31}$$

is in the form of the MT Hertzian potential and

$$A_1\left(\vec{r_1}\right) = -H_x^{inc}\left(\vec{r_1}\right) = -A_{10}\left[(\pi/a)^2 - k_0^2\right]\cos(\pi x_1/a)e^{-jk_{y10}y_1} \tag{4.32}$$

is the forcing term based on the incident x-directd magnetic field. Solving this partial differential equation in terms of a complementary and particular solution (details in section 2.4.2.1) and then superposing the two solutions leads to the MFIE at BS1

$$\int_{S_1} \frac{E_{y1}\left(\vec{r_1}'\right)}{j\omega\mu_0} G_{WC}\left(\vec{r_1}|\vec{r_1}'\right) dS_1' - \int_{S_2} \frac{E_{y2}\left(\vec{r_2}'\right)}{j\omega\mu_0} G_{CV}\left(\vec{r_1}|\vec{r_2}'\right) dS_2'$$
$$= \tilde{C}_1\left(y_1\right)\cos\left(k_0 x_1\right) + D_1\left(y_1\right)\sin\left(k_0 x_1\right) + A_{10} e^{-jk_{y10} y_1}\cos\left(\pi x_1/a\right) \qquad (4.33)$$

4.4.2.2 MFIE at BS2

Similarly for BS2, the integro-differential equation (4.27) is written in the form

$$\left(\frac{\partial^2}{\partial x^2} + k_0^2\right) F_2\left(\vec{r_2}\right) = A_2\left(\vec{r_2}\right) \qquad (4.34)$$

where

$$F_2\left(\vec{r_2}\right) = \int_{S_1} \frac{E_{y1}\left(\vec{r_1}'\right)}{j\omega\mu_0} G_{CV}\left(\vec{r_2}|\vec{r_1}'\right) dS_1'$$
$$- \int_{S_2} \frac{E_{y2}\left(\vec{r_2}'\right)}{j\omega} G_{CP}\left(\vec{r_2}|\vec{r_2}'\right) dS_2' \qquad (4.35)$$

is in the form of the MT Hertzian potential and

$$A_2\left(\vec{r_2}\right) = \bar{k}^2 \int_{S_2} \frac{E_{y2}\left(\vec{r_2}'\right)}{j\omega\mu} G_{PP}\left(\vec{r_2}|\vec{r_2}'\right) dS_2' \qquad (4.36)$$

is the forcing term that was generated by added and subtracted k_0^2 to equation (4.26)

The solution to equation (4.34) is written as

$$F_2\left(\vec{r_2}\right) = F_2^C\left(\vec{r_2}\right) + F_2^P\left(\vec{r_2}\right) \qquad (4.37)$$

where the complementary solution is given as

$$F_2^C\left(\vec{r_2}\right) = C_2\left(y_2, 0\right)\cos\left(k_0 x_2\right) + D_2\left(y_2, 0\right)\sin\left(k_0 x_2\right) \qquad (4.38)$$

and the particular solution, in terms of the forced response in (2.32) and the forcing term in (4.36) is

$$F_2^P(\vec{r_2}) = \frac{\bar{k}^2}{k_0}\int_{S_2} dS_2' \frac{E_{y2}(\vec{r_2}')}{j\omega\mu} \int_{-\infty}^{\infty}\int_{-\infty}^{\infty} d^2\lambda \frac{e^{-j\xi x_2'} e^{j\eta(y_2 - y_2')} \cosh(pd)}{(2\pi)^2 p \sinh(pd)} \cdot \int_0^{x_2} d\overline{x_2} \sin[k_0(x_2 - \overline{x_2})] e^{j\xi\overline{x_2}} \tag{4.39}$$

Solving the forced response integral, and performing some algebraic manipulation, gives the following form of the particular solution

$$F_2^P(\vec{r_2}) = \frac{\bar{k}^2}{k_0}\int_{S_2} dS_2' \frac{E_{y2}(\vec{r_2}')}{j\omega\mu} \int_{-\infty}^{\infty}\int_{-\infty}^{\infty} d^2\lambda \frac{e^{-j\xi x_2'} e^{j\eta(y_2 - y_2')} \cosh(pd)}{(2\pi)^2 p \sinh(pd)} \cdot \left[\frac{j\xi\sin(k_0 x_2) + k_0\cos(k_0 x_2) - k_0 e^{j\xi x_2}}{\xi^2 - k_0^2}\right] \tag{4.40}$$

Substituting equations (4.35), (4.38) and (4.40) into equation (4.37) and combining the complementary solutions as well as the similar integrands over S_2, leads to the MFIE at BS2

$$\int_{S_1} \frac{E_{y1}(\vec{r_1}')}{j\omega\mu_0} G_{CV}(\vec{r_2}|\vec{r_1}')\, dS_1' - \int_{S_2} \frac{E_{y2}(\vec{r_2}')}{j\omega} G_{CP2}(\vec{r_2}|\vec{r_2}')\, dS_2' = \tilde{C}_2(y_2, 0)\cos(k_0 x_2) + \tilde{D}_2(y_2, 0)\sin(k_0 x_2) \tag{4.41}$$

where

$$G_{CP2}(\vec{r_2}|\vec{r_2}') = \frac{G_{CV}(\vec{r_2}|\vec{r_2}')}{\mu_0} + \frac{G_{PPN}(\vec{r_2}|\vec{r_2}')}{\mu} \tag{4.42}$$

and the new parallel-plate Green's function is given as

$$G_{PPN}\left(\vec{r_2}|\vec{r_2}'\right) = \int_{-\infty}^{\infty}\int_{-\infty}^{\infty} d^2\lambda \frac{e^{j\vec{\lambda}\cdot\left(\vec{\rho_2}-\vec{\rho_2}'\right)}\cosh\left(pd\right)\left(\xi^2-k^2\right)}{\left(2\pi\right)^2 p\sinh\left(pd\right)\left(\xi^2-k_0^2\right)} \tag{4.43}$$

4.5 MoM Technique

In this section, a MoM technique is applied to solve the MFIEs developed in the last section. The steps taken to apply the the MoM technique along with a summary of the solution is discussed herein.

4.5.1 Expansion of Unknown Slot Voltages

The expansion of the slot electric-field in terms of the unknown slot voltages mirrors Chapter 2 (reference Section 2.5.1).

4.5.1.1 Expanded MFIE at BS1

Applying the slot electric-field expansion in equation (2.48) to equation (4.33) leads to the expanded version of the MFIE at BS1

$$\begin{aligned}\int_{-L_1}^{L_1} dx_1' V_1\left(x_1'\right) K_{WC}\left(x_1, y_1|x_1'\right) - \int_{-L_2}^{L_2} dx_2' V_2\left(x_2'\right) K_{CV2}\left(x_1, y_1|x_2'\right) \\ = \tilde{C}_1\left(y_1\right)\cos\left(k_0x_1\right) + D_1\left(y_1\right)\sin\left(k_0x_1\right) + A_{10}e^{-jk_{y10}y_1}\cos\left(\pi x_1/a\right)\end{aligned} \tag{4.44}$$

where the kernels at BS1 are defined as

$$K_{WC}\left(x_1, y_1|x_1'\right) = \int_{-W_1}^{W_1} dy_1' \frac{f_1\left(y_1'\right)}{j\omega\mu_0} G_{WC}\left(\vec{r_1}|\vec{r_1}'\right) \tag{4.45}$$

and

$$K_{CV2}\left(x_1, y_1|x_2'\right) = \int_{-W_2}^{W_2} dy_2' \frac{f_2\left(y_2'\right)}{j\omega\mu_0} G_{CV}\left(\vec{r_1}|\vec{r_2}'\right) \tag{4.46}$$

4.5.1.2 Expanded MFIE at BS2

Similarly, substituting the same slot electric-field expansion from equation (2.48) into equation (4.41) leads to the expanded version of the MFIE at BS2

$$\int_{-L_1}^{L_1} dx_1' V_1(x_1') K_{CV2}(x_2, y_2|x_1') - \int_{-L_2}^{L_2} dx_2' V_2(x_2') K_{CP2}(x_2, y_2|x_2')$$
$$= \tilde{C}_2(y_2, 0) \cos(k_0 x_2) + \tilde{D}_2(y_2, 0) \sin(k_0 x_2) \qquad (4.47)$$

where the kernels at BS2 are defined as

$$K_{CV2}(x_2, y_2|x_1') = \int_{-W_1}^{W_1} dy_1' \frac{f_1(y_1')}{j\omega\mu_0} G_{CV}(\vec{r_2}|\vec{r_1}') \qquad (4.48)$$

and

$$K_{CP2}(x_2, y_2|x_2') = \int_{-W_2}^{W_2} dy_2' \frac{f_2(y_2')}{j\omega} G_{CP2}(\vec{r_2}|\vec{r_2}') \qquad (4.49)$$

4.5.2 Application of the MoM Technique

Applying the following point-matching testing operator

$$\int_{-W_l}^{W_l} \int_{-L_l}^{L_l} dx_l dy_l \delta\left(x_l - x_{l_{m_l}}\right) \delta(y_l) \quad for \quad m_l = 1, 2, ..., N_l \qquad (4.50)$$

($l = 1, 2$ depending on which interface the testing is taking place at) to equations (4.44) and (4.47) respectively, leads to

$$\int_{-L_1}^{L_1} dx_1' V_1\left(x_1'\right) K_{WC}\left(x_{1m_1}, 0|x_1'\right) - \int_{-L_2}^{L_2} dx_2' V_2\left(x_2'\right) K_{CV2}\left(x_{1m_1}, 0|x_2'\right)$$
$$= \tilde{C}_1(0)\cos\left(k_0 x_{1m_1}\right) + D_1(0)\sin\left(k_0 x_{1m_1}\right) + A_{10}\cos\left(\pi x_{1m_1}/a\right)$$
$$for \quad m_1 = 1, 2, ..., N_1 \quad (4.51)$$

for BS1 and

$$\int_{-L_1}^{L_1} dx_1' V_1\left(x_1'\right) K_{CV2}\left(x_{2m_2}, 0|x_1'\right) - \int_{-L_2}^{L_2} dx_2' V_2\left(x_2'\right) K_{CP2}\left(x_{2m_2}, 0|x_2'\right)$$
$$= \tilde{C}_2(0,0)\cos\left(k_0 x_{2m_2}\right) + \tilde{D}_2(0,0)\sin\left(k_0 x_{2m_2}\right)$$
$$for \quad m_2 = 1, 2, ..., N_2 \quad (4.52)$$

for BS2. These equations are then expanded in terms of the unknown slot voltages, using the pulse-function expansion given as

$$V_l\left(x_l\right) = \sum_{n_l=1}^{N_l} V_{ln_l} p_{ln_l}\left(x_l\right) \tag{4.53}$$

where the individual segment length and location are respectively

$$\Delta x_l = 2L_l/N_l \quad ; \quad x_{ln_l} = -L_l + \left(n_l - 1/2\right)\Delta x_l \tag{4.54}$$

and the pulse function is defined as

$$p_{ln_l}\left(x_l\right) = \begin{cases} 1 & \ldots \left(x_{ln_l} - \frac{\Delta x_l}{2}\right) < x_l < \left(x_{ln_l} + \frac{\Delta x_l}{2}\right) \\ 0 & \ldots \quad otherwise \end{cases} \tag{4.55}$$

Substituting the expression for the pulse-function expansion into equations (4.51) and (4.52) respectively, gives

$$\sum_{n_1=1}^{N_1} V_{1n_1} \int\limits_{x_{1n_1}-\frac{\Delta x_1}{2}}^{x_{1n_1}+\frac{\Delta x_1}{2}} dx_1' K_{WC}\left(x_{1m_1}, 0|x_1'\right)$$
$$-\sum_{n_2=1}^{N_2} V_{2n_2} \int\limits_{x_{2n_2}-\frac{\Delta x_2}{2}}^{x_{2n_2}+\frac{\Delta x_2}{2}} dx_2' K_{CV2}\left(x_{1m_1}, 0|x_2'\right)$$
$$= \tilde{C}_1(0)\cos\left(k_0 x_{1m_1}\right) + D_1(0)\sin\left(k_0 x_{1m_1}\right) + A_{10}\cos\left(\pi x_{1m_1}/a\right)$$
$$for \quad m_1 = 1, 2, ..., N_1 \qquad (4.56)$$

for BS1 and

$$\sum_{n_1=1}^{N_1} V_{1n_1} \int\limits_{x_{1n_1}-\frac{\Delta x_1}{2}}^{x_{1n_1}+\frac{\Delta x_1}{2}} dx_1' K_{CV2}\left(x_{2m_2}, 0|x_1'\right)$$
$$-\sum_{n_2=1}^{N_2} V_{2n_2} \int\limits_{x_{2n_2}-\frac{\Delta x_2}{2}}^{x_{2n_2}+\frac{\Delta x_2}{2}} dx_2' K_{CP2}\left(x_{2m_2}, 0|x_2'\right)$$
$$= \tilde{C}_2(0,0)\cos\left(k_0 x_{2m_2}\right) + \tilde{D}_2(0,0)\sin\left(k_0 x_{2m_2}\right)$$
$$for \quad m_2 = 1, 2, ..., N_2 \qquad (4.57)$$

for BS2. These equations represent the MoM solution, for the unknown slot voltages (V_1, V_2), to the MFIEs of section 4.4. However, four constants (C_1, D_1, C_2, D_2) still remain unsolved. These constants are evaluated by invoking the appropriate boundary conditions

$$V_{l_{1,N_l}} = 0 \quad for \quad l = 1,2 \tag{4.58}$$

to equations (4.56) and (4.57), which leads to the final expressions for the MoM solution

$$\sum_{n_1=2}^{N_1-1} V_{1n_1} \int_{x_{1n_1}-\frac{\Delta x_1}{2}}^{x_{1n_1}+\frac{\Delta x_1}{2}} dx_1' K_{WC}\left(x_{1m_1}, 0|x_1'\right)$$
$$- \sum_{n_2=2}^{N_2-1} V_{2n_2} \int_{x_{2n_2}-\frac{\Delta x_2}{2}}^{x_{2n_2}+\frac{\Delta x_2}{2}} dx_2' K_{CV2}\left(x_{1m_1}, 0|x_2'\right)$$
$$= \tilde{C}_1(0)\cos\left(k_0 x_{1m_1}\right) + D_1(0)\sin\left(k_0 x_{1m_1}\right) + A_{10}\cos\left(\pi x_{1m_1}/a\right)$$
$$for \quad m_1 = 1,2,...,N_1 \tag{4.59}$$

at BS1 and

$$\sum_{n_1=2}^{N_1-1} V_{1n_1} \int_{x_{1n_1}-\frac{\Delta x_1}{2}}^{x_{1n_1}+\frac{\Delta x_1}{2}} dx_1' K_{CV2}\left(x_{2m_2}, 0|x_1'\right)$$
$$- \sum_{n_2=2}^{N_2-1} V_{2n_2} \int_{x_{2n_2}-\frac{\Delta x_2}{2}}^{x_{2n_2}+\frac{\Delta x_2}{2}} dx_2' K_{CP2}\left(x_{2m_2}, 0|x_2'\right)$$
$$= \tilde{C}_2(0,0)\cos\left(k_0 x_{2m_2}\right) + \tilde{D}_2(0,0)\sin\left(k_0 x_{2m_2}\right)$$
$$for \quad m_2 = 1,2,...,N_2 \tag{4.60}$$

at BS2.

4.5.3 MoM Solution in Matrix Form

Equations (4.59) and (4.60) is summarized in matrix form as

$$\sum_{n=1}^{N} a_{m,n} C_m = b_m \quad for \quad m = 1, 2, 3, ..., N \quad where \quad N = N_1 + N_2 \tag{4.61}$$

where $N = N_1 + N_2$ and,

$$b_m = \begin{cases} A_{10} \cos\left(\pi x 1_m / a\right) & for \quad m = 1, 2, ..., N_1 \\ 0 & for \quad m = N_1 + 1, N_1 + 2, ..., N \end{cases} \tag{4.62}$$

is the forcing vector due to the incident x-directed component of the magnetic field. The unknown slot voltages and constants are defined as

$$C_m = \begin{cases} \tilde{C}_1(0, t) & for \quad m = 1 \\ V1_m & for \quad m = 2, 3, ..., N_1 - 1 \\ D_1(0, t) & for \quad m = N_1 \\ \tilde{C}_2(0, 0) & for \quad m = N_1 + 1 \\ V2_{m-N_1} & for \quad m = N_1 + 2, N_1 + 3, ..., N - 1 \\ \tilde{D}_2(0, 0) & for \quad m = N \end{cases} \tag{4.63}$$

and finally, a summary of the moment method admittance matrix elements is given by

$$a_{m,n} = \begin{cases} -\cos\left(k_0 x1_m\right) & for \begin{cases} m &= 1, 2, ..., N_1 \\ n &= 1 \end{cases} \\ -\sin\left(k_0 x1_m\right) & for \begin{cases} m &= 1, 2, ..., N_1 \\ n &= N_1 \end{cases} \\ -\cos\left(k_0 x2_{m-N_1}\right) & for \begin{cases} m &= N_1+1, N_1+2, ..., N \\ n &= N_1+1 \end{cases} \\ -\sin\left(k_0 x2_{m-N_1}\right) & for \begin{cases} m &= N_1+1, N_1+2, ..., N \\ n &= N \end{cases} \\ 0 & for \begin{cases} m &= 1, 2, ..., N_1 \\ n &= N_1+1, N \end{cases} \\ 0 & for \begin{cases} m &= N_1+1, N_1+2, ..., N \\ n &= 1, N_1 \end{cases} \\ l^{WC}_{m,n} & for \begin{cases} m &= 1, 2, ..., N_1 \\ n &= 2, 3, ..., N_1-1 \end{cases} \\ -l^{CV1}_{m,n-N_1} & for \begin{cases} m &= 1, 2, ..., N_1 \\ n &= N_1+2, N_1+3, ..., N-1 \end{cases} \\ l^{CV2}_{m-N_1,n} & for \begin{cases} m &= N_1+1, N_1+2, ..., N \\ n &= 2, 3, ..., N_1-1 \end{cases} \\ -l^{CP2}_{m-N_1,n-N_1} & for \begin{cases} m &= N_1+1, N_1+2, ..., N \\ n &= N_1+2, N_1+3, ..., N-1 \end{cases} \end{cases} \tag{4.64}$$

4.5.3.1 Matrix Element Definitions

The solutions for the various admittance matrix elements (details in Appendix C) are given here. For the first quadrant of matrix elements, the combination of the waveguide and cavity self terms at BS1 are

$$l^{WC}_{m_1,n_1} = l^{WG}_{m_1,n_1} + l^{CV11}_{m_1,n_1} \tag{4.65}$$

where

$$\begin{aligned} l^{WG}_{m_1,n_1} = \frac{-2j}{\omega\mu_0 ab W_1} \sum_{\gamma} \frac{\epsilon_\gamma}{k_{x\gamma} k^2_{y\gamma}} \sin\left[k_{x\gamma}\left(x_{1_{m_1}} - a/2\right)\right] \sin\left[k_{x\gamma}\left(x_{1_{n_1}} - a/2\right)\right] \\ \cdot \sin\left(k_{x\gamma}\Delta x_1/2\right)\left[e^{-jk_{y\gamma}W_1} - 1\right] \quad for \quad \begin{cases} \alpha = 1, 2, 3, \ldots \\ \beta = 0, 1, 2, \ldots \end{cases} \end{aligned} \tag{4.66}$$

and

$$\begin{aligned} l^{CV11}_{m_1,n_1} = \frac{j}{\omega\mu_0 L W^2} \sum_{\Gamma} \frac{\epsilon_\Gamma}{k_{x\gamma} k_{y\Gamma} k_{z\Gamma}} \sin\left(k_{x\gamma}\Delta x_1/2\right) \\ \cdot \sin\left[k_{x\Gamma}\left(x_{1_{m_1}} - L\right)\right] \sin\left[k_{x\Gamma}\left(x_{1_{n_1}} - L\right)\right] \\ \cdot \cos^2\left(k_{y\Gamma}W\right) \sin\left(k_{y\Gamma}W\right) \cot\left(k_{z\Gamma}t\right) \end{aligned} \tag{4.67}$$

For the second quadrant of the matrix elements, the coupled cavity terms at BS1 are

$$\begin{aligned} l^{C1}_{m_1,n_2} = l^{CV12}_{m_1,n_2} = \frac{j}{\omega\mu_0 L W W_2} \sum_{\Gamma} \frac{\epsilon_\Gamma}{k_{x\gamma} k_{y\Gamma} k_{z\Gamma} \sin\left(k_{z\Gamma}t\right)} \\ \cdot \sin\left(k_{x\gamma}\Delta x_2/2\right) \sin\left[k_{x\Gamma}\left(x_{1_{m_1}} - L\right)\right] \sin\left[k_{x\Gamma}\left(x_{2_{n_2}} - L\right)\right] \\ \cdot \cos^2\left(k_{y\Gamma}W\right) \sin\left(k_{y\Gamma}W_2\right) \end{aligned} \tag{4.68}$$

For the third quadrant of the matrix elements, the coupled cavity terms at BS2 are

$$l_{m_2,n_1}^{C2} = l_{m_2,n_1}^{CV21} = \frac{j}{\omega\mu_0 L W^2} \sum_{\Gamma} \frac{\epsilon_\Gamma}{k_{x_\gamma} k_{y_\Gamma} k_{z_\Gamma} \sin\left(k_{z_\Gamma} t\right)}$$
$$\cdot \sin\left(k_{x_\gamma} \Delta x_1/2\right) \sin\left[k_{x_\Gamma}\left(x_{2_{m_2}} - L\right)\right] \sin\left[k_{x_\Gamma}\left(x_{1_{n_1}} - L\right)\right]$$
$$\cdot \cos^2\left(k_{y_\Gamma} W\right) \sin\left(k_{y_\Gamma} W\right) \qquad (4.69)$$

Finally, for the fourth quadrant of matrix elements, the combination of the cavity and parallel-plate self terms at BS2 are

$$l_{m_2,n_2}^{CH} = l_{m_2,n_2}^{CV22} + l_{m_2,n_2}^{PP} \qquad (4.70)$$

where

$$l_{m_2,n_2}^{CV22} = \frac{j}{\omega\mu_0 L W W_2} \sum_{\Gamma} \frac{\epsilon_\Gamma \cos\left(k_{z_\Gamma} t\right)}{k_{x_\gamma} k_{y_\Gamma} k_{z_\Gamma} \sin\left(k_{z_\Gamma} t\right)}$$
$$\cdot \sin\left(k_{x_\gamma} \Delta x_2/2\right) \sin\left[k_{x_\Gamma}\left(x_{2_{m_2}} - L\right)\right] \sin\left[k_{x_\Gamma}\left(x_{2_{n_2}} - L\right)\right]$$
$$\cdot \cos^2\left(k_{y_\Gamma} W\right) \sin\left(k_{y_\Gamma} W_2\right) \qquad (4.71)$$

and

$$l_{m_2,n_2}^{PP} = l_{m_2,n_2}^{PP1} + l_{m_2,n_2}^{PP2} + l_{m_2,n_2}^{PP3} \qquad (4.72)$$

The three components of the parallel-plate self terms at BS2 are

$$l_{m_2,n_2}^{PP1} = \frac{-j}{\omega\mu 4 W_2} \left[\sum_{\upsilon=1}^{\infty} \frac{2 p_{0_\upsilon}^2 F_1^{exp1}}{\xi_\upsilon^2 \left(\xi_\upsilon^2 - k_0^2\right) d} + \frac{\overline{k} \cos\left(\overline{k} d\right) F_1^{exp2}}{k_0^2 \sin\left(\overline{k} d\right)}\right] \qquad (4.73)$$

and

$$l_{m_2,n_2}^{PP2} = \frac{j k \cos\left(k d\right)}{\omega\mu 2 W_2 k_0^2 \sin\left(k d\right)} \quad for \quad m = n \qquad (4.74)$$

and

$$l^{PP3}_{m_2,n_2} = \frac{-j}{\omega\mu\pi W_2 d} \sum_{\nu=0}^{\infty} \epsilon_\nu$$

$$\cdot \int_0^{\infty} d\xi \frac{\cos\left[\xi\left(x_{2_{m_2}} - x_{2_{n_2}}\right)\right] \sin\left(\xi \Delta x_2/2\right)\left(\xi^2 - k^2\right) e^{-j\eta_\nu W_2}}{\xi\left(\xi^2 - k_0^2\right)\eta_\nu^2} \tag{4.75}$$

Other definitions include

$$F_1^{exp1} = \begin{cases} \left[e^{-j\xi_v A} - e^{-j\xi_v B}\right] & for \quad m > n \\ \left[e^{-j\xi_v A} + e^{j\xi_v B}\right] & for \quad m = n \\ \left[-e^{j\xi_v A} + e^{j\xi_v B}\right] & for \quad m < n \end{cases} \tag{4.76}$$

and

$$F_1^{exp2} = \begin{cases} \left[e^{-jk_0 A} - e^{-jk_0 B}\right] & for \quad m > n \\ \left[e^{-jk_0 A} + e^{jk_0 B}\right] & for \quad m = n \\ \left[-e^{jk_0 A} + e^{jk_0 B}\right] & for \quad m < n \end{cases} \tag{4.77}$$

where the terms A, B are given as

$$\begin{aligned} A &= \Delta x\left(m - n + 1/2\right) \\ B &= \Delta x\left(m - n - 1/2\right) \end{aligned} \tag{4.78}$$

and the various spectral constants are

$$\xi_v^2 = p_{0_v}^2 + k^2 \quad ; \quad p_{0_v} = \frac{jv\pi}{d} \quad ; \quad \xi_v = -j\sqrt{-\left(\xi_v^2\right)} \tag{4.79}$$

$$\eta_\nu^2 = p_\nu^2 + k^2 - \xi^2 \quad ; \quad p_\nu = \frac{j\nu\pi}{d} \quad ; \quad \eta_\nu = -j\sqrt{-\left(\eta_\nu^2\right)} \tag{4.80}$$

$$\bar{k}^2 = k^2 - k_0^2 \quad ; \quad \bar{k} = \sqrt{k^2 - k_0^2} \tag{4.81}$$

with the Neumann number for the residues given as

$$\epsilon_\nu = \begin{cases} 1 & for \quad \nu = 0 \\ 2 & for \quad \nu \neq 0 \end{cases} \tag{4.82}$$

4.6 Rectangular Waveguide Scattering Parameters

The objective of this section is to obtain expressions for the rectangular waveguide scattering parameters S_{11}^{thy} and S_{21}^{thy}. This is accomplished by comparing the ratio of scattered to incident electric field intensities at specific interfaces in the rectangular waveguide [58]. The effect of certain slot dimensions, parallel-plate dimensions and EM materials are discussed utilizing the formulation.

4.6.1 Reflection and Transmission Coefficients

The rectangular waveguide scattering parameters S_{11}^{thy} and S_{21}^{thy} were developed in Section 2.6, and are repeated here for convenience. The scattering parameters are given in terms of the reflection and transmission coefficients as

$$\Gamma = S_{11}^{thy} \quad ; \quad T = S_{21}^{thy} \tag{4.83}$$

The reflection coefficient is given as

$$\Gamma(x, y) = e^{jk_{y10} 2y_I} \Gamma(x) \tag{4.84}$$

where the x-dependence with N_1 as the number of slot partitions at BS1 is

$$\Gamma(x) = -\frac{\Delta x_1 \sin\left(k_{y_{10}} W_1\right)}{W_1 ab\omega\mu_0 k_{y_{10}}^2} \sum_{n_1=1}^{N_1} V_1\left(x_{1_{n_1}}\right) \cos\left(k_{x_{10}} x_{1_{n_1}}\right) \tag{4.85}$$

and the transmission coefficient is

$$T(x, y) = e^{-jk_{y10}(y_T - y_I)} \left[1 - \Gamma(x)\right] \tag{4.86}$$

4.6.2 Analysis of Material Properities

The purpose of this section is to analyze how certain material properties (permittivity, permeability and material thickness) affect the rectangular waveguide scattering parameters. Only the magnitude data is considered since the phase data, which essentially represents only a phase shift in the waveguide, adds only consistent information.

4.6.2.1 Relative Permittivity and Permeability

The permittivity and permeability are the parameters of most interest, since they are the ultimately the desired result from the extraction process in the next Chapter. Therefore, an understanding of how each specific component of the complex variables affects the waveguide scattering parameters is of significant importance. For this analysis the slot dimensions are kept the same as those in Chapter 2, a material thickness of 5 mm is used, and the material parameters not under analysis are those of free-space.

Figure 4.2 shows the magnitude, in dB, of the reflection and transmission coefficients for various real components of relative permittivity versus a frequency range of 8.2 - 12.4 GHz. As the real component of the relative permittivity increases, the resonance is seen to shift lower in frequency and the strength of signal coupled to the material is seen to decrease.

Figure 4.3 shows the magnitude, in dB, of the reflection and transmission coefficients for various imaginary components of relative permittivity versus a frequency range of 8.2 - 12.4 GHz. As the imaginary component of the relative permittivity is increased, the resonance of the signal is seen to shift higher in frequency and the strength of signal coupled to the material decreases.

Figure 4.4 shows the magnitude, in dB, of the reflection and transmission coefficients for various real components of relative permeability versus a frequency range of 8.2 - 12.4 GHz. As the real component of relative permeability increases, the resonance is seen to shift lower in frequency, but not as quickly as with the real component of relative permittivity. Also, there is no decrease in strength of signal coupled to the material.

Figure 4.5 shows the magnitude, in dB, of the reflection and transmission coefficients for various imaginary components of relative permeability versus a frequency range of 8.2 - 12.4 GHz. As the imaginary component of relative permeability increases, the resonance is seen to shift lower in frequency and a general trend of the strength of signal coupled to the material decreasing holds till the last value. At which point the strength of signal is seen to jump back up to a higher value. This might be due to the material thickness and the possibility of a higher order mode propagation.

4.6.2.2 Material Thickness

The last material parameter of interest for analysis is the thickness of the material. As the material thickness changes, the distance the signal travels before it reflects off the PEC boundary is changed. This leads to higher order modes being excited in the parallel-plate region if the thickness is greater than half a wavelength in the material. For this analysis the slot dimensions are kept the same as those in Chapter 2.

Figure 4.6 shows the magnitude, in dB, of the reflection and transmission coefficients for various thicknesses of a loaded material (ep = 2 - j1.d-3, mu = 1 - j1.d-3) versus a frequency range of 8.2 - 12.4 GHz. As the thickness of the loaded material increases, the resonance shifts lower in frequency and the strength of signal coupled to the material increases as the material nears a half wavelength (12 mm). When the thickness increases above a half wavelength the resonance then shifts higher in frequency and the strength of signal coupled to the material decreases. The effect of higher order modes beginning to propagate is seen on the thicknesses above a half wavelength.

Figure 4.7 shows the magnitude, in dB, of the reflection and transmission coefficients for various thicknesses of a loaded material (ep = 2 - j1.d0, mu = 1 - j1.d-3) versus a frequency range of 8.2 - 12.4 GHz. As the thickness of the loaded material increases, the resonance shifts lower in frequency and the signal coupled to the material is seen to decrease. As the imaginary component of relative permittivity is increased, the signal is attenuated faster and thus does not affect the results as significantly.

Figure 4.8 shows the magnitude, in dB, of the reflection and transmission coefficients for various thicknesses of a loaded material (ep = 1 - j1.d-3, mu = 2 - j1.d-3) versus a frequency range of 8.2 - 12.4 GHz. Figure 4.9 shows the magnitude, in dB, of the reflection and transmission coefficients for various thicknesses of a loaded material (ep = 1 - j1.d-3, mu = 2 - j1.d0) versus a frequency range of 8.2 - 12.4 GHz. As the thickness increases for the magnetically loaded materials increases, similar properties to the electrically loaded materials with a slightly tighter dispersion of the resonance curves for the magnetically loaded cases.

4.6.3 Analysis of Slot Dimensions

The purpose of this section is to analyze how certain slot dimensions (thickness, length and width) affect the rectangular waveguide scattering parameters. This analysis is performed with the material properties mirroring those of FGM125, the available sample for validation in the next Chapter. Only the magnitude data is considered since the phase data, which essentially represents only a phase shift in the waveguide, adds only consistent information for the analysis.

4.6.3.1 Thickness of Slot

Figure 4.10 shows the magnitude, in dB, of the reflection and transmission coefficients for various slot wall thicknesses versus a frequency range of 8.2 - 12.4 GHz. As the thickness of the slot increases the resonance is seen to shift slightly higher in frequency and have a slightly larger coupling. However, at non-resonant frequencies the coupling is seen to drastically decrease as the thickness increases.

4.6.3.2 Length of Slot

Figure 4.11 shows the magnitude, in dB, of the reflection and transmission coefficients for various slot lengths versus a frequency range of 8.2 - 12.4 GHz. As the length of the slot increases, the resonance is seen to shift lower in frequency. This matches the results of Chapter 2, except that a smaller slot length is needed to match the resonant length of the wavelength in the material.

4.6.3.3 Width of Slot

Figure 4.12 shows the magnitude, in dB, of the reflection and transmission coefficients for various slot widths versus a frequency range of 8.2 - 12.4 GHz. As the width of the slot increases, the coupling to the material is seen to increase. The most significant change is seen at non-resonant frequencies, although at the largest width the resonant frequencies are also seen to have increased coupling.

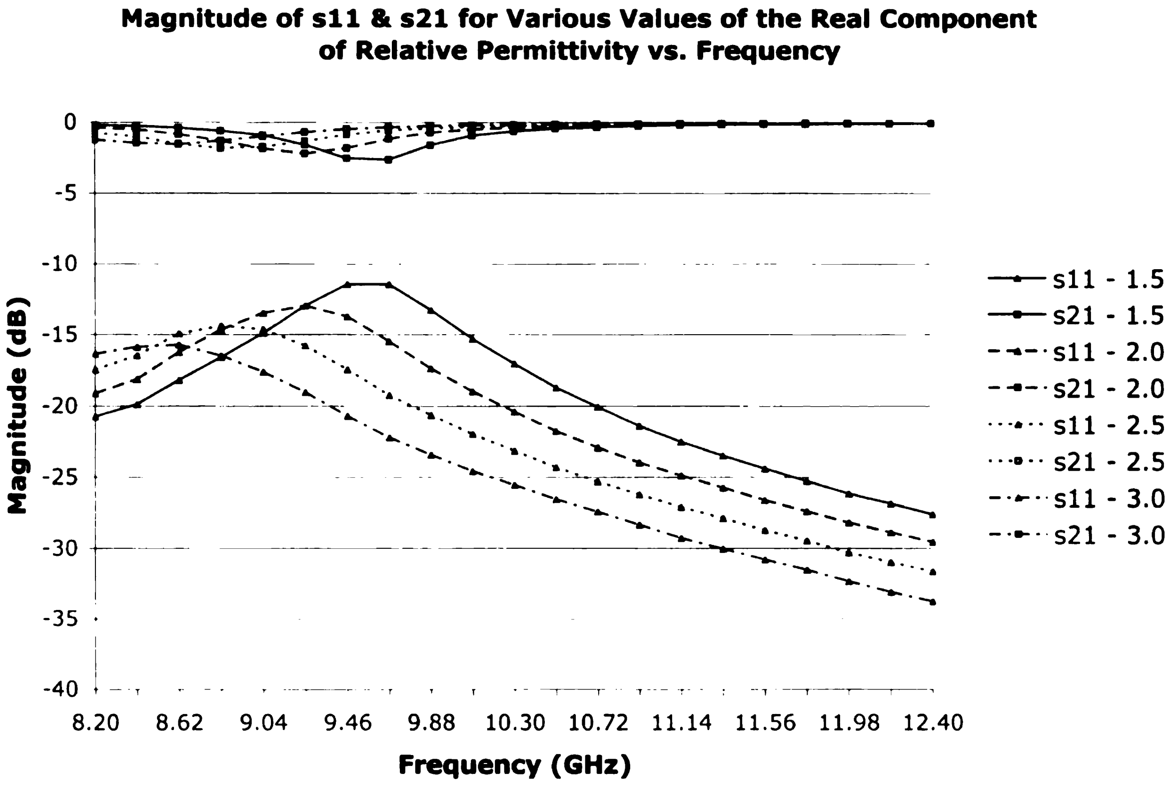

Figure 4.2. Effect of the real component of the relative permittivity on the magnitude (dB) of the waveguide scattering parameters vs. frequency (GHz).

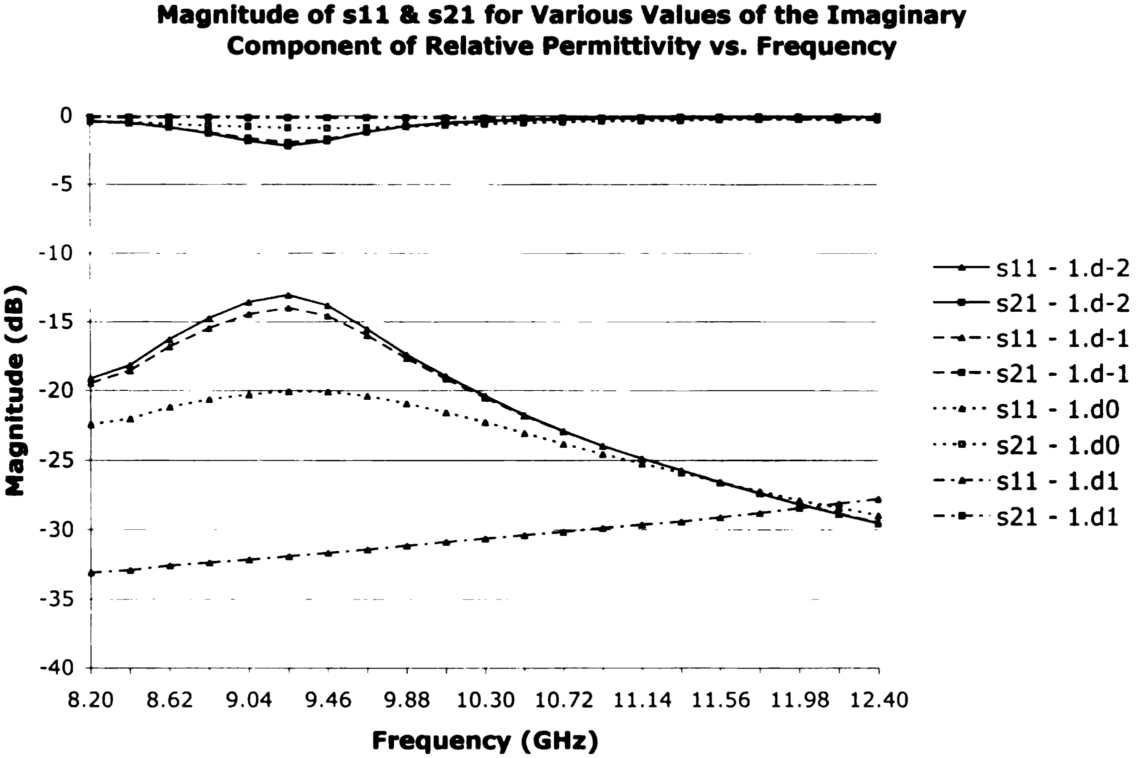

Figure 4.3. Effect of the imaginary component of the relative permittivity on the magnitude (dB) of the waveguide scattering parameters vs. frequency (GHz).

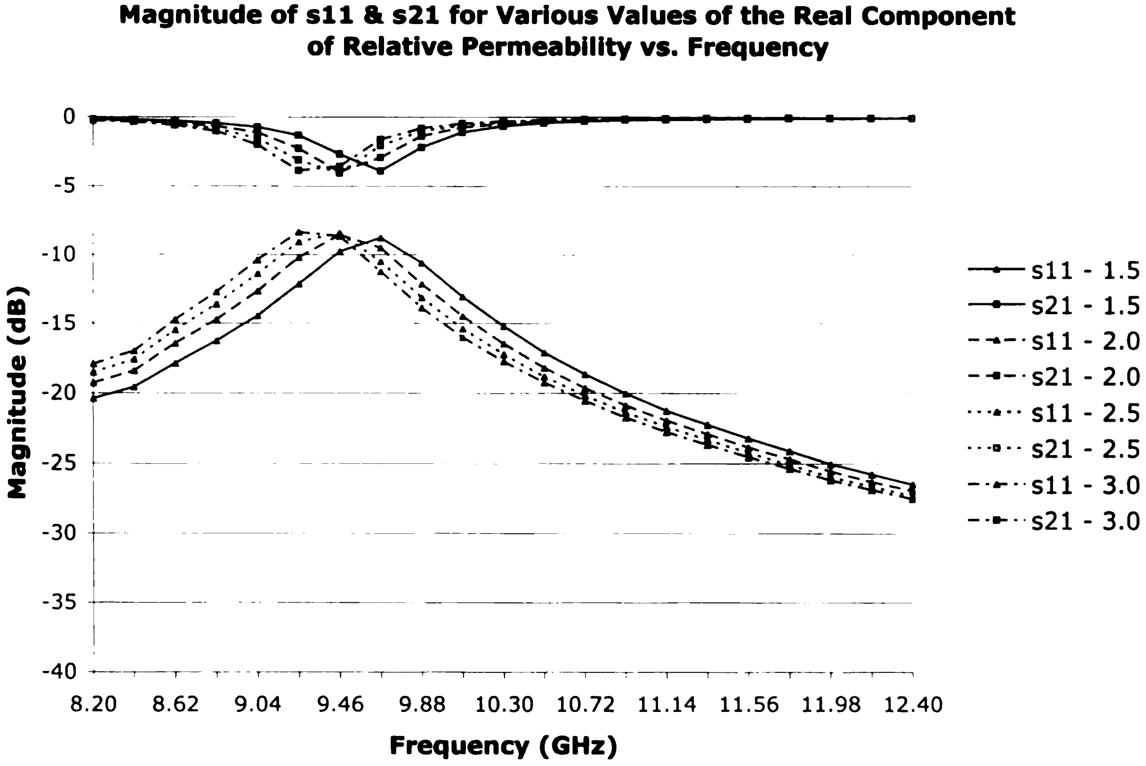

Figure 4.4. Effect of the real component of the relative permeability on the magnitude (dB) of the waveguide scattering parameters vs. frequency (GHz).

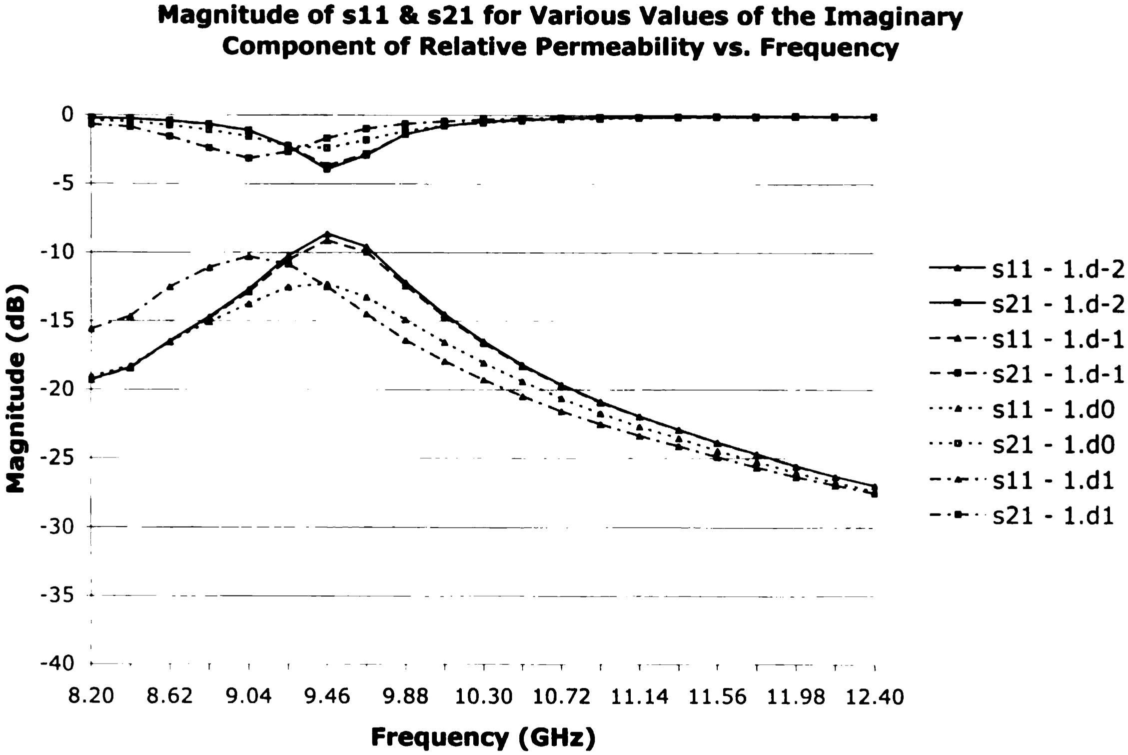

Figure 4.5. Effect of the imaginary component of the relative permeability on the magnitude (dB) of the waveguide scattering parameters vs. frequency (GHz).

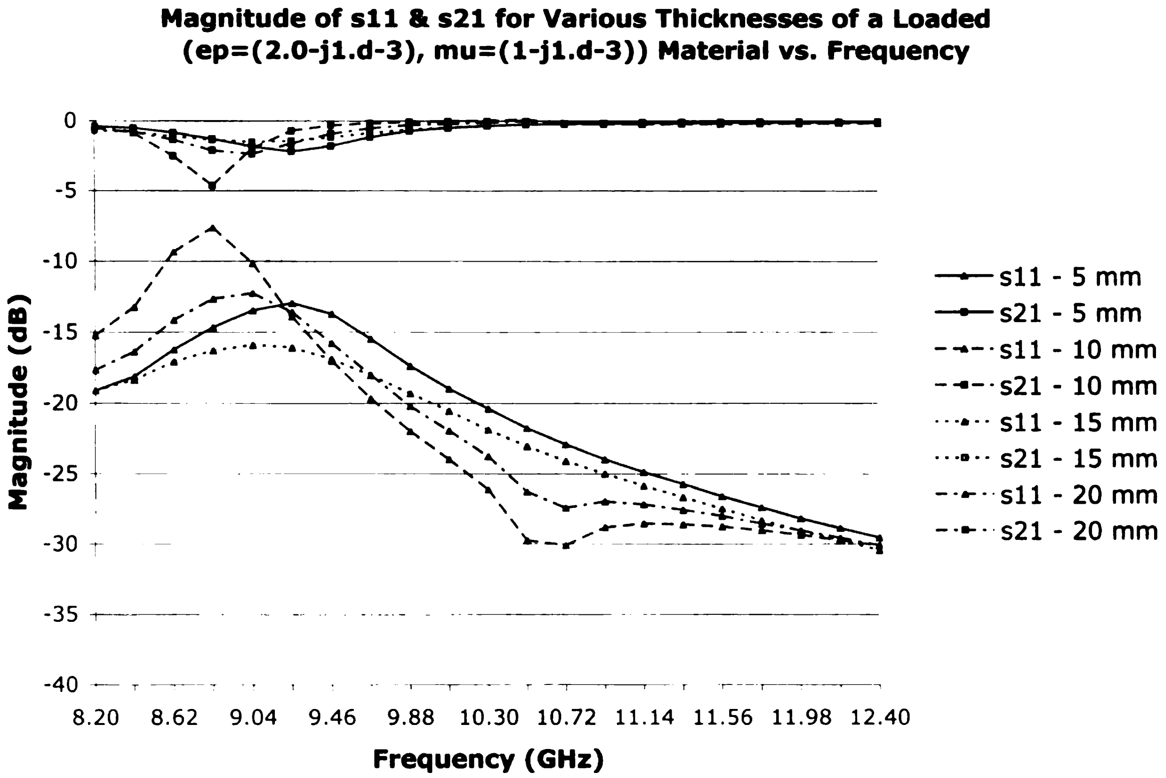

Figure 4.6. Effect of the material thickness of the real component of the relative permittivity on the magnitude (dB) of the waveguide scattering parameters vs. frequency (GHz).

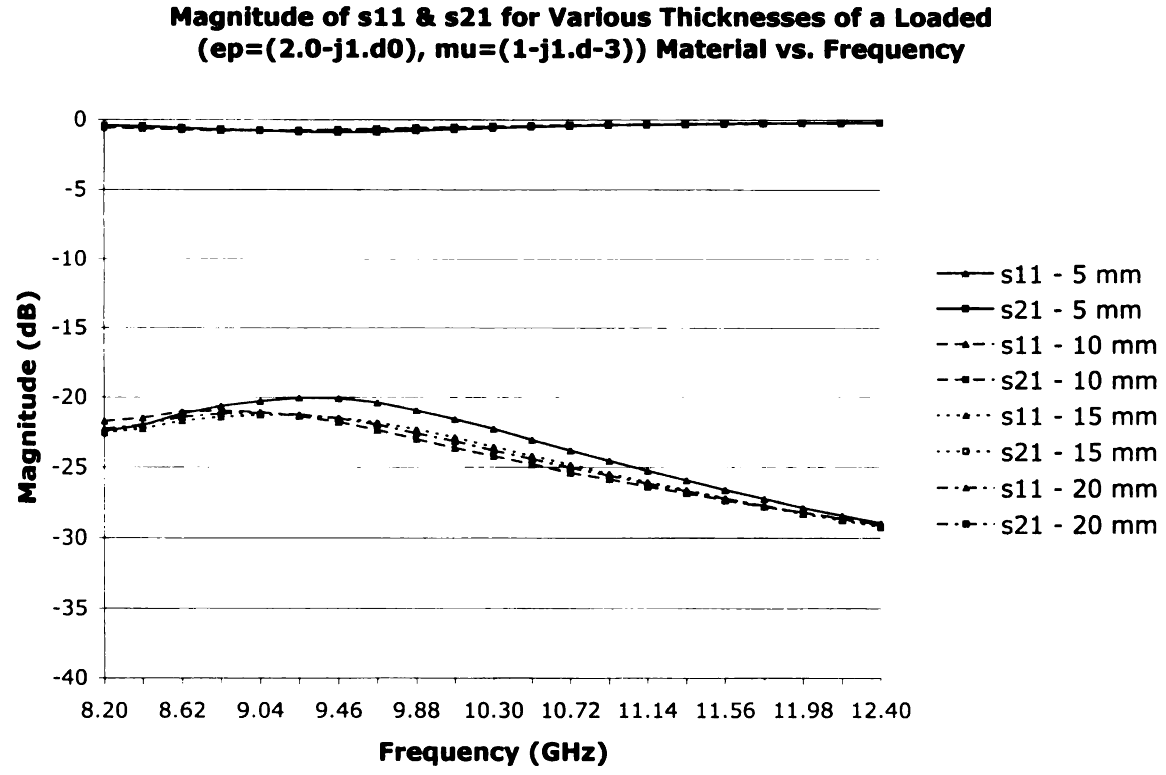

Figure 4.7. Effect of the material thickness of the imaginary component of the relative permittivity on the magnitude (dB) of the waveguide scattering parameters vs. frequency (GHz).

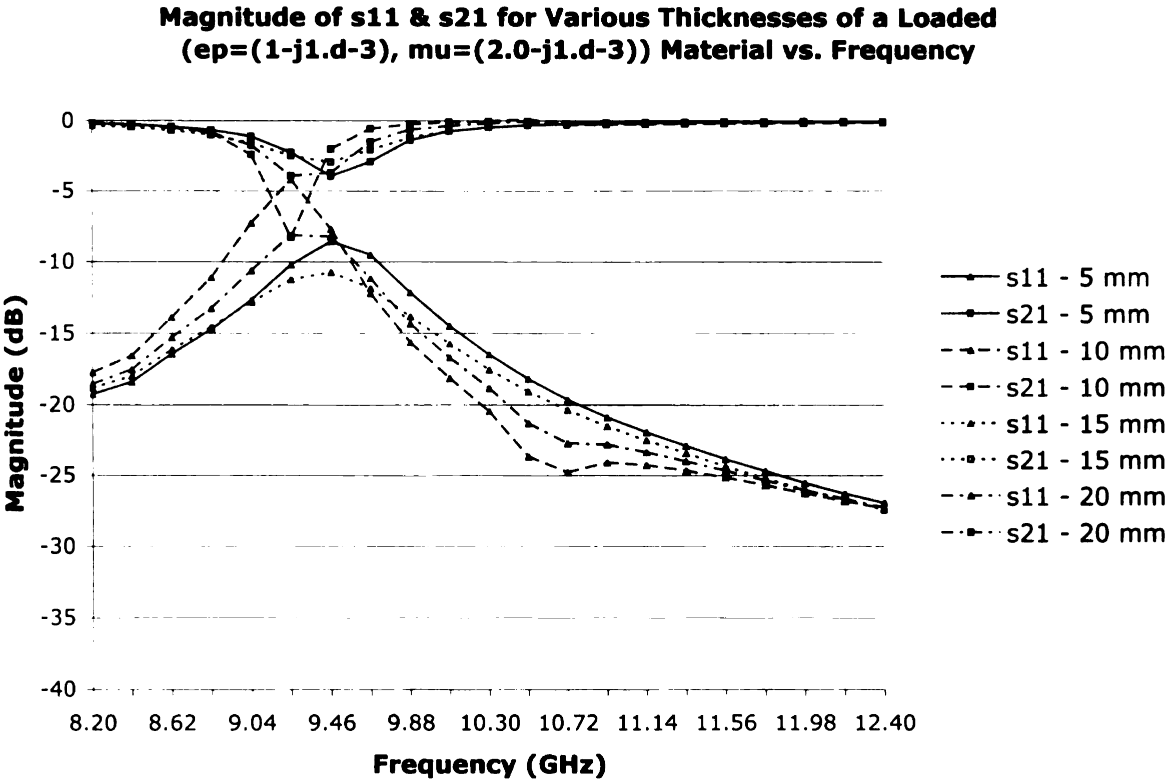

Figure 4.8. Effect of the material thickness of the real component of the relative permeability on the magnitude (dB) of the waveguide scattering parameters vs. frequency (GHz).

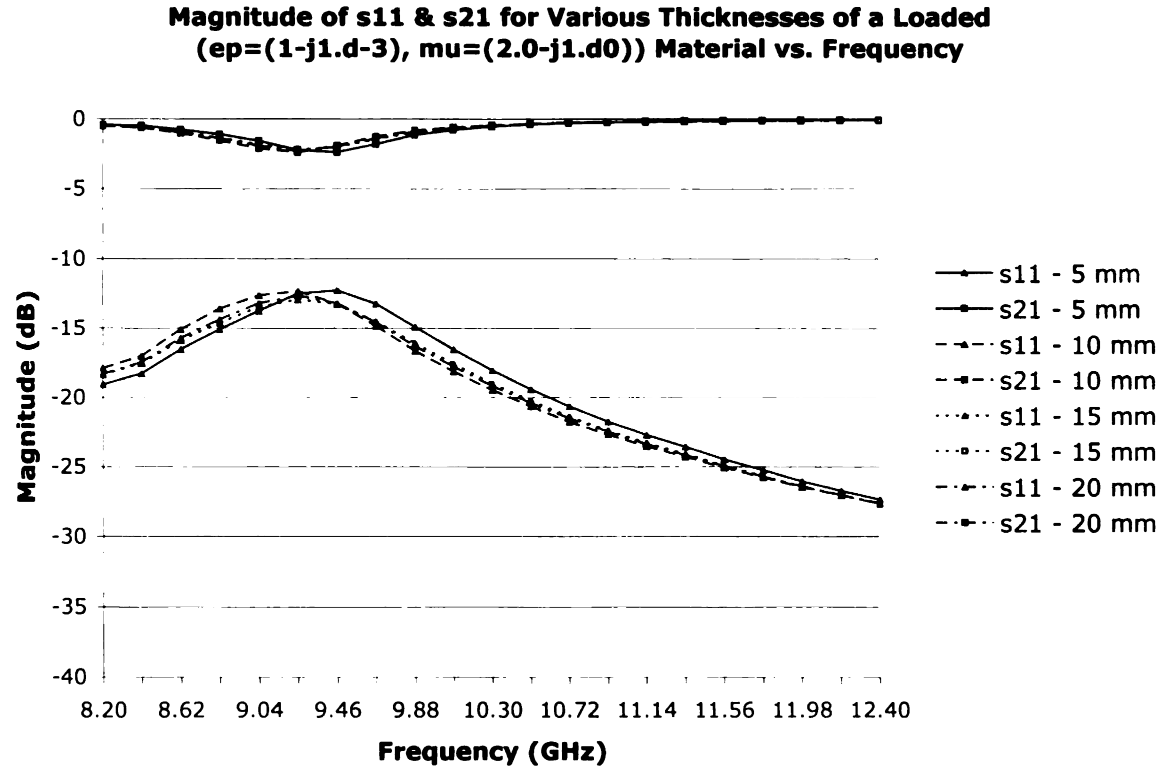

Figure 4.9. Effect of the material thickness of the imaginary component of the relative permeability on the magnitude (dB) of the waveguide scattering parameters vs. frequency (GHz).

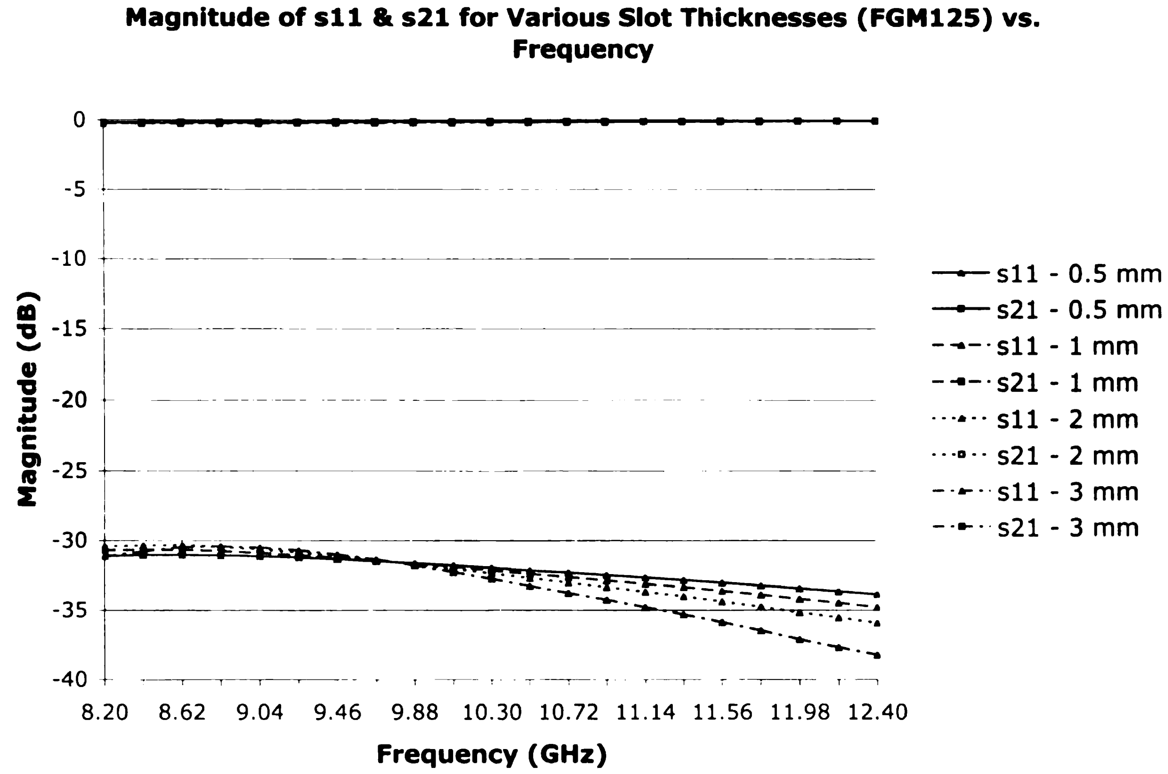

Figure 4.10. Effect of the slot wall thickness, for a parallel-plate region loaded with FGM125, on the magnitude (dB) of the waveguide scattering parameters vs. frequency (GHz).

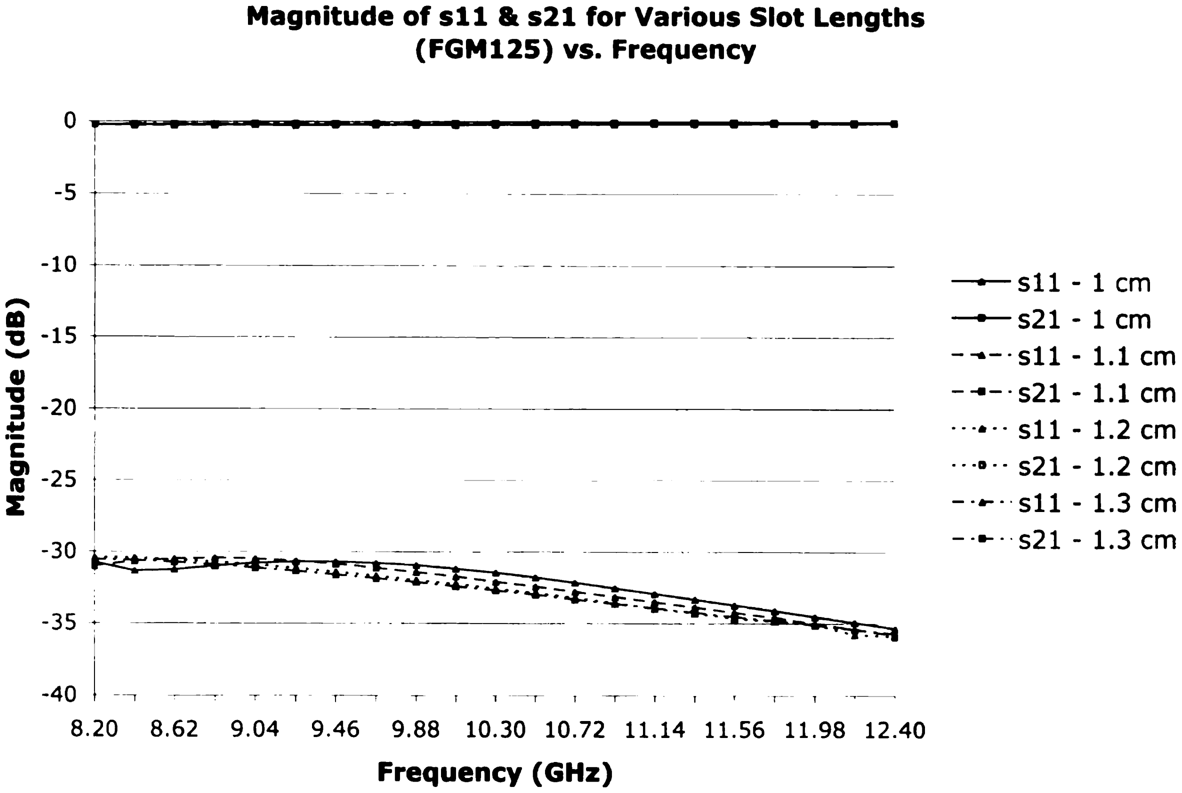

Figure 4.11. Effect of the slot length, for a parallel-plate region loaded with FGM125, on the magnitude (dB) of the waveguide scattering parameters vs. frequency (GHz).

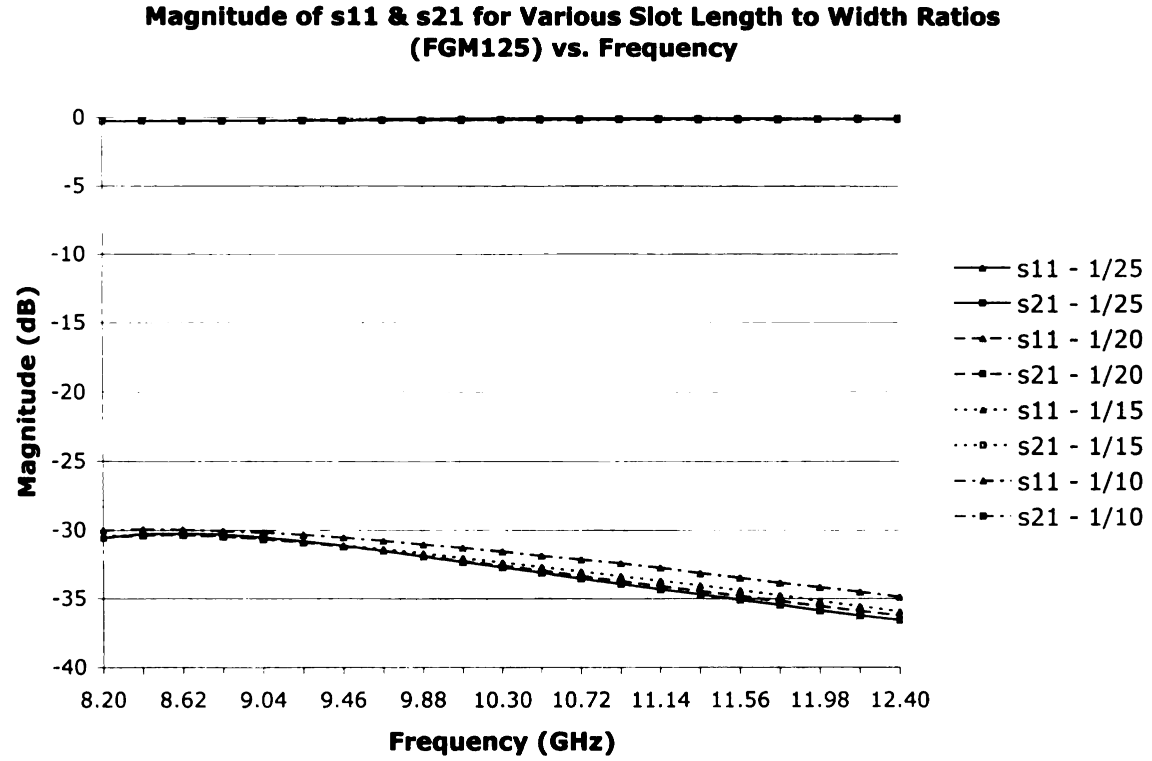

Figure 4.12. Effect of the slot width (using slot length to width ratios), for a parallel-plate region loaded with FGM125, on the magnitude (dB) of the waveguide scattering parameters vs. frequency (GHz).

CHAPTER 5

RESULTS

To verify the MFIE techniques developed in both Chapter 2 and Chapter 4, several measurements were taken in the X-band frequency range, 8.2-12.4 GHz. While this technique is valid over any desired frequency range, the dimensions and availability of X-band waveguide sections made this the easiest range for a proof of concept demonstration. In this Chapter, the experimental setup is explained and verified, the extraction process is investigated and verified, and experimental results are shown for MagRAM.

5.1 Experimental Setup

The experimental setup used for this resonant antenna material characterization technique is shown in Figure 5.1 and Figure 5.2. The physical experiment gets connected to a HP8510C Vector Network Analyzer (VNA) via coaxial cables, coax to WR90 waveguide (where the WR stands for "waveguide rectangular" and 90 refers to the inner waveguide width a = 0.90 inches) transitions, and WR90 waveguide sections. The connection between the physical experiment and the WR90 waveguide sections uses precision alignment pins and screws to help minimize the discontinuities across the interfaces. Great care is also taken to ensure that the coaxial cables are spatially stabilized while calibrating the experimental setup and measuring samples. The two-port experimental setup is calibrated using the thru-reflect-line (TRL) method [65]-[67]. The full two-port TRL calibration method, including the development of the calibration kit for the HP 8510C, is discussed in [68].

The physical experiment is built out of a single sheet of brass (Length = 5.5 inches, Width = 5 inches, and Height = 1.625 inches) to help insure that there are no electrical discontinuities, except at the flanges and the transverse slot. To build the device, the machine shop first conductively etched a WR90 waveguide segment (Length = 5.5 inches, Width = 0.9 inches, and Height = 0.4 inches) into the length of the brass sheet. Next, they milled away the excess material above the WR90 waveguide segment to achieve the thinest waveguide wall thickness (0.04 inches) that was structurally durable. Then the precision alignment pin and screw holes were drilled for the WR90 waveguide flanges. Finally, the transverse slot (Length = 0.45 inches and Width = 0.27 inches) is etched into the center of the upper WR90 waveguide wall.

5.1.1 Validation

Before measuring any test samples, a standard baseline is checked to initially validate the experimental setup. After performing the calibration, the two waveguide sections are placed together and the magnitude and phase of the S-parameters is checked to ensure that $S_{21,12}^{exp} = 1\angle 0^o$ and $\left|S_{11,22}^{exp}\right| = 0$. Next, the physical experiment, with the slot covered by conductive tape, is connected to the VNA and the magnitude and phase of the S-parameters is again checked to ensure that $S_{21,12}^{exp} \approxeq 1\angle 0^o$ and $\left|S_{11,22}^{exp}\right| \approxeq 0$. The magnitude and phase are approximate in this case due to the slot discontinuity in the waveguide wall.

5.1.1.1 Radiation into a Half-Space

To provide further confidence and validation of the experimental setup, a comparison of measured and formulated data, for radiation into a half-space, is considered. Figure 5.3 shows the comparison of formulation results and experimental data for the magnitude (in decibels (dB)) of the rectangular waveguide reflection and transmission coefficients versus a frequency range of 8.2 - 12.4 GHz. Figure 5.4 shows the comparison of formulation results and experimental data for the phase (in degrees) of the rectangular waveguide reflection and transmission coefficients versus a frequency range of 8.2 - 12.4 GHz. The curves for both the magnitude and phase of the reflection and transmission coefficients line up very well.

The resonance of the slot antenna is seen at just slightly less than 13 GHz, which is expected since the slot is the complement of a strip dipole antenna [55]. Also, the dispersion of the formulated resonance is slightly tighter than the experimental resonance. This is expected since the formulation assumes the brass waveguide is a PEC, when in actuality it has a small amount of ohmic loss.

5.1.1.2 Signal Attenuation

In observing Figure 5.2 it is noticed that the experimental setup has a finite parallel-plate region, whereas the formulation assumed and infinite parallel-plate region. The assumption of an infinite parallel-plate region was implemented for two reasons: it greatly reduces the complexity of the formulation; the motivation of this problem was the characterization of lossy EM materials. Since the signal in a lossy media attenuates, no contribution is seen from fringing fields due to the finite boundaries of the physical experiment. Thus making the assumption viable and allowing the formulation to correctly model the experiment.

To understand how lossy the EM materials must be to ensure the assumption of an infinite parallel-plate region is maintained, an analysis of the attenuation of signals in the parallel-plate region is given. Figure 5.5 and Figure 5.6 show the attenuation of a wave traveling 6 cm in a parallel-plate waveguide for various real components of relative permittivity versus the imaginary component of relative permittivity for 8.2 and 12.4 GHz respectively. The signals are seen to decay rapidly as the imaginary component increases. As the real component of permittivity increases, a higher imaginary component is required to achieve the same level of signal attenuation. There is a tighter dispersion between the curves for the real component of permittivity as the frequency increases.

The MagRAM sample that is used to validate the formulation is FGM125 from Cuming Microwave. Using its general material properties [41], a knowledge of the general attenuation properties of the signal in the MagRAM is obtained. Figure 5.7

shows the attenuation of a wave traveling in a parallel-plate waveguide loaded with FGM125 for various frequencies versus distance. The signal is seen to attenuate to -40 dB in less than 1 cm over the desired X-band bandwidth. Thus, showing that no fringing effects are seen when measuring the experimental data with the experimental setup that has been built.

5.2 Complex Constitutive Parameter Extraction

The overall objective of this material measurement technique is to experimentally obtain sample scattering parameters using a network analyzer and compare them with their theoretical expressions. That is,

$$\begin{aligned} S_{11}^{thy}(\omega,\epsilon,\mu) - S_{11}^{exp}(\omega) &= 0 \\ S_{21}^{thy}(\omega,\epsilon,\mu) - S_{21}^{exp}(\omega) &= 0 \end{aligned} \tag{5.1}$$

This pair of nonlinear equations with two unknowns has a solution which is seen to decompose into two parts. First, analytical theory is needed to relate $S_{11}^{thy}(\omega,\epsilon,\mu)$ and $S_{21}^{thy}(\omega,\epsilon,\mu)$ to the complex constitutive parameters (see MFIE analysis in Chapter 4). Second, a technique is needed to accurately measure $S_{11}^{exp}(\omega)$ and $S_{21}^{exp}(\omega)$ (see previous section). With the two necessary parts for the solution, equation 5.1 is iteratively solved using a complex two-dimensional Newton root search method, giving the desired results of the complex constitutive parameters [7].

5.2.1 Extraction Validation

The ultimate goal for this material measurement technique is to simultaneously extract both permittivity and permeability. The intention is to perform the extraction using both the reflection and transmission coefficients from the rectangular waveguide, while measuring only a single layer of the material. Unfortunately, simple validation tests of the extraction process showed that this is not possible under the current formulation. Essentially, the two scattering parameters do not provide enough sensitivity to perform the extraction.

In order to achieve the desired goal of simultaneous extraction of permittivity and permeability, a second independent experimental measurement is needed. The simplest method to achieve this goal is to measure a second thickness of the desired material. Then using one of the scattering parameters from each of the two different material thickness measurements, solve the pair of nonlinear equations in 5.1.

To decipher how different the two material thicknesses need be to perform the complex constitutive parameter extraction, tests were performed using generated acrylic data. Acrylic is used due to its consistent material properties across the entire waveguide bandwidth. Figure 5.8 shows the extracted permittivity and permeability values for an acrylic material with a material thickness difference equal to 15 percent of the material wavelength. The data is seen to be very good across most of the bandwidth, however, certain points are still not converging correctly.

Figure 5.9 shows the extracted permittivity and permeability values for an acrylic material with a material thickness difference equal to 20 percent of the material wavelength. The data is seen to be very good across the entire bandwidth, leading to the conclusion that a 20 percent material wavelength thickness difference is sufficient to properly extract the desired material characteristics.

5.2.2 Tested Samples

The general concept of this resonant antenna material characterization technique is to non-destructively measure simple, lossy medias. Thus, the ultimate verification of this technique is to measure a sample with those properties. MagRAM, in the form of FGM125 from Cuming Microwave, is a convenient solution in that it exhibits the desired properties, it is readily available, and comparison data is available using a partially-filled waveguide technique [68].

5.2.2.1 MagRAM

The results for permeability of the MagRAM using the resonant slot-antenna technique are compared to the results using a partially-filled rectangular waveguide technique in Figure 5.10. Using the results of the partially-filled rectangular waveguide technique as the baseline for the expected results for the resonant slot-antenna technique, the values of the permeability are seen to line up very well.

The results for permittivity of the MagRAM using the resonant slot-antenna technique are compared to the results using a partially-filled rectangular waveguide technique in Figure 5.11. Again, using the results of the partially-filled rectangular waveguide technique as the baseline for the expected results for the resonant slot-antenna technique, the values of the permittivity are seen to not line up very well. The real component of the permittivity seems to have the general concept, but oscillates wildly about the desired value. Whereas the imaginary component of the permittivity also oscillates wildly, but not near the desired value.

These type of results have been noticed before, mostly in coaxial probe techniques, and are due to air-gaps between the probe flange and the material surface [22],[40],[69]-[70]. Even a small air-gap between the sample and probe causes a significant discontinuity in the strong, normal electric-fields leading to large errors on the predicted permittivity values. The permeability results however remain largely unchanged as there EM boundary conditions are not significantly affected by the small discontinuity.

However, for a couple of reason the issue is believed not to be due to an air-gap. First, the real component of permittivity would be lower across the entire bandwidth than the predicted value, which is not the case. Second, the electric field is actually tangential and therefore continuous, which should not create such a large effect on results. Finally, an exceptionally heavy weight was placed on the experimental setup ensuring a good contact between the material and slot antenna. The alternative explanation offered is a poor electric field interrogation of the material.

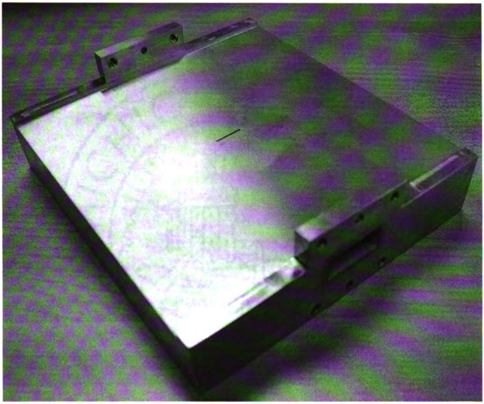

Figure 5.1. Experimental Setup: Rectangular waveguide radiating through a transverse slot into a half space.

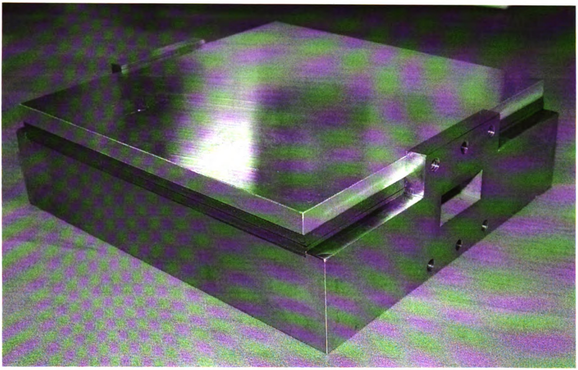

Figure 5.2. Experimental Setup: Rectangular waveguide radiating through a transverse slot into a finite parallel-plate region loaded with MagRAM.

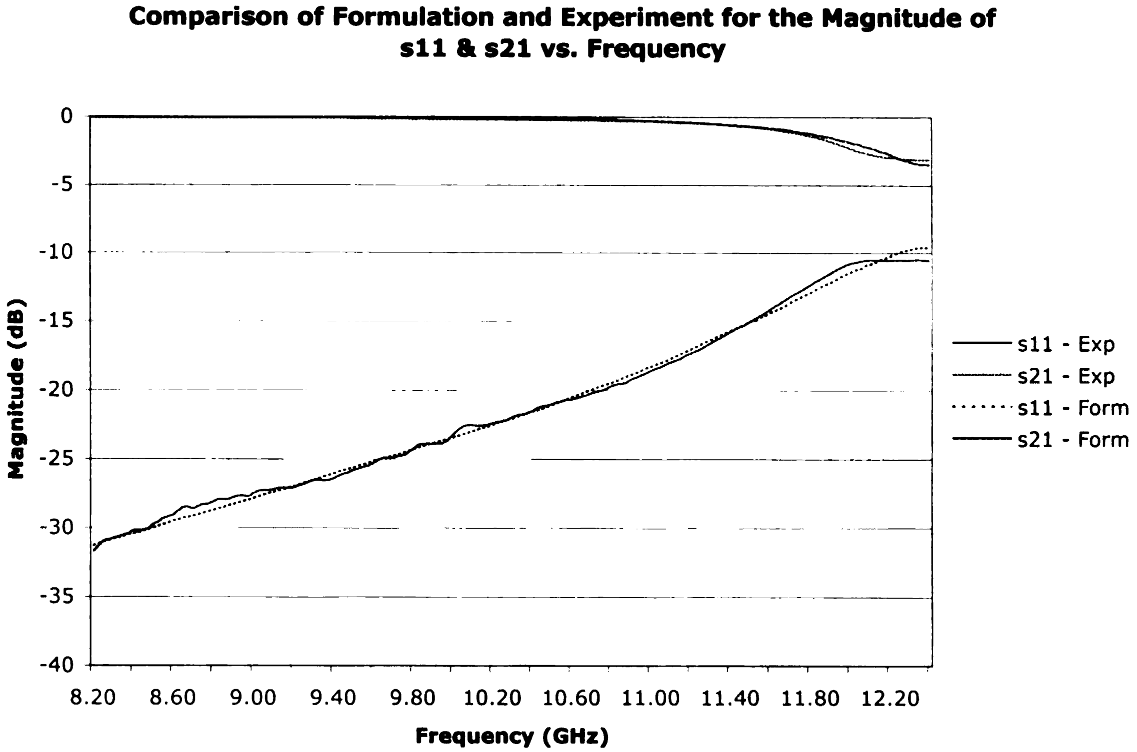

Figure 5.3. Comparison of the formulation results and experimental data, using the magnitude (dB) of the waveguide scattering parameters, for the radiation of the signal into a half-space vs. frequency (GHz).

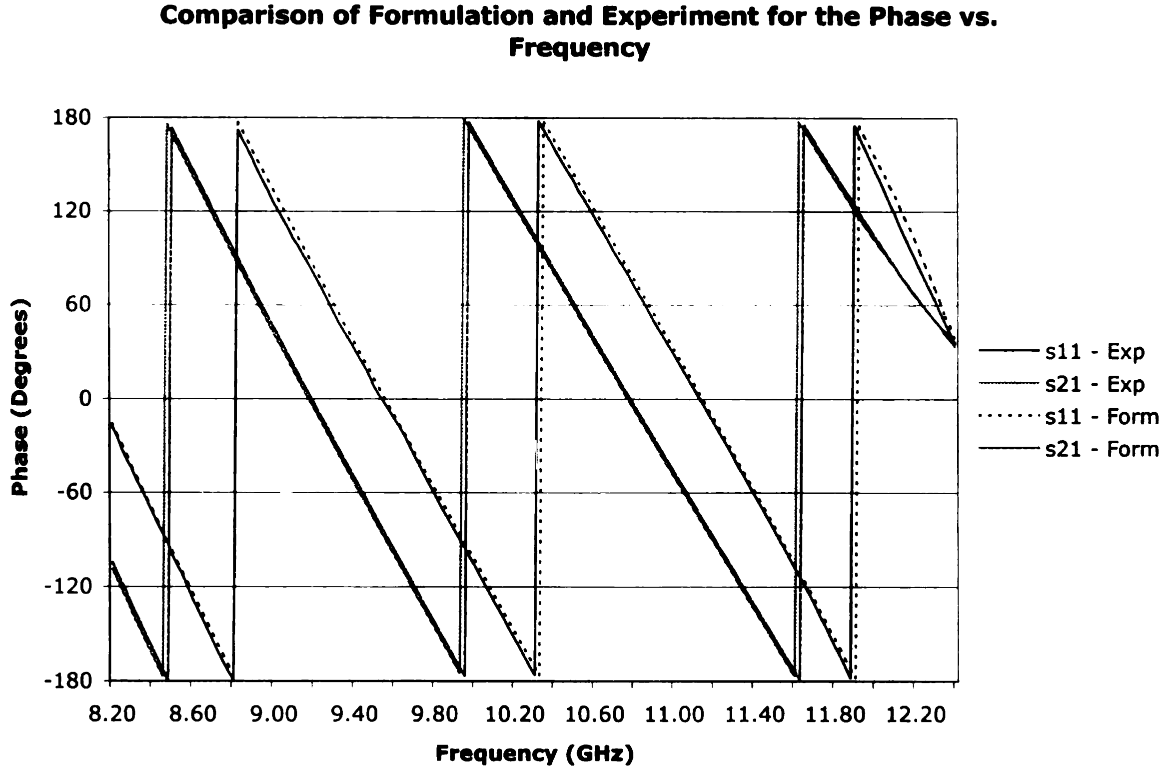

Figure 5.4. Comparison of the formulation results and experimental data, using the phase (degrees) of the waveguide scattering parameters, for the radiation of the signal into a half-space vs. frequency (GHz).

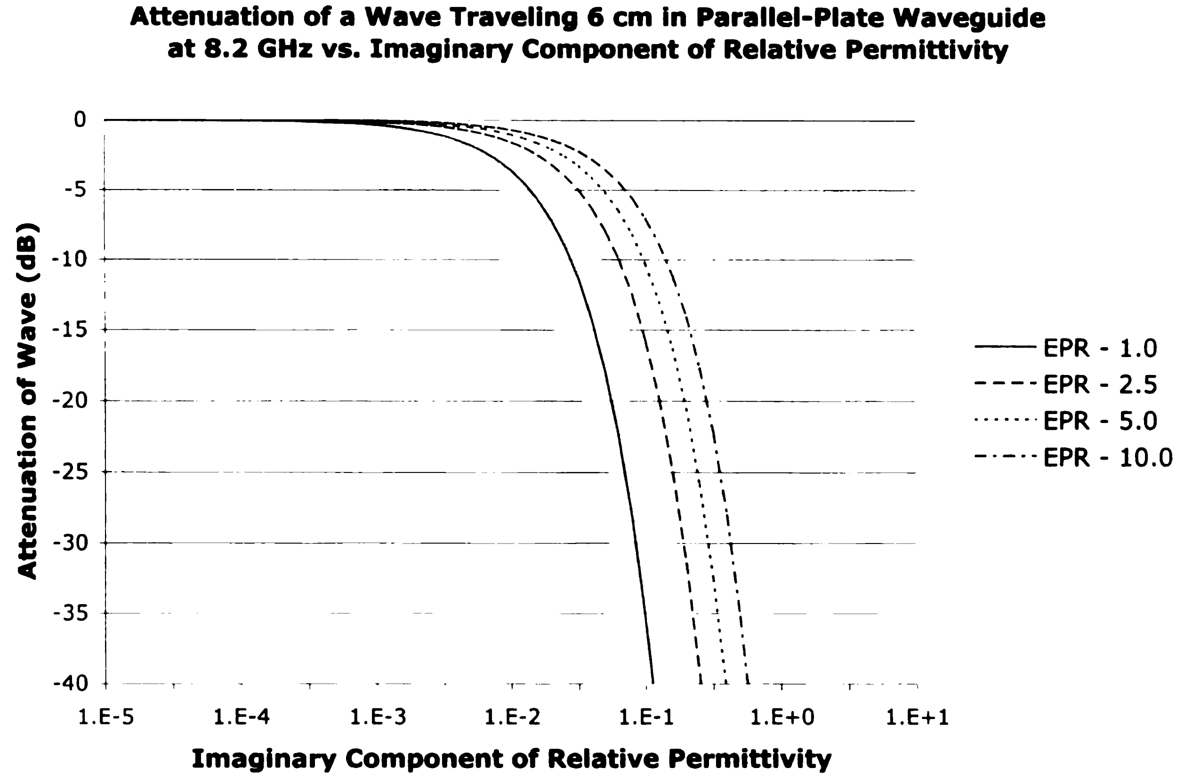

Figure 5.5. The attenuation (dB) of a wave traveling 6 cm in a parallel-plate waveguide, for various values of the real component of relative permittivity, at 8.2 GHz vs. the imaginary component of the relative permittivity.

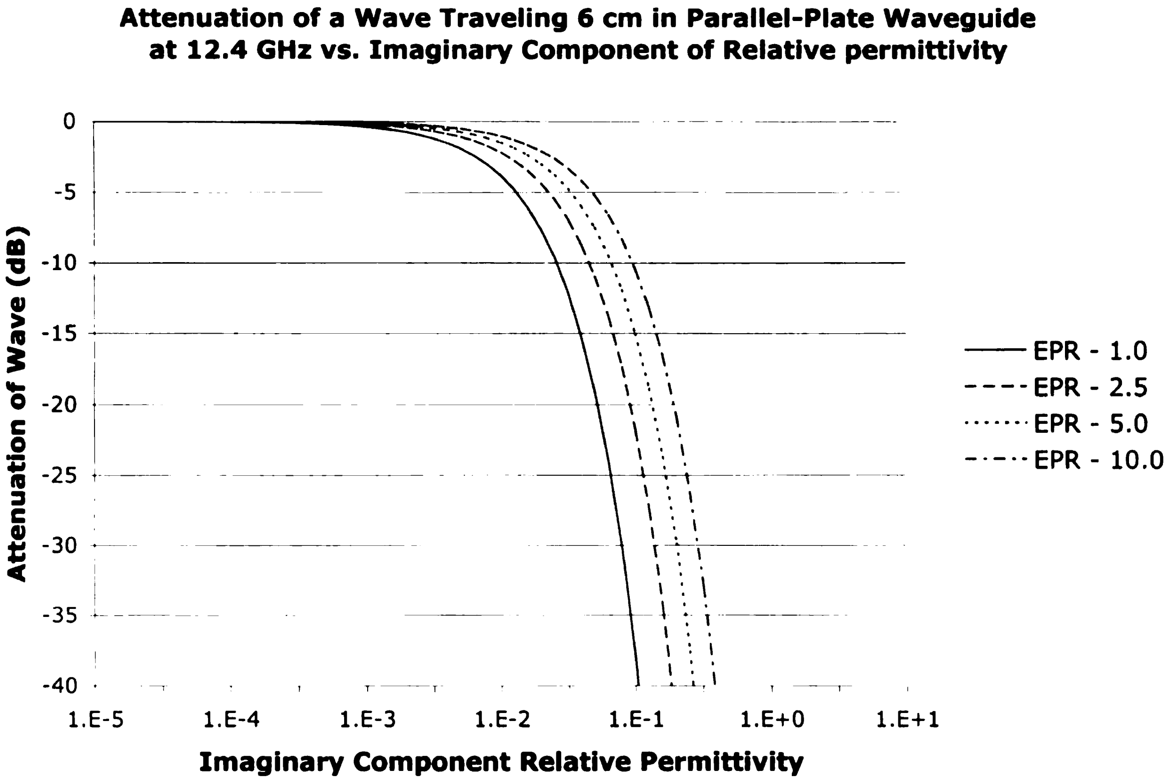

Figure 5.6. The attenuation (dB) of a wave traveling 6 cm in a parallel-plate waveguide, for various values of the real component of relative permittivity, at 12.4 GHz vs. the imaginary component of the relative permittivity.

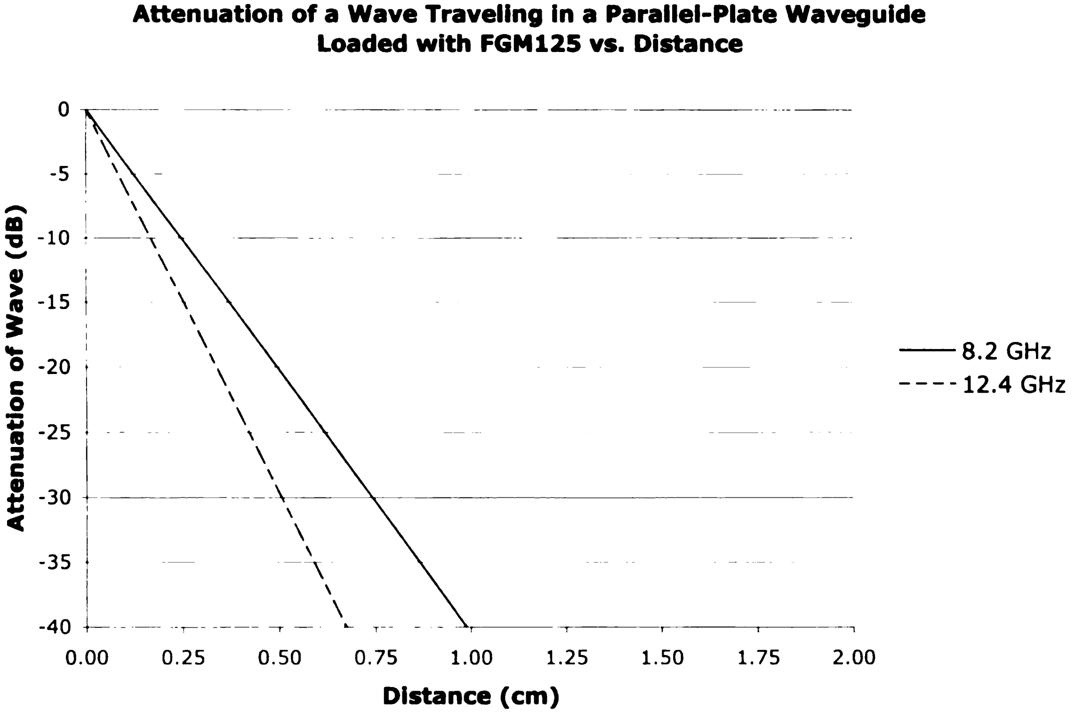

Figure 5.7. The attenuation (dB) of a wave traveling in a parallel-plate waveguide, at 8.2 and 12.4 GHz, loaded with FGM125 vs. distance (cm).

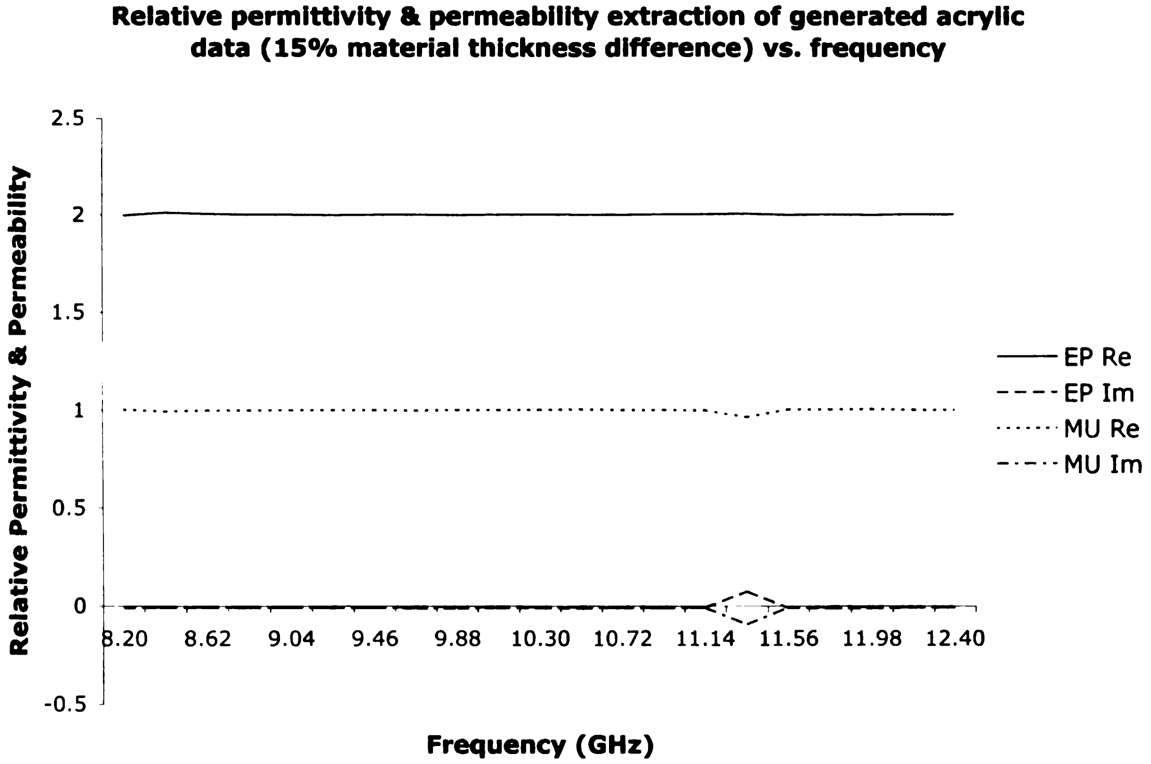

Figure 5.8. Relative permittivity and permeability extracted using generated acrylic data that has a 15 percent wavelength difference between the two material thicknesses.

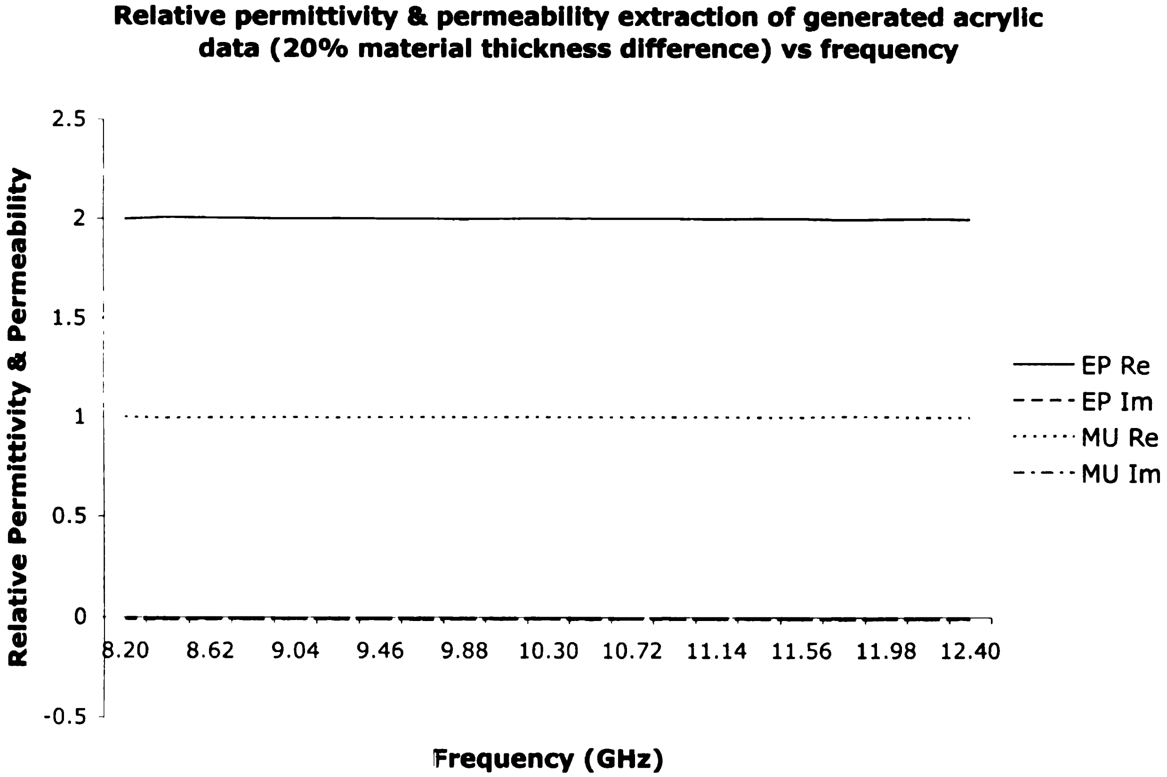

Figure 5.9. Relative permittivity and permeability extracted using generated acrylic data that has a 20 percent wavelength difference between the two material thicknesses.

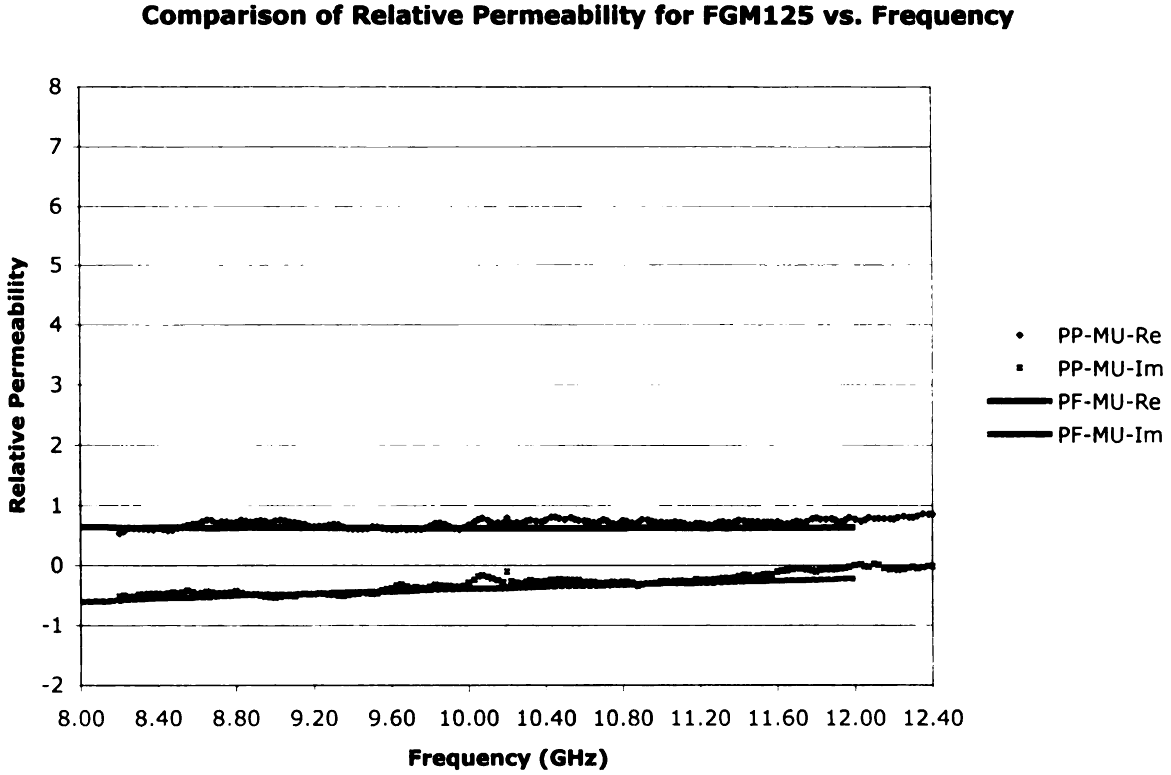

Figure 5.10. Comparison of the relative permeability, for the MagRAM FGM125, using a partially-filled rectangular waveguide method and the resonant antenna technique vs. frequency (GHz).

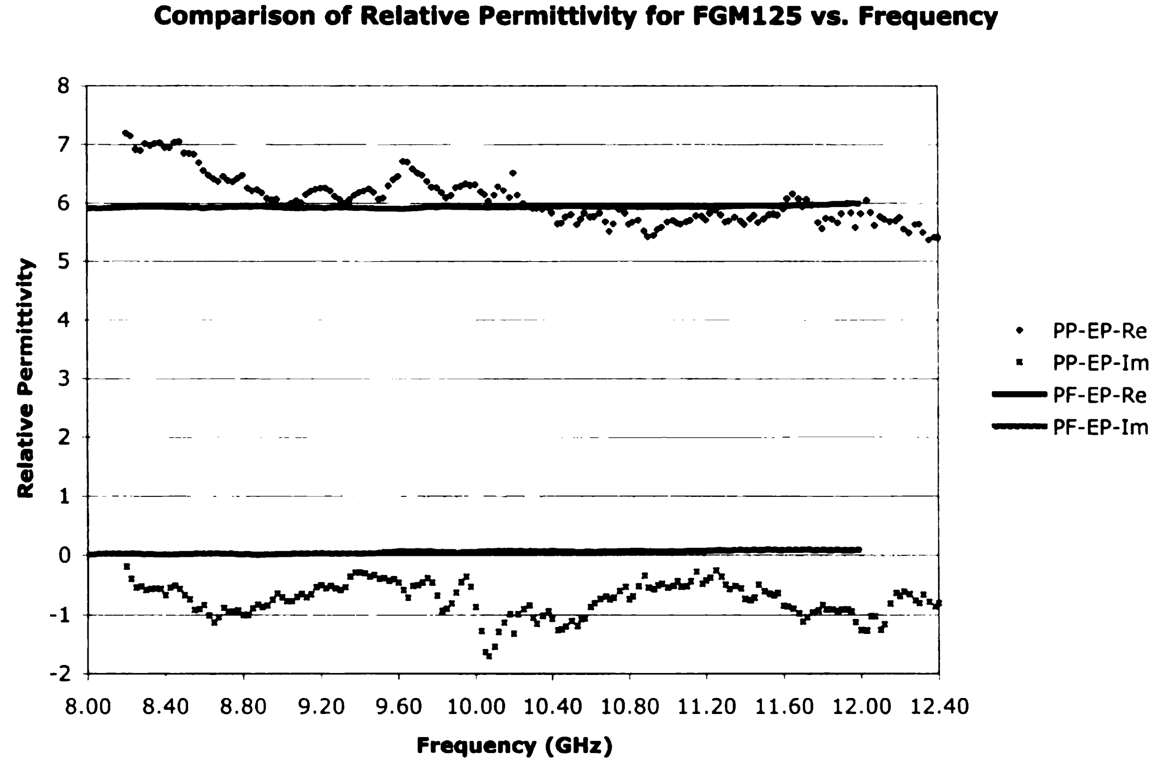

Figure 5.11. Comparison of the relative permittivity, for the MagRAM FGM125, using a partially-filled rectangular waveguide method and the resonant antenna technique vs. frequency (GHz).

CHAPTER 6

CONCLUSIONS

This dissertation has provided a waveguide slot-antenna technique for the non-destructive evaluation of a PEC backed lossy, simple media. The sample permittivity and permeability were found by using an iterative complex two-dimensional Newton's root-searching algorithm to compare the theoretical S-parameters obtained using the MFIE technique with the experimentally measured S-parameters obtained form the network analyzer.

The initial goal of this research was to extract both permittivity and permeability simultaneously with only a single experimental setup. This was not possible under the current formulation, thus a second material thickness was needed to perform the simultaneous extraction. A couple of special case tests were done to show that the extraction process, using the two separate thicknesses, was converging to the correct complex constitutive parameters. Then the waveguide slot-antenna material characterization technique was experimentally verified, through the comparison of a MagRAM sample, with a partially-filled rectangular waveguide measurement. The accuracy of the permittivity data suffered, likely due to a poor electric field interrogation of the material. This comparison demonstrated a proof of concept, and thus the validity of the technique.

6.1 Suggestions for Future Work

As this is initial research into the use of slot antennas for material characterization, many areas of future research are note worthy. First, looking into why the single layer of material was unable to simultaneously perform a full characterization of the material. This should include looking into various extraction methods to see if the 2-D Newton's method used was not the appropriate choice. Next, a study into increasing the coupling though the slot. The most practical way to achieve this is to relax the assumption of a long an narrow slot, and increase the size of the aperture. Another area of interest is using multiple slots. This should also increase coupling to the material, but could also help achieve the initial goal of using only a single material thickness to fully characterize the material. Finally, looking into the ability to extract the complex constitutive parameters for two-layers, which could be done using a two-layer parallel-plate Green's function.

APPENDICES

APPENDIX A

MAXWELL'S EQUATIONS AND HERTZIAN POTENTIALS

A.1 Introduction

Appendix A provides an overview of Maxwell's Equations and Hertzian potentials due to a magnetic source. A development of the wave equations, for both EM fields and Hertzian potentials, is also included.

A.2 Maxwell's Equations and the Wave Equation for $\vec{E}$ and $\vec{H}$

Maxwell's equations, due to a magnetic source, for a simple medium (linear, homogeneous and isotropic) and the magnetic source continuity equation in the spectral-domain point form are

$$\nabla \times \vec{E}(\vec{r}) = -\vec{J}_m(\vec{r}) - j\omega\mu\vec{H}(\vec{r}) \tag{A.1}$$

$$\nabla \times \vec{H}(\vec{r}) = j\omega\epsilon\vec{E}(\vec{r}) \tag{A.2}$$

$$\nabla \cdot \epsilon\vec{E}(\vec{r}) = 0 \tag{A.3}$$

$$\nabla \cdot \mu\vec{H}(\vec{r}) = \rho_m(\vec{r}) \tag{A.4}$$

$$\nabla \cdot \vec{J}_m(\vec{r}) = -j\omega\rho_m(\vec{r}) \tag{A.5}$$

where $\vec{J}_m$ is a volume magnetic current density, ρ_m is the density of the magnetic charge, and $\epsilon = \tilde{\epsilon}(1 - j\sigma/\omega\tilde{\epsilon})$ is the effective complex permittivity. The wave equation for $\vec{E}$ is found by taking the curl of (A.1), substituting (A.2) into the resulting relation, then applying the vector identity $\nabla \times \nabla \times \vec{E} = \nabla\left(\nabla \cdot \vec{E}\right) - \nabla^2\vec{E}$ and using equation (A.3). The result is

$$\nabla^2\vec{E} + k^2\vec{E} = \nabla \times \vec{J}_m \tag{A.6}$$

where $k^2 = \omega^2\mu\epsilon$. Similarly, the wave equation for $\vec{H}$ is determined by taking the curl of (A.2), substituting (A.1) into the resulting equation and then using the vector identity $\nabla \times \nabla \times \vec{E} = \nabla\left(\nabla \cdot \vec{E}\right) - \nabla^2\vec{E}$ and also equations (A.4) and (A.5). The result is

$$\nabla^2\vec{H} + k^2\vec{H} = j\omega\epsilon\vec{J}_m + \frac{1}{j\omega\mu}\nabla\left(\nabla \cdot \vec{J}_m\right) \tag{A.7}$$

A.3 MT Hertzian Potential

The primary use of Hertzian potentials is as a simplifying intermediate step to determining electric and magnetic fields. The MT Hertzian potential may be identified by observing that (A.3) implies that $\vec{E}$ is written as

$$\vec{E} = -j\omega\mu\nabla \times \vec{\pi}_h \tag{A.8}$$

since $\nabla \cdot \nabla \times \vec{\pi}_h = 0$ by vector identity. The magnetic field is then determined by substituting (A.8) into (A.2) and using the vector identity $\nabla \times \nabla\Phi = 0$. This leads to

$$\vec{H} = k^2\vec{\pi}_h + \nabla\phi \tag{A.9}$$

The wave equation for $\vec{\pi}_h$ is identified by substituting (A.8) and (A.9) into (A.1), applying the identity $\nabla \times \nabla \times \vec{\pi}_h = \nabla\left(\nabla \cdot \vec{\pi}_h\right) - \nabla^2\vec{\pi}_h$ and then using the Lorentz gauge condition $\Phi = \nabla \cdot \vec{\pi}_h$. The resulting Helmholtz wave equation is

$$\nabla^2\vec{\pi}_h + k^2\vec{\pi}_h = -\frac{\vec{J}_m}{j\omega\mu} \tag{A.10}$$

Equation (A.10) is decomposed into three scalar equations in Cartesian coordinates (reducing mathematical complexity) as follows

$$\nabla^2\vec{\pi}_{h_\alpha} + k^2\vec{\pi}_{h_\alpha} = -\frac{\vec{J}_{m_\alpha}}{j\omega\mu} \tag{A.11}$$

where $\alpha = x, y, z$. Substituting $\Phi = \nabla \cdot \vec{\pi}_h$ into (A.9) leads to

$$\vec{H} = k^2 \vec{\pi}_h + \nabla (\nabla \cdot \vec{\pi}_h) \tag{A.12}$$

Since (A.10) shows that $\vec{\pi}_h$ is maintained by a magnetic current, it is called a MT Hertzian potential (ET Hertzian potentials are also possible, but since they do not occur in this problem they are not discussed here). A comparison of (A.11) with (A.6) or (A.7) demonstrates why Hertzian potentials are introduced in mathematical analysis of EM problems. In equation (A.11), each component of $\vec{\pi}_h$ is directly related to each component of $\vec{J}_m$. The relationship between $\vec{E}, \vec{J}$ in (A.6) or $\vec{H}, \vec{J}$ in (A.7) is more complicated and thus a solution is generally strongly singular and more difficult to obtain. Thus, it is easier to solve for $\vec{\pi}_h$ first then determine $\vec{E}$ and $\vec{H}$ using (A.8) and (A.12).

APPENDIX B

PROPERTIES OF RECTANGULAR WAVEGUIDES AND CAVITIES

B.1 Introduction

An analysis of the guided wave structures used in Chapters 2 and 4 is needed to ensure proper application in the formulations developed. Appendix B develops the characteristic eigenmode fields of the rectangular waveguide, for both the y and z-axial directions. These modal fields are then extended to Green's functions for both the rectangular waveguide and cavity respectively. Followed by the development of the rectangular waveguide scattering parameters for the y-axial direction modal fields.

B.2 Waveguide Modes

In the interior of a rectangular waveguide, Maxwell's equations (A.1-A.4) can be divided into two basic sets of solutions or modes. For one set of modes no longitudinal or axial magnetic field component exists, these modes are called transverse magnetic (TM) modes. The other basic set of modes have an axial magnetic field but no axial electric field component, this set is referred to as the transverse electric (TE) modes [58]. The TE modes are used in the rectangular waveguides (with $a > b$, see Figure B.1), because the TE_{10} mode is the dominant mode due to the fact is has the lowest cutoff frequency.

The cutoff frequency of the TE_{mn} mode is given by

$$f_{c,mn} = \frac{ck_c}{2\pi} = \frac{c\sqrt{m^2b^2 + n^2a^2}}{2ab} \tag{B.1}$$

where c is the speed of light in free space, a is the width of rectangular waveguide, b is the height, and m and n are the modal values [58]. The cutoff frequency helps define the bandwidth of the waveguide, where the first higher order mode to propagate defines the upper bound of the bandwidth, and the cutoff frequency defines the lower bound of the bandwidth.

B.2.1 Geometrical Configuration

Consider the cross-sectional view of a rectangular waveguide shown in Figure B.1. The origin is located in the center of the bottom plate and the waveguide has dimensions of width $-a/2 \leq x \leq a/2$ and height $y = b$. The width (a) will in general be twice the height (b).

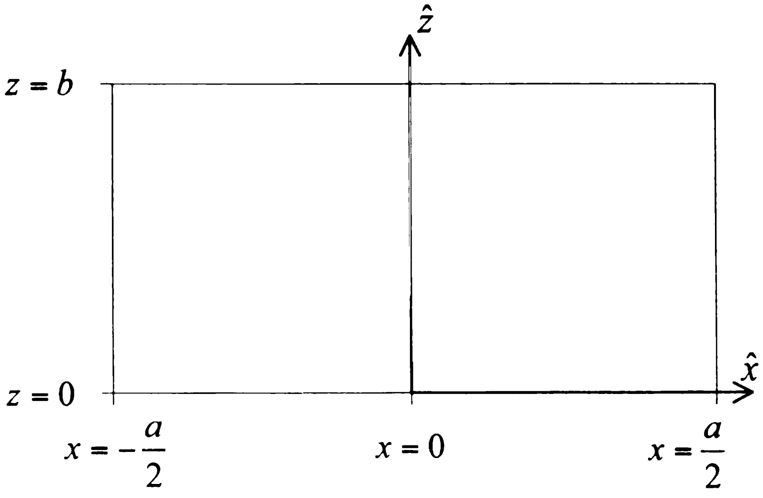

Figure B.1. Geometrical Configuration: Rectangular waveguide (y-axially direction)

B.2.2 Modal Analysis (TE_x Modes)

Generally when describing a set of TE modes, the direction of propagation has no electric-field component. However, sometimes the geometry of the problem lends itself to an alternative set of modes. In the case of the rectangular waveguide used in the formulations of Chapters 2 and 4, where the direction of propagation is the y-direction, the TE_x modes are the most complete set of modes. This is because the transverse slot can only have an equivalent x-directed magnetic current. This can alternatively be reasoned by noting that the slot causes higher order modes to be scattered, thus a superposition of TE_y and TM_y modes would be needed to have a complete set of modes. This superposition of TE_y and TM_y modes is seen to equal the set of TE_x modes, for propagation in the y-direction [60], thus the latter set of modes is developed here.

B.2.2.1 y-axial direction

To develop the desired set of modes, the appropriate choice of the MT Hertzian potential is necessary. To ensure that the x-directed component of the electric-field is equal zero and the x-directed component of the magnetic field is not equal to zero, the appropriate choice of the MT Hertzian potential is

$$\vec{\pi}_h = \hat{x}\pi_h \tag{B.2}$$

Then, substituting (B.2) into (A.8) and (A.12) and carrying out the vector operations gives respectively for the EM fields

$$\vec{E} = j\omega\mu_0\hat{x} \times \nabla_{t_x}\pi_h \tag{B.3}$$

and

$$\vec{H} = \nabla_{t_x}\frac{\partial}{\partial x}\pi_h + \hat{x}\left(k_0^2 + \frac{\partial^2}{\partial x^2}\right)\pi_h \tag{B.4}$$

where the transverse Laplacin operator with respect to the x-direction is

$$\nabla_{t_x} = \hat{y}\frac{\partial}{\partial y} + \hat{z}\frac{\partial}{\partial z} \tag{B.5}$$

To solve the homogeneous Helmholtz equation

$$\nabla^2\pi_h + k_0^2\pi_h = 0 \tag{B.6}$$

in terms of longitudinal and transverse components requires writing the MT Hertzian potential as

$$\pi_h = A_{\alpha\beta}\pi_h\left(x, z\right)e^{\mp\Gamma y} \tag{B.7}$$

Then utilizing (B.7) in (B.6) along with the separation of variables technique leads to

$$\pi_h = A_{\alpha\beta}\left[A\cos\left(k_x x\right) + B\sin\left(k_x x\right)\right]\left[C\cos\left(k_z z\right) + D\sin\left(k_z z\right)\right]e^{\mp\Gamma y} \tag{B.8}$$

where the cutoff wavenumber and propagation constant are respectively

$$k_c^2 = k_0^2 + \Gamma^2 = k_x^2 + k_z^2 \tag{B.9}$$

$$\Gamma = jk_y \tag{B.10}$$

The boundary conditions on the PEC waveguide walls are

$$E_{y,z}|_{x=-a/2,a/2} = 0 \rightarrow \pi_h|_{x=-a/2,a/2} = 0 \tag{B.11}$$

$$E_y|_{z=t,b_1} = 0 \rightarrow \frac{\partial\pi_h}{\partial z}|_{z=t,b_1} = 0 \tag{B.12}$$

where the partial derivative required for enforcing the boundary conditions is given as

$$\frac{\partial\pi_h}{\partial z} = A_{\alpha\beta}k_z\left[A\cos\left(k_x x\right) + B\sin\left(k_x x\right)\right]\left[-C\sin\left(k_z z\right) + D\cos\left(k_z z\right)\right]e^{\mp\Gamma y} \tag{B.13}$$

leading to the generating eigenfunction for the γ^{th} mode as

$$\pi_{h_\gamma} = A_\gamma \sin\left[k_{x_\gamma}\left(x - a/2\right)\right]\cos\left[k_{z_\gamma}\left(z - t\right)\right]e^{\mp jk_{y_\gamma}y} \tag{B.14}$$

with the wavenumbers defined as

$$\begin{aligned} k_{x_\gamma} &= \tfrac{\alpha\pi}{a}, \alpha = 1, 2, 3, ... \\ k_{z_\gamma} &= \tfrac{\beta\pi}{b}, \beta = 0, 1, 2, ... \quad where \quad b = (b_1 - t) \\ k_{c\gamma}^2 &= k_0^2 - k_{y\gamma}^2 = k_{x\gamma}^2 + k_{z\gamma}^2 \end{aligned} \tag{B.15}$$

Substituting (B.14) into (B.3) and (B.4) and applying the mathematical operations, the modal fields are summarized as follows

$$\vec{E}_\gamma^\pm(\vec{r}) = \left[\pm\hat{z}A_{z_\gamma}e_{z_\gamma}(\vec{r}) + \hat{y}A_{y_\gamma}e_{y_\gamma}(\vec{r})\right]e^{\mp jk_{y_\gamma}y} \tag{B.16}$$

$$\vec{H}_\gamma^\pm(\vec{r}) = \left[\vec{h}_{t_\gamma}(\vec{r}) \pm \hat{y}\tilde{A}_{y_\gamma}h_{y_\gamma}(\vec{r})\right]e^{\mp jk_{y_\gamma}y} \tag{B.17}$$

$$e_{z_\gamma}(\vec{r}) = \sin\left[k_{x_\gamma}(x - a/2)\right]\cos\left[k_{z_\gamma}(z - t)\right] \quad ; \quad A_{z_\gamma} = \omega\mu_0 k_{y_\gamma} A_\gamma \tag{B.18}$$

$$e_{y_\gamma}(\vec{r}) = \sin\left[k_{x_\gamma}(x - a/2)\right]\sin\left[k_{z_\gamma}(z - t)\right] \quad ; \quad A_{y_\gamma} = j\omega\mu_0 k_{z_\gamma} A_\gamma \tag{B.19}$$

$$\vec{h}_{t_\gamma}(\vec{r}) = \hat{x}\tilde{A}_{x_\gamma}h_{x_\gamma}(\vec{r}) + \hat{z}\tilde{A}_{z_\gamma}h_{z_\gamma}(\vec{r}) \tag{B.20}$$

$$h_{x_\gamma}(\vec{r}) = \sin\left[k_{x_\gamma}(x - a/2)\right]\cos\left[k_{z_\gamma}(z - t)\right] \quad ; \quad \tilde{A}_{x_\gamma} = \left(k_0^2 - k_x^2\right)A_\gamma \tag{B.21}$$

$$h_{z_\gamma}(\vec{r}) = \cos\left[k_{x_\gamma}(x - a/2)\right]\sin\left[k_{z_\gamma}(z - t)\right] \quad ; \quad \tilde{A}_{z_\gamma} = -k_{x_\gamma}k_{z_\gamma}A_\gamma \tag{B.22}$$

$$h_{y_\gamma}(\vec{r}) = \cos\left[k_{x_\gamma}(x - a/2)\right]\cos\left[k_{z_\gamma}(z - t)\right] \quad ; \quad \tilde{A}_{y_\gamma} = -jk_{x_\gamma}k_{y_\gamma}A_\gamma \tag{B.23}$$

B.2.2.2 z-axial direction

Consider the cross-sectional view of a rectangular waveguide shown in Figure B.2. The origin is located in the center of the waveguide having dimensions of width $-a_c/2 \le x \le a_c/2$ and height $-b_c/2 \le y \le b_c/2$.

Using the same steps as the previous section, the TE_x modes with propagation

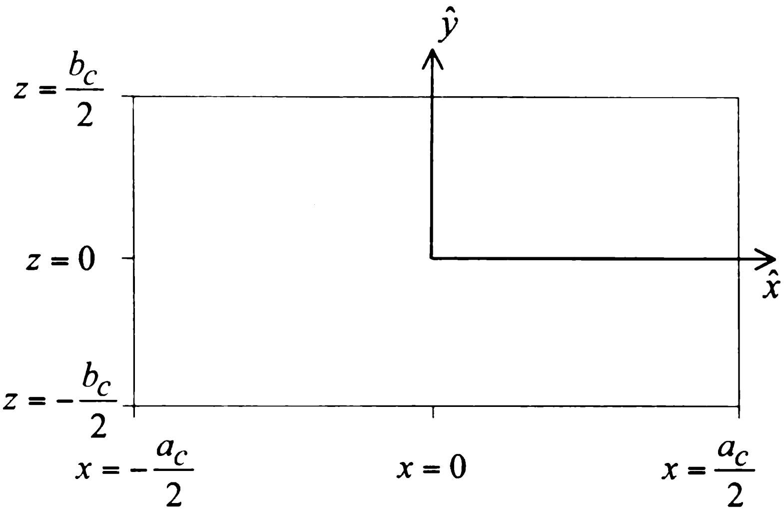

Figure B.2. Geometrical Configuration: Rectangular waveguide (z-axially direction)

in the z-direction may be summarized as follows

$$\vec{E}^{\pm}_{\Gamma}(\vec{r}) = \left[-\hat{z}A_{z\Gamma}e_{z\Gamma}(x,y) \mp \hat{y}A_{y\Gamma}e_{y\Gamma}(x,y)\right] e^{\mp jk_{z\Gamma}z} \tag{B.24}$$

$$\vec{H}^{\pm}_{\Gamma}(\vec{r}) = \left[\vec{h}_{t\Gamma}(x,y) \mp \hat{z}\tilde{A}_{z\Gamma}h_{z\Gamma}(x,y)\right] e^{\mp jk_{z\Gamma}z} \tag{B.25}$$

$$e_{z\Gamma}(x,y) = \sin\left[k_{x\Gamma}(x - a_c/2)\right]\sin\left[k_{y\Gamma}(y - b_c/2)\right] \quad ; \quad A_{z\Gamma} = j\omega\mu_0 k_{y\Gamma}A_\Gamma \tag{B.26}$$

$$e_{y\Gamma}(x,y) = \sin\left[k_{x\Gamma}(x - a_c/2)\right]\cos\left[k_{y\Gamma}(y - b_c/2)\right] \quad ; \quad A_{y\Gamma} = \omega\mu_0 k_{z\Gamma}A_\Gamma \tag{B.27}$$

$$\vec{h}_{t\Gamma}(x,y) = \hat{x}\tilde{A}_{x\Gamma}h_{x\Gamma}(x,y) - \hat{y}\tilde{A}_{y\Gamma}h_{y\Gamma}(x,y) \tag{B.28}$$

$$h_{x\Gamma}(x,y) = \sin\left[k_{x\Gamma}(x - a_c/2)\right]\cos\left[k_{y\Gamma}(y - b_c/2)\right] \quad ; \quad \tilde{A}_{x\Gamma} = \left(k_0^2 - k_x^2\right)A_\Gamma \tag{B.29}$$

$$h_{z\Gamma}(x,y) = \cos\left[k_{x\Gamma}(x - a_c/2)\right]\cos\left[k_{y\Gamma}(y - b_c/2)\right] \quad ; \quad \tilde{A}_{z\Gamma} = jk_{x\Gamma}k_{z\Gamma}A_\Gamma \tag{B.30}$$

$$h_{y_\Gamma}(x,y) = \cos\left[k_{x_\Gamma}(x-a_c/2)\right]\sin\left[k_{y_\Gamma}(y-b_c/2)\right] \quad ; \quad \tilde{A}_{y_\Gamma} = k_{x_\Gamma}k_{y_\Gamma}A_\Gamma \tag{B.31}$$

$$\begin{aligned} k_{x_\Gamma} &= \tfrac{\alpha\pi}{a_c}, \alpha = 1,2,3,\ldots \\ k_{y_\Gamma} &= \tfrac{\beta\pi}{b_c}, \beta = 0,1,2,\ldots \\ k_{c_\Gamma}^2 &= k_0^2 - k_{z_\Gamma}^2 = k_{x_\Gamma}^2 + k_{y_\Gamma}^2 \end{aligned} \tag{B.32}$$

B.3 Green's Functions

In this section the Green's functions for the rectangular waveguide and cavity are developed. The rectangular waveguide Green's function is determined by using the Lorentz reciprocity theorem, while the rectangular cavity Green's function is determined by using the method of scattering superposition [61].

B.3.1 Rectangular Waveguide

Consider the waveguide configuration given in Figure B.3. The slot is assumed to be cut in the bottom waveguide wall between cross-sectional planes CS_1 at $y = y_1$ and CS_2 at $y = y_2$. It also supports a field $\vec{E}_s$ that is excited by the incident TE_y^{10} mode.

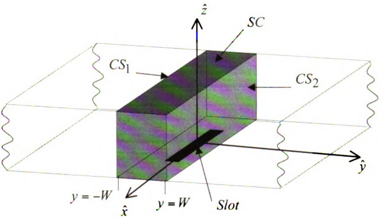

Figure B.3. Rectangular waveguide with slot discontinuity

B.3.1.1 Slot Excited Modal Fields

The first step in the determination of the desired rectangular waveguide Green's function, is to express the scattered waveguide fields, excited by the slot, using a modal expansion. These electric and magnetic field expressions are given as

$$\vec{E} = \sum_{\gamma} B_\gamma \vec{E}_\gamma^- (\vec{r}) = \sum_{\gamma} B_\gamma \left[-\hat{z} A_{z_\gamma} e_{z_\gamma} (x, z) + \hat{y} A_{y_\gamma} e_{y_\gamma} (x, z) \right] e^{j k_{y_\gamma} y} \tag{B.33}$$

$$\vec{H} = \sum_{\gamma} B_\gamma \vec{H}_\gamma^- (\vec{r}) = \sum_{\gamma} B_\gamma \left[\vec{h}_{t_\gamma} (x, z) - \hat{y} \tilde{A}_{y_\gamma} h_{y_\gamma} (x, z) \right] e^{j k_{y_\gamma} y} \tag{B.34}$$

and

$$\vec{E} = \sum_{\gamma} C_\gamma \vec{E}_\gamma^+ (\vec{r}) = \sum_{\gamma} C_\gamma \left[\hat{z} A_{z_\gamma} e_{z_\gamma} (x, z) + \hat{y} A_{y_\gamma} e_{y_\gamma} (x, z) \right] e^{-j k_{y_\gamma} y} \tag{B.35}$$

$$\vec{H} = \sum_{\gamma} C_\gamma \vec{H}_\gamma^+ (\vec{r}) = \sum_{\gamma} C_\gamma \left[\vec{h}_{t_\gamma} (x, z) + \hat{y} \tilde{A}_{y_\gamma} h_{y_\gamma} (x, z) \right] e^{-j k_{y_\gamma} y} \tag{B.36}$$

for $y < y_1$ and $y > y_2$ respectively.

B.3.1.2 Determination of Modal Expansion Coefficients

The next step is to determine the modal expansion coefficients by using the Lorentz reciprocity theorem on a source-free, bounded region S. The closed boundary of this source-free region S consists of the cross-sectional surfaces CS_1 and CS_2, and the conducting waveguide surface S_c, or

$$S = S_C + CS_1 + CS_2 \tag{B.37}$$

The Lorentz reciprocity theorem applied to this source-free region is written as

$$\oint_S \hat{n} \cdot \left(\vec{E}^a \times \vec{H}^b - \vec{E}^b \times \vec{H}^a \right) dS = 0 \tag{B.38}$$

where the fields

$$\vec{E}^a = \vec{E}$$
$$\vec{H}^a = \vec{H} \tag{B.39}$$

represent the EM fields (described in section B.2.2.1) radiated into the bounded waveguide region by the slot aperture field $\vec{E}_s$ and

$$\vec{E}^b = \vec{E}_\gamma^\pm$$
$$\vec{H}^b = \vec{H}_\gamma^\pm \tag{B.40}$$

are the waveguide modal field (described in equations (B.33-B.36)) traveling in the $\pm y$-direction. Substituting the fields in (B.39) and (B.40) into (B.38) gives the specialized form of the Lorentz reciprocity theorem

$$\oint_S \hat{n} \cdot \left(\vec{E} \times \vec{H}_\gamma^\pm - \vec{E}_\gamma^\pm \times \vec{H} \right) dS = 0 \tag{B.41}$$

where the superposition of the three boundaries set equal to zero determines the modal expansion coefficients. Solving for the conducting surface S_C by first using a vector identity [57] gives

$$\int_{S_C} \hat{n} \cdot \left(\vec{E} \times \vec{H}_\gamma^\pm - \vec{E}_\gamma^\pm \times \vec{H} \right) dS = \int_{S_C} \left[\left(\hat{n} \times \vec{E} \right) \cdot \vec{H}_\gamma^\pm - \left(\hat{n} \times \vec{E}_\gamma^\pm \right) \cdot \vec{H} \right] dS \tag{B.42}$$

Application of the PEC boundary condition [58] results in the expression

$$\int_{S_C} \hat{n} \cdot \left(\vec{E} \times \vec{H}_\gamma^\pm - \vec{E}_\gamma^\pm \times \vec{H} \right) dS = \int_{S_a} \hat{n} \cdot \left(\vec{E}_S \times \vec{H}_\gamma^\pm \right) dS \tag{B.43}$$

where the only remaining contribution is due to the slot electric-field.

Solving the cross-sectional surface CS_1 next (where the outward normal is defined as $-\hat{y}$) leads to

$$CS_1 = \int_{CS_1} -\hat{y} \cdot \left(\vec{E} \times \vec{H}_{\gamma}^{\pm} - \vec{E}_{\gamma}^{\pm} \times \vec{H} \right) dS \tag{B.44}$$

with the substitution of the scattered and modal field expressions from (B.39) and (B.40) leading to

$$\begin{aligned} CS_1 = \textstyle\sum_{\gamma} B_{\gamma} \int_{CS_1} -\hat{y} \cdot \Big[&- \left(\hat{z} A_{z_\gamma} e_{z_\gamma} (x,z) \times \vec{h}_{t_\gamma} (x,z) \right) e^{j\left(k_{y\gamma} \mp k_{y\gamma}\right) y_1} \\ &\mp \left(\hat{z} A_{z_\gamma} e_{z_\gamma} (x,z) \times \vec{h}_{t_\gamma} (x,z) \right) e^{j\left(\mp k_{y\gamma} + k_{y\gamma}\right) y_1} \Big] \end{aligned} \tag{B.45}$$

Then by defining the mode orthogonality relationship as

$$S_{\gamma} \delta_{\gamma\iota} = \int_{CS} dS \hat{y} \cdot \left(\vec{e}_{t_\gamma} (x,z) \times \vec{h}_{t_\iota} (x,z) \right) \tag{B.46}$$

equation (B.45) is simplified to

$$CS_1 = B_{\gamma} S_{\gamma} e^{j(1 \mp 1) k_{y\gamma} y_1} (1 \pm 1) \tag{B.47}$$

where the $\mp$ is associated with forward and backward traveling waves respectively.

Similar steps are taken to solve the second cross-sectional surface CS_2 (where the outward normal is defined as $\hat{y}$) giving

$$CS_2 = \int_{CS_2} \hat{y} \cdot \left(\vec{E} \times \vec{H}_{\gamma}^{\pm} - \vec{E}_{\gamma}^{\pm} \times \vec{H} \right) dS \tag{B.48}$$

Substitution of the scattered and modal field expressions from (B.39) and (B.40) along with simplifying the expression using (B.46), leads to

$$CS_2 = C_{\gamma} S_{\gamma} e^{j(-1 \mp 1) k_{y\gamma} y_2} (1 \mp 1) \tag{B.49}$$

where the $\mp$ is again associated with the forward and backward traveling waves respectively.

Superposing the terms in (B.43), (B.47), and (B.49) and setting them equal to zero generates the expression for all values of γ as

$$\begin{aligned} B_\gamma S_\gamma e^{j(1\mp 1)k_{y_\gamma} y_1}(1\pm 1) + C_\gamma S_\gamma e^{j(-1\mp 1)k_{y_\gamma} y_2}(1\mp 1) \\ + \textstyle\int_{S_a} \hat{n}\cdot\left(\vec{E}_S \times \vec{H}_\gamma^{\pm}\right) dS = 0 \end{aligned} \tag{B.50}$$

Solving this equation using either the upper or lower sign and then rearranging the terms leads to the modal expansion coefficients as

$$B_\gamma = \frac{-1}{2S_\gamma}\int_{S_a} \hat{n}\cdot\left(\vec{E}_S \times \vec{H}_\gamma^{+}\right) dS \tag{B.51}$$

and

$$C_\gamma = \frac{-1}{2S_\gamma}\int_{S_a} \hat{n}\cdot\left(\vec{E}_S \times \vec{H}_\gamma^{-}\right) dS \tag{B.52}$$

respectively. Substituting the appropriate fields into the mode orthogonality relationship, the mode expansion constant is defined as

$$S_\gamma = \frac{A_{z_\gamma}\tilde{A}_{x_\gamma} ab}{2\epsilon_\gamma} \quad \ldots \quad \epsilon_\gamma = \begin{cases} 1 & for \quad \beta = 0 \\ 2 & for \quad \beta \neq 0 \end{cases} \tag{B.53}$$

Finally, the modal expansion coefficients are determined as

$$B_\gamma = -\frac{\epsilon_\gamma}{A_{z_\gamma} ab}\int_{S_a} dS E_y\left(\vec{r}'\right) \sin\left[k_{x_\gamma}\left(x' - a/2\right)\right] \cos\left[k_{z_\gamma}\left(z' - t\right)\right] e^{-jk_{y_\gamma} y'} \tag{B.54}$$

$$C_\gamma = -\frac{\epsilon_\gamma}{A_{z_\gamma} ab}\int_{S_a} dS E_y\left(\vec{r}'\right) \sin\left[k_{x_\gamma}\left(x' - a/2\right)\right] \cos\left[k_{z_\gamma}\left(z' - t\right)\right] e^{jk_{y_\gamma} y'} \tag{B.55}$$

B.3.1.3 Green's Function due to a Transverse Slot

The Green's function is now found by simply substituting the modal expansion coefficients into equations (B.34) and (B.36) (repeated here for convenience)

$$H_x^s = \sum_\gamma B_\gamma \tilde{A}_{x_\gamma} \vec{h}_{x_\gamma}(x,z)\, e^{jk_{y_\gamma} y} \quad \ldots \quad y < y' \tag{B.56}$$

$$H_x^s = \sum_\gamma C_\gamma \tilde{A}_{x_\gamma} \vec{h}_{x_\gamma}(x,z)\, e^{-jk_{y_\gamma} y} \quad \ldots \quad y > y' \tag{B.57}$$

and then manipulating the subsequent expressions into the form of equations (2.9) and (2.10). The resulting x-directed component of the magnetic field for all y and y' is

$$H_x^s = \left(k_0^2 + \frac{\partial^2}{\partial x^2}\right) \int_{S_a} dS \frac{E_y(\vec{r}')}{j\omega\mu_0} G_{WG}(\vec{r}|\vec{r}') \tag{B.58}$$

where the MT Hertzian potential is the dot product of the slot electric field and the resulting rectangular waveguide Green's function, due to a transverse slot cut in the lower broad wall, which is given as

$$\begin{aligned} G_{WG}(\vec{r}|\vec{r}') = \tfrac{1}{ab} \textstyle\sum_\gamma \frac{\epsilon_\gamma}{jk_{y_\gamma}} \sin\left[k_{x_\gamma}(x - a/2)\right] \sin\left[k_{x_\gamma}(x' - a/2)\right] \\ \cdot \cos\left[k_{z_\gamma}(z - t)\right] \cos\left[k_{z_\gamma}(z' - t)\right] e^{-jk_{y_\gamma}\left|y - y'\right|} \end{aligned} \tag{B.59}$$

B.3.2 Rectangular Cavity

The Green's function for the rectangular cavity derived in this appendix follows the development of Tai [61]. This approach involves starting with the functions already available for a rectangular waveguide of the same cross-sectional dimensions and then applies the method of scattering superposition to find the desired function. The method of scattering superposition is applied in two separate steps. The first step is to generate the Green's function for the semi-infinite waveguide, with a PEC plate placed at the $z = c_c$ interface. The second step is to generate the Green's function for the rectangular cavity with a second PEC plate placed at the $z = 0$ interface.

To solve for the Green's functions by placing PEC plates at the interfaces $z = 0, c_c$, the PEC boundary condition (tangential electric-fields equals zero) is applied to the fields at these locations. Since only the y-directed component of the electric-field is tangential at both interfaces, it is the only component of the electric-field that is represented here. To develop the expression for the y-directed component of the electric-field, the modal fields of section B.2.2.2 are used to derive a rectangular waveguide Green's function using the derivation in section B.3.1. The y-directed component of the electric-field, that is valid for all z and z', of an infinite rectangular waveguide is thus represented as

$$E_y = -j\omega\mu_0 \frac{\partial}{\partial z} \int_{S_a} dS \quad G_{WG}\left(\vec{r}|\vec{r}'\right) \frac{E_y\left(\vec{r}'\right)}{j\omega\mu_0} \tag{B.60}$$

where the Green's function is represented as

$$\begin{aligned} G_{WG}\left(\vec{r}|\vec{r}'\right) = \frac{1}{a_c b_c} \sum_{\Gamma} \frac{\epsilon_\Gamma}{j k_{z_\Gamma}} & \sin\left[k_{x_\Gamma}\left(x - a_c/2\right)\right] \sin\left[k_{x_\Gamma}\left(x' - a_c/2\right)\right] \\ & \cdot \cos\left[k_{y_\Gamma}\left(y - b_c/2\right)\right] \cos\left[k_{y_\Gamma}\left(y' - b_c/2\right)\right] e^{-j k_{z_\Gamma}\left|z - z'\right|} \end{aligned} \tag{B.61}$$

Substituting this Green's function into the field expression and rearranging terms so only the z-dependence is considered, leads to the following

$$E_y = E_y\left(x, y|x', y'\right) \frac{\partial}{\partial z}\left[e^{\mp j k_{z_\Gamma} z} e^{\pm j k_{z_\Gamma} z'}\right] \tag{B.62}$$

Now that the necessary field is developed, the method of scattering superposition may be applied to generate the first Green's function for a semi-infinite rectangular waveguide. This is accomplished by added a scattering term to the field expression in (B.62) that accounts for the waves scattered off the PEC interface at $z = c_c$. The resulting field is

$$E_y = E_y\left(x, y|x', y'\right) \frac{\partial}{\partial z} \left[e^{\mp jk_{z_\Gamma} z} e^{\pm jk_{z_\Gamma} z'} + A_{s1} e^{jk_{z_\Gamma} z} e^{jk_{z_\Gamma} z'} \right] \tag{B.63}$$

where applying the appropriate boundary condition determines the constant A_{s1} as

$$A_{s1} = e^{-jk_{y_\Gamma} 2c_c} \tag{B.64}$$

Substitution of this constant back into (B.63) and then applying mathematical manipulation to the field for the $z > z'$ and $z < z'$ cases respectively, leads to

$$E_y = E_y\left(x, y|x', y'\right) \frac{\partial}{\partial z} 2 \begin{bmatrix} \cos\left[k_{z_\Gamma}\left(z - c_c\right)\right] e^{jk_{z_\Gamma}\left(z' - c_c\right)} \\ e^{jk_{z_\Gamma}\left(z - c_c\right)} \cos\left[k_{z_\Gamma}\left(z' - c_c\right)\right] \end{bmatrix} \tag{B.65}$$

e.g. the representation of the y-directed component of the electric-field for a semi-infinite rectangular waveguide. The second step is to generate the desired Green's function for the rectangular cavity. Just as before, this is accomplished by adding a scattering term to the field expression in (B.65) that accounts for the waves scattered off the PEC interface at $z = 0$. The resulting field for the $z > z'$ and $z < z'$ cases respectively is

$$\begin{aligned} E_y = E_y\left(x, y|x', y'\right) \tfrac{\partial}{\partial z} 2 \Bigg[& \left\{ \begin{array}{c} \cos\left[k_{z_\Gamma}\left(z - c_c\right)\right] e^{jk_{z_\Gamma}\left(z' - c_c\right)} \\ e^{jk_{z_\Gamma}\left(z - c_c\right)} \cos\left[k_{z_\Gamma}\left(z' - c_c\right)\right] \end{array} \right\} \\ & + A_{s2} \cos\left[k_{z_\Gamma}\left(z - c_c\right)\right] \cos\left[k_{z_\Gamma}\left(z' - c_c\right)\right] \Bigg] \end{aligned} \tag{B.66}$$

where applying the appropriate boundary condition determines the constant A_{s2} as

$$A_{s2} = -\frac{je^{-jk_{z_\Gamma} c_c}}{\sin\left(k_{z_\Gamma} c_c\right)} \tag{B.67}$$

Then, substitution of this constant back into (B.66) and then applying mathematical manipulation to the field for the $z > z'$ and $z < z'$ cases respectively, leads to

$$E_y = E_y\left(x, y|x', y'\right) \frac{\partial}{\partial z} \frac{2}{j \sin\left[k_{z_\Gamma} c_c\right]} \begin{bmatrix} \cos\left[k_{z_\Gamma}\left(z - c_c\right)\right] \cos\left(k_{z_\Gamma} z'\right) \\ \cos\left(k_{z_\Gamma} z\right) \cos\left[k_{z_\Gamma}\left(z' - c_c\right)\right] \end{bmatrix} \tag{B.68}$$

the representation of the y-directed component of the electric field for the rectangular cavity. Expanding this field, which is valid for all z and z', to include the x and y-dependencies and manipulating the expression to look like equation (B.60) gives

$$E_y = -j\omega\mu_0 \frac{\partial}{\partial z} \int_{S_a} dS \quad G_{CV}\left(\vec{r}|\vec{r}'\right) \frac{E_y\left(\vec{r}'\right)}{j\omega\mu_0} \tag{B.69}$$

where the rectangular cavity Green's function for the $z > z'$ and $z < z'$ cases respectively is

$$\begin{aligned} G_{CV}\left(\vec{r}|\vec{r}'\right) = \frac{-2}{a_c b_c} \sum_{\Gamma} \frac{\epsilon_\Gamma}{k_{z_\Gamma} \sin\left(k_{z_\Gamma} c_c\right)} & \sin\left[k_{x_\Gamma}\left(x - a_c/2\right)\right] \sin\left[k_{x_\Gamma}\left(x' - a_c/2\right)\right] \\ & \cdot \cos\left[k_{y_\Gamma}\left(y - b_c/2\right)\right] \cos\left[k_{y_\Gamma}\left(y' - b_c/2\right)\right] \\ & \begin{bmatrix} \cos\left[k_{z_\Gamma}\left(z - c_c\right)\right] \cos\left(k_{z_\Gamma} z'\right) \\ \cos\left(k_{z_\Gamma} z\right) \cos\left[k_{z_\Gamma}\left(z' - c_c\right)\right] \end{bmatrix} \end{aligned} \tag{B.70}$$

APPENDIX C

SOLUTIONS TO ADMITTANCE MATRIX ELEMENTS

Solutions to admittance matrix elements developed in Chapters 2 and 4 are detailed in Appendix C.

C.1 Waveguide Matrix Elements

The waveguide matrix elements only interact with one of the equivalent currents defined in the formulations. Therefore, they have only self terms defined as

$$l^{WG}_{m_1,n_1} = \int\limits_{x_{1n_1}-\frac{\Delta x_1}{2}}^{x_{1n_1}+\frac{\Delta x_1}{2}} dx'_1 K_{WG}\left(x_{1m_1},0|x'_1\right) \tag{C.1}$$

where the kernel is represented as

$$K_{WG}\left(x_{1m_1},0|x'_1\right) = \int\limits_{-W_1}^{W_1} dy'_1 \frac{f_1\left(y'_1\right)}{j\omega\mu_0} G_{WG}\left(x_{1m_1},0,t|x'_1,y'_1,t\right) \tag{C.2}$$

and the rectangular waveguide Green's function, due to a transverse slot cut in the bottom wall, from Appendix B is specialized as

$$\begin{aligned} G_{WG}\left(x_{1m_1},0,t|x'_1,y'_1,t\right) = {} & \frac{1}{ab}\sum_{\gamma}\frac{\epsilon_\gamma}{jk_{y\gamma}}\sin\left[k_{x\gamma}\left(x_{1m_1}-a/2\right)\right] \\ & \cdot \sin\left[k_{x\gamma}\left(x'_1-a/2\right)\right]e^{-jk_{y\gamma}\left|-y'_1\right|} \end{aligned} \tag{C.3}$$

Substitution of (C.2) and (C.3) into (C.1) and rearranging the terms leads to

$$l_{m,n}^{WG} = \frac{-1}{\omega\mu_0 ab}\sum_{\gamma}\frac{\epsilon_\gamma}{k_{y_\gamma}}\sin\left[k_{x_\gamma}\left(x_{1_{m_1}} - a/2\right)\right]\int_{-W_1}^{W_1} dy'_1 f_1\left(y'_1\right) e^{-jk_{y_\gamma}\left|-y'_1\right|} \cdot \int_{x_{1_{n_1}}-\frac{\Delta x_1}{2}}^{x_{1_{n_1}}+\frac{\Delta x_1}{2}} dx'_1 \sin\left[k_{x_\gamma}\left(x'_1 - a/2\right)\right] \quad \text{(C.4)}$$

where solving the spatial integrals gives the solution to the waveguide matrix elements. Solving the x'_1-dependent integral first, the addition theorem for sinusoidal functions is used to split the single integral into two closed form integrals. This is given as

$$\begin{aligned} l_{m,n}^{WG} = \frac{-1}{\omega\mu_0 ab}\sum_{\gamma}\frac{\epsilon_\gamma}{k_{y_\gamma}}\sin\left[k_{x_\gamma}\left(x_{1_{m_1}} - a/2\right)\right]\int_{-W_1}^{W_1} dy'_1 f_1\left(y'_1\right) e^{-jk_{y_\gamma}\left|-y'_1\right|} \\ \cdot \cos\left(k_{x_\gamma} a/2\right)\int_{x_{1_{n_1}}-\frac{\Delta x_1}{2}}^{x_{1_{n_1}}+\frac{\Delta x_1}{2}} dx'_1 \sin\left(k_{x_\gamma} x'_1\right) \\ - \sin\left(k_{x_\gamma} a/2\right)\int_{x_{1_{n_1}}-\frac{\Delta x_1}{2}}^{x_{1_{n_1}}+\frac{\Delta x_1}{2}} dx'_1 \cos\left(k_{x_\gamma} x'_1\right) \quad \text{(C.5)} \end{aligned}$$

where substitution of the solution for these closed form integrals leads to

$$\begin{aligned} l_{m,n}^{WG} = \frac{-1}{\omega\mu_0 ab}\sum_{\gamma}\frac{\epsilon_\gamma}{k_{y_\gamma}}\sin\left[k_{x_\gamma}\left(x_{1_{m_1}} - a/2\right)\right]\int_{-W_1}^{W_1} dy'_1 f_1\left(y'_1\right) e^{-jk_{y_\gamma}\left|-y'_1\right|} \\ \cdot \cos\left(k_{x_\gamma} a/2\right)\frac{2}{k_{x_\gamma}}\sin\left(k_{x_\gamma} x_{1_{n_1}}\right)\sin\left(k_{x_\gamma}\Delta x_1/2\right) \\ - \sin\left(k_{x_\gamma} a/2\right)\frac{2}{k_{x_\gamma}}\cos\left(k_{x_\gamma} x_{1_{n_1}}\right)\sin\left(k_{x_\gamma}\Delta x_1/2\right) \quad \text{(C.6)} \end{aligned}$$

Combining the similar sinusoidal terms and again using the addition theorem for sine functions, the matrix elements are written in terms of the only the y_1'-dependency as

$$l_{m,n}^{WG} = \frac{-2}{\omega\mu_0 ab}\sum_{\gamma}\frac{\epsilon_\gamma}{k_{x_\gamma}k_{y_\gamma}}\sin\left[k_{x_\gamma}\left(x_{1_{m_1}} - a/2\right)\right]\sin\left[k_{x_\gamma}\left(x_{1_{n_1}} - a/2\right)\right]$$
$$\cdot\sin\left(k_{x_\gamma}\Delta x_1/2\right)\int\limits_{-W_1}^{W_1} dy_1' f_1\left(y_1'\right)e^{-jk_{y_\gamma}\left|-y_1'\right|} \quad \text{(C.7)}$$

Now, to solve the y_1'-dependent integral, the y_1-directed distribution of the slot electric field from equation (2.49) is substituted, giving

$$l_{m,n}^{WG} = \frac{-1}{\omega\mu_0 abW_1}\sum_{\gamma}\frac{\epsilon_\gamma}{k_{x_\gamma}k_{y_\gamma}}\sin\left[k_{x_\gamma}\left(x_{1_{m_1}} - a/2\right)\right]\sin\left[k_{x_\gamma}\left(x_{1_{n_1}} - a/2\right)\right]$$
$$\cdot\sin\left(k_{x_\gamma}\Delta x_1/2\right)\int\limits_{-W_1}^{W_1} dy_1' e^{-jk_{y_\gamma}\left|-y_1'\right|} \quad \text{(C.8)}$$

Analysis of the exponential integral (making sure to handle the absolute value correctly) leads to the final solution for the waveguide matrix elements as

$$l_{m,n}^{WG} = \frac{-2j}{\omega\mu_0 abW_1}\sum_{\gamma}\frac{\epsilon_\gamma}{k_{x_\gamma}k_{y_\gamma}^2}\sin\left[k_{x_\gamma}\left(x_{1_{m_1}} - a/2\right)\right]\sin\left[k_{x_\gamma}\left(x_{1_{n_1}} - a/2\right)\right]$$
$$\cdot\sin\left(k_{x_\gamma}\Delta x_1/2\right)\left[e^{-jk_{y_\gamma}W_1} - 1\right] \quad for \quad \begin{cases} \alpha = 1, 2, 3, \ldots \\ \beta = 0, 1, 2, \ldots \end{cases} \quad \text{(C.9)}$$

C.2 Cavity Matrix Elements

The cavity matrix elements interact with two of the equivalent currents developed in the formulations of Chapters 2 and 4, thus having both self and coupled terms. The matrix elements are solved (observed) at either BS1 or BS2, where the self terms are excited by the equivalent current at the same interface, and the coupled terms are excited by the equivalent current at the opposite interface.

C.2.1 BS1 - Self Terms

The self term cavity matrix elements at BS1 are defined as

$$l_{m,n}^{CV11} = l_{m_1,n_1}^{CV11} = \int\limits_{x_{1_{n_1}}-\Delta x_1/2}^{x_{1_{n_1}}+\Delta x_1/2} dx_1' K_{CV11}\left(x_{1_{m_1}}, 0 | x_1'\right) \tag{C.10}$$

where the kernel is given as

$$K_{CV11}\left(x_{1_{m_1}}, 0 | x_1'\right) = \int\limits_{-W_1}^{W_1} dy_1' \frac{f_1\left(y_1'\right)}{j\omega\mu_0} G_{CV}\left(x_{1_{m_1}}, 0, t | x_1', y_1', t\right) \tag{C.11}$$

and the rectangular cavity Green's function is specialized as

$$\begin{aligned} G_{CV}\left(x_{1_{m_1}}, 0, t | x_1', y_1', t\right) = \frac{-2}{a_c b_c} \sum_{\Gamma} & \frac{\epsilon_\Gamma}{k_{z_\Gamma} \sin\left(k_{z_\Gamma} c_c\right)} \\ \cdot \sin\left[k_{x_\Gamma}\left(x_{1_{m_1}} - a_c/2\right)\right] & \sin\left[k_{x_\Gamma}\left(x_1' - a_c/2\right)\right] \\ \cdot \cos\left(k_{y_\Gamma} b_c/2\right) & \cos\left[k_{y_\Gamma}\left(y_1' - b_c/2\right)\right] \\ \cdot \cos\left[k_{z_\Gamma}\left(t - c_c\right)\right] & \cos\left(k_{z_\Gamma} t\right) \end{aligned} \tag{C.12}$$

Substitution of (C.11) and (C.12) into (C.10) and rearranging the solution gives

$$\begin{aligned} l^{CV11}_{m,n} = {} & \frac{j2}{\omega\mu_0 a_c b_c}\sum_{\Gamma}\frac{\epsilon_\Gamma \cos\left(k_{z_\Gamma} t\right)}{k_{z_\Gamma}\sin\left(k_{z_\Gamma} c_c\right)}\cos\left(k_{y_\Gamma} b_c/2\right) \\ & \cdot \sin\left[k_{x_\Gamma}\left(x_{1_{m_1}} - a_c/2\right)\right]\cos\left[k_{z_\Gamma}\left(t - c_c\right)\right] \\ & \cdot \int_{-W_1}^{W_1} dy_1' f_1\left(y_1'\right)\cos\left[k_{y_\Gamma}\left(y_1' - b_c/2\right)\right] \\ & \cdot \int_{x_{1_{n_1}}-\Delta x_1/2}^{x_{1_{n_1}}+\Delta x_1/2} dx_1' \sin\left[k_{x_\Gamma}\left(x_1' - a_c/2\right)\right] \end{aligned} \qquad \text{(C.13)}$$

Solving the x_1'-dependent integral first, it is noticed that the waveguide matrix elements had a similar x'-dependency, thus similar steps are taken to solve this integral. Therefore, the self cavity matrix elements at BS1 are written in terms of the only the y_1'-dependency as

$$\begin{aligned} l^{CV11}_{m,n} = {} & \frac{j4}{\omega\mu_0 a_c b_c}\sum_{\Gamma}\frac{\epsilon_\Gamma \cos\left(k_{z_\Gamma} t\right)}{k_{x_\gamma} k_{z_\Gamma}\sin\left(k_{z_\Gamma} c_c\right)}\cos\left[k_{z_\Gamma}\left(t - c_c\right)\right]\cos\left(k_{y_\Gamma} b_c/2\right) \\ & \cdot \sin\left(k_{x_\gamma}\Delta x_1/2\right)\sin\left[k_{x_\Gamma}\left(x_{1_{m_1}} - a_c/2\right)\right]\sin\left[k_{x_\Gamma}\left(x_{1_{n_1}} - a_c/2\right)\right] \\ & \cdot \int_{-W_1}^{W_1} dy_1' f_1\left(y_1'\right)\cos\left[k_{y_\Gamma}\left(y_1' - b_c/2\right)\right] \end{aligned} \qquad \text{(C.14)}$$

Again, similar to the waveguide matrix elements, solving the y_1'-dependent integral involves the substitution of the y_1-directed distribution of the slot electric field from equation (2.49) giving

$$\begin{aligned} l_{m,n}^{CV11} = \frac{j2}{\omega\mu_0 a_c b_c W_1} \sum_{\Gamma} \frac{\epsilon_\Gamma \cos\left(k_{z_\Gamma} t\right)}{k_{x_\gamma} k_{z_\Gamma} \sin\left(k_{z_\Gamma} c_c\right)} \cos\left[k_{z_\Gamma}\left(t - c_c\right)\right] \cos\left(k_{y_\Gamma} b_c/2\right) \\ \cdot \sin\left(k_{x_\gamma} \Delta x_1/2\right) \sin\left[k_{x_\Gamma}\left(x_{1_{m_1}} - a_c/2\right)\right] \sin\left[k_{x_\Gamma}\left(x_{1_{n_1}} - a_c/2\right)\right] \\ \cdot \int_{-W_1}^{W_1} dy_1' \cos\left[k_{y_\Gamma}\left(y_1' - b_c/2\right)\right] \end{aligned} \tag{C.15}$$

Then to solve the y_1'-dependent integral, the addition theorem for cosine is used to split the single integral into two closed form integrals. This is written as

$$\begin{aligned} l_{m,n}^{CV11} = \frac{j2}{\omega\mu_0 a_c b_c W_1} \sum_{\Gamma} \frac{\epsilon_\Gamma \cos\left(k_{z_\Gamma} t\right)}{k_{x_\gamma} k_{z_\Gamma} \sin\left(k_{z_\Gamma} c_c\right)} \cos\left[k_{z_\Gamma}\left(t - c_c\right)\right] \cos\left(k_{y_\Gamma} b_c/2\right) \\ \cdot \sin\left(k_{x_\gamma} \Delta x_1/2\right) \sin\left[k_{x_\Gamma}\left(x_{1_{m_1}} - a_c/2\right)\right] \sin\left[k_{x_\Gamma}\left(x_{1_{n_1}} - a_c/2\right)\right] \\ \cdot \cos\left(k_{y_\Gamma} b_c/2\right) \int_{-W_1}^{W_1} dy_1' \cos\left(k_{y_\Gamma} y_1'\right) \\ \cdot - \sin\left(k_{y_\Gamma} b_c/2\right) \int_{-W_1}^{W_1} dy_1' \sin\left(k_{y_\Gamma} y_1'\right) \end{aligned} \tag{C.16}$$

where it is seen by inspection that using the concept of even/odd integrals over symmetric limits, leads to

$$\begin{aligned} l_{m,n}^{CV11} = \frac{j4}{\omega\mu_0 a_c b_c W_1} \sum_{\Gamma} \frac{\epsilon_\Gamma \cos\left(k_{z_\Gamma} t\right)}{k_{x_\gamma} k_{z_\Gamma} \sin\left(k_{z_\Gamma} c_c\right)} \cos\left[k_{z_\Gamma}\left(t - c_c\right)\right] \cos^2\left(k_{y_\Gamma} b_c/2\right) \\ \cdot \sin\left(k_{x_\gamma} \Delta x_1/2\right) \sin\left[k_{x_\Gamma}\left(x_{1_{m_1}} - a_c/2\right)\right] \sin\left[k_{x_\Gamma}\left(x_{1_{n_1}} - a_c/2\right)\right] \\ \cdot \int_{0}^{W_1} dy_1' \cos\left(k_{y_\Gamma} y_1'\right) \end{aligned} \tag{C.17}$$

Solving this cosine integral leads to the final form of the self cavity matrix elements at BS1, with unspecified dimensions

$$
\begin{aligned}
l^{CV11}_{m,n} = \frac{j4}{\omega\mu_0 a_c b_c W_1} \sum_{\Gamma} \frac{\epsilon_\Gamma \cos\left(k_{z_\Gamma} t\right)}{k_{x_\gamma} k_{y_\Gamma} k_{z_\Gamma} \sin\left(k_{z_\Gamma} c_c\right)} \cos\left[k_{z_\Gamma}\left(t - c_c\right)\right] \\
\cdot \sin\left(k_{x_\gamma} \Delta x_1/2\right) \sin\left[k_{x_\Gamma}\left(x_{1_{m_1}} - a_c/2\right)\right] \sin\left[k_{x_\Gamma}\left(x_{1_{n_1}} - a_c/2\right)\right] \\
\cdot \cos^2\left(k_{y_\Gamma} b_c/2\right) \sin\left(k_{y_\Gamma} W_1\right) \qquad \text{(C.18)}
\end{aligned}
$$

Applying the specific cavity dimensions used in the formulations of Chapters 2 and 4, given as

$$
a_c = 2L \quad ; \quad b_c = 2W \quad ; \quad c_c = t \quad ; \quad W_1 = W \qquad \text{(C.19)}
$$

the self cavity matrix elements at BS1 are finally written as

$$
\begin{aligned}
l^{CV11}_{m_1,n_1} = \frac{j}{\omega\mu_0 L W^2} \sum_{\Gamma} \frac{\epsilon_\Gamma}{k_{x_\gamma} k_{y_\Gamma} k_{z_\Gamma}} \sin\left(k_{x_\gamma} \Delta x_1/2\right) \\
\cdot \sin\left[k_{x_\Gamma}\left(x_{1_{m_1}} - L\right)\right] \sin\left[k_{x_\Gamma}\left(x_{1_{n_1}} - L\right)\right] \\
\cdot \cos^2\left(k_{y_\Gamma} W\right) \sin\left(k_{y_\Gamma} W\right) \cot\left(k_{z_\Gamma} t\right) \qquad \text{(C.20)}
\end{aligned}
$$

C.2.2 BS1 - Coupled Terms

The coupled term cavity matrix elements at BS1 are defined as

$$
l^{CV12}_{m,n} = l^{CV12}_{m_1,n_2} = \int_{x_{2_{n_2}} - \Delta x_2/2}^{x_{2_{n_2}} + \Delta x_2/2} dx_2' K_{CV12}\left(x_{1_{m_1}}, 0 | x_2'\right) \qquad \text{(C.21)}
$$

where the kernel is given as

$$
K_{CV12}\left(x_{1_{m_1}}, 0 | x_2'\right) = \int_{-W_2}^{W_2} dy_2' \frac{f_2\left(y_2'\right)}{j\omega\mu_0} G_{CV}\left(x_{1_{m_1}}, 0, t | x_2', y_2', 0\right) \qquad \text{(C.22)}
$$

and the rectangular cavity Green's function is specialized as

$$\begin{aligned} G_{CV}\left(x_{1_{m_1}}, 0, t | x_2', y_2', 0\right) &= \frac{-2}{a_c b_c} \sum_{\Gamma} \frac{\epsilon_{\Gamma}}{k_{z_{\Gamma}} \sin\left(k_{z_{\Gamma}} c_c\right)} \\ \cdot \sin\left[k_{x_{\Gamma}}\left(x_{1_{m_1}} - a_c/2\right)\right] &\sin\left[k_{x_{\Gamma}}\left(x_2' - a_c/2\right)\right] \\ \cdot \cos\left(k_{y_{\Gamma}} b_c/2\right) \cos\left[k_{y_{\Gamma}}\left(y_2' - b_c/2\right)\right] &\cos\left[k_{z_{\Gamma}}\left(t - c_c\right)\right] \end{aligned} \quad (C.23)$$

Substitution of (C.22) and (C.23) into (C.21) and rearranging the solution gives

$$\begin{aligned} l_{m,n}^{CV12} = \frac{j2}{\omega \mu_0 a_c b_c} &\sum_{\Gamma} \frac{\epsilon_{\Gamma}}{k_{z_{\Gamma}} \sin\left(k_{z_{\Gamma}} c_c\right)} \cos\left(k_{y_{\Gamma}} b_c/2\right) \\ &\cdot \sin\left[k_{x_{\Gamma}}\left(x_{1_{m_1}} - a_c/2\right)\right] \cos\left[k_{z_{\Gamma}}\left(t - c_c\right)\right] \\ &\cdot \int_{-W_2}^{W_2} dy_2' f_2\left(y_2'\right) \cos\left[k_{y_{\Gamma}}\left(y_2' - b_c/2\right)\right] \\ &\cdot \int_{x_{2_{n_2}} - \Delta x_2/2}^{x_{2_{n_2}} + \Delta x_2/2} dx_2' \sin\left[k_{x_{\Gamma}}\left(x_2' - a_c/2\right)\right] \end{aligned} \quad (C.24)$$

Solving the spatial integrals in a similar manner as the self terms at BS1 and then applying the following cavity dimensions

$$a_c = 2L \quad ; \quad b_c = 2W \quad ; \quad c_c = t \quad (C.25)$$

the final solution for the coupled terms of the cavity matrix elements at BS1 is

$$\begin{aligned} l_{m,n}^{CV12} = \frac{j}{\omega \mu_0 L W W_2} &\sum_{\Gamma} \frac{\epsilon_{\Gamma}}{k_{x_{\gamma}} k_{y_{\Gamma}} k_{z_{\Gamma}} \sin\left(k_{z_{\Gamma}} t\right)} \\ \cdot \sin\left(k_{x_{\gamma}} \Delta x_2/2\right) \sin\left[k_{x_{\Gamma}}\left(x_{1_{m_1}} - L\right)\right] &\sin\left[k_{x_{\Gamma}}\left(x_{2_{n_2}} - L\right)\right] \\ &\cdot \cos^2\left(k_{y_{\Gamma}} W\right) \sin\left(k_{y_{\Gamma}} W_2\right) \end{aligned} \quad (C.26)$$

C.2.3 BS2 - Self Terms

Similarly, the self term cavity matrix elements at BS2 are defined as

$$l_{m,n}^{CV22} = l_{m_2,n_2}^{CV22} = \int\limits_{x_{2n_2}-\Delta x_2/2}^{x_{2n_2}+\Delta x_2/2} dx_2' K_{CV22}\left(x_{2m_2}, 0 | x_2'\right) \tag{C.27}$$

where the kernel is given as

$$K_{CV22}\left(x_{2m_2}, 0 | x_2'\right) = \int\limits_{-W_2}^{W_2} dy_2' \frac{f_2\left(y_2'\right)}{j\omega\mu_0} G_{CV}\left(x_{2m_2}, 0, 0 | x_2', y_2', 0\right) \tag{C.28}$$

and the rectangular cavity Green's function is specialized as

$$\begin{aligned} G_{CV}\left(x_{2m_2}, 0, 0 | x_2', y_2', 0\right) &= \frac{-2}{a_c b_c} \sum_{\Gamma} \frac{\epsilon_\Gamma}{k_{z\Gamma} \sin\left(k_{z\Gamma} c_c\right)} \\ &\cdot \sin\left[k_{x\Gamma}\left(x_{2m_2} - a_c/2\right)\right] \sin\left[k_{x\Gamma}\left(x_2' - a_c/2\right)\right] \\ &\cdot \cos\left(k_{y\Gamma} b_c/2\right) \cos\left[k_{y\Gamma}\left(y_2' - b_c/2\right)\right] \cos\left(k_{z\Gamma} c_c\right) \end{aligned} \tag{C.29}$$

Substitution of (C.28) and (C.29) into (C.27) and rearranging the solution gives

$$\begin{aligned} l_{m,n}^{CV22} = \frac{j2}{\omega\mu_0 a_c b_c} \sum_{\Gamma} &\frac{\epsilon_\Gamma \cos\left(k_{z\Gamma} c_c\right)}{k_{z\Gamma} \sin\left(k_{z\Gamma} c_c\right)} \cos\left(k_{y\Gamma} b_c/2\right) \\ &\cdot \sin\left[k_{x\Gamma}\left(x_{2m_2} - a_c/2\right)\right] \\ &\cdot \int\limits_{-W_2}^{W_2} dy_2' f_2\left(y_2'\right) \cos\left[k_{y\Gamma}\left(y_2' - b_c/2\right)\right] \\ &\cdot \int\limits_{x_{2n_2}-\Delta x_2/2}^{x_{2n_2}+\Delta x_2/2} dx_2' \sin\left[k_{x\Gamma}\left(x_2' - a_c/2\right)\right] \end{aligned} \tag{C.30}$$

where solving the spatial integrals in a similar manner as the self terms at BS1 and then applying the following cavity dimensions

$$a_c = 2L \quad ; \quad b_c = 2W \quad ; \quad c_c = t \tag{C.31}$$

the final solution for the self terms of the cavity matrix elements at BS2 is

$$\begin{aligned} l_{m,n}^{CV22} = \frac{j}{\omega\mu_0 L W W_2} \sum_{\Gamma} \frac{\epsilon_\Gamma \cos\left(k_{z_\Gamma} t\right)}{k_{x_\gamma} k_{y_\Gamma} k_{z_\Gamma} \sin\left(k_{z_\Gamma} t\right)} \\ \cdot \sin\left(k_{x_\gamma} \Delta x_2/2\right) \sin\left[k_{x_\Gamma}\left(x_{2_{m_2}} - L\right)\right] \sin\left[k_{x_\Gamma}\left(x_{2_{n_2}} - L\right)\right] \\ \cdot \cos^2\left(k_{y_\Gamma} W\right) \sin\left(k_{y_\Gamma} W_2\right) \end{aligned} \tag{C.32}$$

C.2.4 BS2 - Coupled Terms

Finally, the coupled term cavity matrix elements at BS2 are defined as

$$l_{m,n}^{CV21} = l_{m_2,n_1}^{CV21} = \int\limits_{x_{1_{n_1}} - \Delta x_1/2}^{x_{1_{n_1}} + \Delta x_1/2} dx_1' K_{CV21}\left(x_{2_{m_2}}, 0 | x_1'\right) \tag{C.33}$$

where the kernel is given as

$$K_{CV21}\left(x_{2_{m_2}}, 0 | x_1'\right) = \int\limits_{-W_1}^{W_1} dy_1' \frac{f_1\left(y_1'\right)}{j\omega\mu_0} G_{CV}\left(x_{2_{m_2}}, 0, 0 | x_1', y_1', t\right) \tag{C.34}$$

and the rectangular cavity Green's function is specialized as

$$\begin{aligned} G_{CV}\left(x_{2_{m_2}}, 0, 0 | x_1', y_1', t\right) = \frac{-2}{a_c b_c} \sum_{\Gamma} \frac{\epsilon_\Gamma}{k_{z_\Gamma} \sin\left(k_{z_\Gamma} c_c\right)} \\ \cdot \sin\left[k_{x_\Gamma}\left(x_{2_{m_2}} - a_c/2\right)\right] \sin\left[k_{x_\Gamma}\left(x_1' - a_c/2\right)\right] \\ \cdot \cos\left(k_{y_\Gamma} b_c/2\right) \cos\left[k_{y_\Gamma}\left(y_1' - b_c/2\right)\right] \cos\left[k_{z_\Gamma}\left(t - c_c\right)\right] \end{aligned} \tag{C.35}$$

Substitution of (C.34) and (C.35) into (C.33) and rearranging the solution gives

$$\begin{aligned} l^{CV21}_{m,n} &= \frac{j2}{\omega\mu_0 a_c b_c} \sum_{\Gamma} \frac{\epsilon_\Gamma}{k_{z_\Gamma} \sin\left(k_{z_\Gamma} c_c\right)} \cos\left(k_{y_\Gamma} b_c/2\right) \\ &\cdot \sin\left[k_{x_\Gamma}\left(x_{2_{m_2}} - a_c/2\right)\right] \cos\left[k_{z_\Gamma}\left(t - c_c\right)\right] \\ &\cdot \int_{-W_1}^{W_1} dy_1' f_1\left(y_1'\right) \cos\left[k_{y_\Gamma}\left(y_1' - b_c/2\right)\right] \int_{x_{1_{n_1}}-\Delta x_1/2}^{x_{1_{n_1}}+\Delta x_1/2} dx_1' \sin\left[k_{x_\Gamma}\left(x_1' - a_c/2\right)\right] \end{aligned} \tag{C.36}$$

Again, solving the spatial integrals in a similar manner as the self terms at BS1 and then applying the following cavity dimensions

$$a_c = 2L \quad ; \quad b_c = 2W \quad ; \quad c_c = t \quad ; \quad W_1 = W \tag{C.37}$$

the final solution for the coupled terms of the cavity matrix elements at BS2 is

$$\begin{aligned} l^{CV21}_{m,n} &= \frac{j}{\omega\mu_0 L W^2} \sum_{\Gamma} \frac{\epsilon_\Gamma}{k_{x_\gamma} k_{y_\Gamma} k_{z_\Gamma} \sin\left(k_{z_\Gamma} t\right)} \\ &\cdot \sin\left(k_{x_\gamma}\Delta x_1/2\right) \sin\left[k_{x_\Gamma}\left(x_{2_{m_2}} - L\right)\right] \sin\left[k_{x_\Gamma}\left(x_{1_{n_1}} - L\right)\right] \\ &\cdot \cos^2\left(k_{y_\Gamma} W\right) \sin\left(k_{y_\Gamma} W\right) \end{aligned} \tag{C.38}$$

C.3 Halfspace Matrix Elements

The halfspace matrix elements only interact with the equivalent current defined at BS2 in the formulation of Chapter 2. Therefore, they have only self terms defined as

$$l^{HS}_{m_2,n_2} = \int_{x_{2_{n_2}}-\frac{\Delta x_2}{2}}^{x_{2_{n_2}}+\frac{\Delta x_2}{2}} dx_2' K_{HS}\left(x_{2_{m_2}}, 0 | x_2'\right) \tag{C.39}$$

where the kernel is given as

$$K_{HS}\left(x_{2_{m_2}},0|x_2'\right) = \int_{-W_2}^{W_2} dy_2' \frac{f_2\left(y_2'\right)}{j\omega\mu_0} G_{HS}\left(x_{2_{m_2}},0,0|x_2',y_2',0\right) \tag{C.40}$$

and the halfspace Green's function is specialized as

$$G_{HS}\left(x_{2_{m_2}},0,0|x_2',y_2',0\right) = \frac{e^{-jk_0\sqrt{\left(x_{2_{m_2}}-x_2'\right)^2+\left(-y_2'\right)^2}}}{2\pi\sqrt{\left(x_{2_{m_2}}-x_2'\right)^2+\left(-y_2'\right)^2}} \tag{C.41}$$

Substitution of (C.40) and (C.41) into (C.39) and rearranging the solution gives

$$l_{m,n}^{HS} = \frac{-j}{\omega\mu_0 4\pi W_2} \int_{x_{2_{n_2}}-\frac{\Delta x_2}{2}}^{x_{2_{n_2}}+\frac{\Delta x_2}{2}} dx_2' \int_{-W_2}^{W_2} dy_2' \frac{e^{-jk_0\sqrt{\left(x_{2_{m_2}}-x_2'\right)^2+\left(y_2'\right)^2}}}{\sqrt{\left(x_{2_{m_2}}-x_2'\right)^2+\left(y_2'\right)^2}} \tag{C.42}$$

where depending on whether or not m_2 equals n_2, the solution of the spatial integrals are approximated differently, leading to the final solution for the halfspace matrix elements.

C.3.1 $m_2 \neq n_2$

For the $m_2 \neq n_2$ case, the source points are approximated as follows

$$x_2' \rightarrow x_{2_{n_2}}; \quad y_2' \rightarrow 0 \tag{C.43}$$

which is essentially a point excitation at the center of each partition, leading to the distance between source and observer as

$$R_{m\neq n} = \sqrt{\left(x_{2_{m_2}} - x_{2_{n_2}}\right)^2} = \left|x_{2_{m_2}} - x_{2_{n_2}}\right| \tag{C.44}$$

This approximation is valid since the dimensions of the slot are long and narrow relative to the wavelength, where by the distance between separate partitions will vary insignificantly for any point in either partition. Substitution of (C.44) into (C.42) and then rearranging the solution gives

$$l_{m,n}^{HS} = \frac{-j}{\omega\mu_0 4\pi W_2} \frac{e^{-jk_0\left|x_{2m_2}-x_{2n_2}\right|}}{\left|x_{2m_2} - x_{2n_2}\right|} \int\limits_{x_{2n_2}-\frac{\Delta x_2}{2}}^{x_{2n_2}+\frac{\Delta x_2}{2}} dx_2' \int\limits_{-W_2}^{W_2} dy_2' \tag{C.45}$$

which, after solving the spatial integrals, leads to the final form of the halfspace matrix elements for $m_2 \neq n_2$ as

$$l_{m,n}^{HS} = \frac{-j\Delta x_2 e^{-jk_0\left|x_{2m_2}-x_{2n_2}\right|}}{\omega\mu_0 2\pi \left|x_{2m_2} - x_{2n_2}\right|} \tag{C.46}$$

C.3.2 $m_2 = n_2$

For the $m_2 = n_2$ case, the source points are approximated as follows

$$x_2' \rightarrow x_{2n_2}; \;\; y_2' \rightarrow 0; \;\; x_{2m_2} = x_{2n_2} \tag{C.47}$$

where, since the source and observer locations are at essentially the same point, the distance between them is approximately

$$R_{m_2=n_2} \approxeq 0 \tag{C.48}$$

Substitution of (C.48) into (C.42) leads to the following

$$l_{m,n}^{HS} = \frac{-j}{\omega\mu_0 4\pi W_2} \int_{x_{2n_2}-\frac{\Delta x_2}{2}}^{x_{2n_2}+\frac{\Delta x_2}{2}} dx_2' \int_{-W_2}^{W_2} dy_2' \frac{1}{\sqrt{\left(x_{2n_2} - x_2'\right)^2 + \left(y_2'\right)^2}} \tag{C.49}$$

where the $R_{m_2=n_2}$ in the denominator is not substituted, since this would lead to an indeterminate form of the equation, and thus a bad approximation. Instead, a change of variables given as

$$x_{2n_2} - x_2' = u; \quad dx_2' = -du \tag{C.50}$$

is applied to (C.49) to simplify the analysis of the spatial integrals, leading to

$$l_{m,n}^{HS} = \frac{-j}{\omega\mu_0 4\pi W_2} \int_{-\frac{\Delta x_2}{2}}^{\frac{\Delta x_2}{2}} du \int_{-W_2}^{W_2} dy_2' \frac{1}{\sqrt{u^2 + y_2'^2}} \tag{C.51}$$

Now the use of a change of variables ($u = x'$) along with the concept of an even function integrated over symmetric limits gives the solution as

$$l_{m,n}^{HS} = \frac{-j}{\omega\mu_0 2\pi W_2} \int_{-\frac{\Delta x_2}{2}}^{\frac{\Delta x_2}{2}} dx_2' \int_{0}^{W_2} dy_2' \frac{1}{\sqrt{x_2'^2 + y_2'^2}} \tag{C.52}$$

The integral over the y_2'-dependent function was found in an integral table [71] as

$$\int \frac{dx}{\sqrt{R}} = \frac{1}{\sqrt{c}} \sinh^{-1}\left(\frac{2cx + b}{\sqrt{4ac - b^2}}\right) \quad ; \quad R = a + bx + cx^2 \tag{C.53}$$

where

$$x = y_2'; \quad a = x_2'^2; \quad b = 0; \quad c = 1 \tag{C.54}$$

specializes (C.53) to the integral in (C.52). Substituting the solution to (C.53) into (C.52) leads to

$$l_{m,n}^{HS} = \frac{-j}{\omega\mu_0 2\pi W_2} \int_{-\frac{\Delta x_2}{2}}^{\frac{\Delta x_2}{2}} dx_2' \sinh^{-1}\left(\frac{W_2}{x_2'}\right) \tag{C.55}$$

where the simple trigonometric relationship

$$\sinh^{-1}(x) = \csc h^{-1}\left(\frac{1}{x}\right) \tag{C.56}$$

allows (C.55) to be written as

$$l_{m,n}^{HS} = \frac{-j}{\omega\mu_0 2\pi W_2} \int_{-\frac{\Delta x_2}{2}}^{\frac{\Delta x_2}{2}} dx_2' \csc h^{-1}\left(\frac{x_2'}{W_2}\right) \tag{C.57}$$

The integral over the x_2'-dependent function was also found in an integral table [71] as

$$\int dx \csc h^{-1}\left(\frac{x}{a}\right) = x \csc h^{-1}\left(\frac{x}{a}\right) + a \sinh^{-1}\left(\frac{x}{a}\right) \tag{C.58}$$

where

$$x = x_2'; \quad a = W_2 \tag{C.59}$$

specializes (C.58) to the integral in (C.57). Solving this integral, substituting the solution back into (C.57), and then using simple mathematical manipulations, the final solution for the halfspace matrix elements when $m_2 = n_2$ is

$$l_{m,n}^{HS} = \frac{-j}{\omega\mu_0 \pi W_2}\left[\frac{\Delta x_2}{2} \sinh^{-1}\left(\frac{2W_2}{\Delta x_2}\right) + W_2 \sinh^{-1}\left(\frac{\Delta x_2}{2W_2}\right)\right] \tag{C.60}$$

C.4 Parallel-plate Matrix Elements

The parallel-plate matrix elements only interact with the equivalent current defined at BS2 in the formulation of Chapter 4. Therefore, they have only self terms defined as

$$l^{PP3}_{m_2,n_2} = \int\limits_{x_{2n_2}-\Delta x_2/2}^{x_{2n_2}+\Delta x_2/2} dx_2' K_{PP3}\left(x_{2m_2},0|x_2'\right) \tag{C.61}$$

where the kernel is given as

$$K_{PP3}\left(x_{2m_2},0|x_2'\right) = \int\limits_{-W_2}^{W_2} dy_2' \frac{f_2\left(y_2'\right)}{j\omega\mu} G_{PP3}\left(x_{2m_2},0,0|x_2',y_2',0\right) \tag{C.62}$$

and the parallel-plate Green's function from Chapter 3 is specialized as

$$G_{PP3}\left(x_{2m_2},0,0|x_2',y_2',0\right) = \int\limits_{-\infty}^{\infty}\int\limits_{-\infty}^{\infty} d^2\lambda \frac{e^{j\xi\left(x_{2m_2}-x_2'\right)} e^{-j\eta y_2'} \cosh\left(pd\right)\left(\xi^2-k^2\right)}{\left(2\pi\right)^2 p \sinh\left(pd\right)\left(\xi^2-k_0^2\right)} \tag{C.63}$$

Substitution of (C.62) and (C.63) into (C.61) and then rearranging the solution leads to

$$\begin{aligned} l^{PP3}_{m,n} = \frac{-j}{\omega\mu 4\pi^2} &\int\limits_{-\infty}^{\infty}\int\limits_{-\infty}^{\infty} d^2\lambda \frac{e^{j\xi x_{2m_2}} \cosh\left(pd\right)\left(\xi^2-k^2\right)}{p\sinh\left(pd\right)\left(\xi^2-k_0^2\right)} \\ &\cdot \int\limits_{-W_2}^{W_2} dy_2' f_2\left(y_2'\right) e^{-j\eta y_2'} \int\limits_{x_{2n_2}-\Delta x_2/2}^{x_{2n_2}+\Delta x_2/2} dx_2' e^{-j\xi x_2'} \end{aligned} \tag{C.64}$$

where the solution is in terms of both spatial and spectral integrals. Solving the x_2'-dependent spatial integral first leads to

$$l_{m,n}^{PP3} = \frac{-j}{\omega\mu 2\pi^2} \int_{-\infty}^{\infty} \int_{-\infty}^{\infty} d^2\lambda \frac{e^{j\xi\left(x_{2_{m_2}} - x_{2_{n_2}}\right)} \sin\left(\xi \Delta x_2/2\right) \cosh\left(pd\right) \left(\xi^2 - k^2\right)}{\xi p \sinh\left(pd\right) \left(\xi^2 - k_0^2\right)} \cdot \int_{-W_2}^{W_2} dy_2' f_2\left(y_2'\right) e^{-j\eta y_2'} \tag{C.65}$$

Next, the y_2'-dependent spatial integral is solved after substituting the y_2-directed distribution of the slot electric field from equation 2.49, yielding

$$l_{m,n}^{PP3} = \frac{-j}{\omega\mu 2\pi^2 W_2} \int_{-\infty}^{\infty} \int_{-\infty}^{\infty} d^2\lambda \frac{\sin\left(\eta W_2\right) e^{j\xi\left(x_{2_{m_2}} - x_{2_{n_2}}\right)} \sin\left(\xi \Delta x_2/2\right) \cosh\left(pd\right) \left(\xi^2 - k^2\right)}{\eta \xi p \sinh\left(pd\right) \left(\xi^2 - k_0^2\right)} \tag{C.66}$$

the solution in terms of only spectral integrals.

C.4.1 Spectral Integral Analysis

The use of the Fourier transform domain method in Chapter 3, to solve for the parallel-plate Green's function, lead to the spectral integrals in equation (C.63). Solving the spatial integrals in equation (C.64) has then given the solution to the parallel-plate matrix elements in terms of only the spectral integrals in equation (C.66). Solving these spectral integrals will produce the desired solution for the parallel-plate admittance matrix elements in Chapter 4.

Cauchy's integral theorem, integral formula and residue theorem, are used to solve the spectral integrals in equation (C.66). Cauchy's integral theorem states that if a function $f(z)$ is analytic at all points interior to and on a simple closed contour C

[64], then

$$\oint_C f(z)dz = 0 \tag{C.67}$$

Cauchy's integral formula states that if $f(z)$ is analytic everywhere within and on a simple closed contour C, then if z_0 is any point interior to C

$$\oint_C \frac{f(z)}{z - z_0}dz = \pm 2\pi j f(z_0) \tag{C.68}$$

depending on whether C is oriented in the positive or negative direction. Cauchy's residue theorem states that if $f(z)$ is analytic on the closed contour C, then the value of the integral of $f(z)$ around C is

$$\oint_C f(z)dz = \pm 2\pi j \sum_{k=1}^{n} Res_{z=z_k} f(z) \tag{C.69}$$

C.4.1.1 η Analysis

Rearranging equation (C.66) so that all the η dependent terms are separated and then re-writing the sinusoidal η component in exponential form leads to the following form of the solution

$$\begin{aligned} I_{m,n}^{PP3} = \frac{-1}{\omega\mu 4\pi^2 W_2} \int_{-\infty}^{\infty} d\xi \frac{e^{j\xi\left(x_{2_{m_2}} - x_{2_{n_2}}\right)} \sin\left(\xi\Delta x_2/2\right)\left(\xi^2 - k^2\right)}{\xi\left(\xi^2 - k_0^2\right)} \\ \cdot \int_{-\infty}^{\infty} d\eta \frac{\left(e^{j\eta W_2} - e^{-j\eta W_2}\right)\cosh\left(pd\right)}{\eta p \sinh\left(pd\right)} \end{aligned} \tag{C.70}$$

Since only the η spectral integral is of interest in this section, a separate ξ-dependent function is defined as follows

$$F(\xi) = \int_{-\infty}^{\infty} d\eta \frac{\left(e^{j\eta W_2} - e^{-j\eta W_2}\right)\cosh(pd)}{\eta p \sinh(pd)} \tag{C.71}$$

The parameter $p = p(\eta, \xi)$ is a function of η, thus the solution written in terms of η is

$$F(\xi) = \int_{-\infty}^{\infty} d\eta \frac{\left(e^{j\eta W_2} - e^{-j\eta W_2}\right)\cosh\left(\sqrt{\eta^2 - \eta_0^2}d\right)}{\eta\sqrt{\eta^2 - \eta_0^2}\sinh\left(\sqrt{\eta^2 - \eta_0^2}d\right)} \tag{C.72}$$

where

$$\eta_0^2 = p^2 + k^2 - \xi^2 \tag{C.73}$$

Equation (C.71) now reveals the singularities in the complex η-plane, where at first glance there appears to be both simple poles (ie. $\eta = 0$) and branch cuts (ie. $p.\sinh(pd) = 0$). However, upon further evaluation the apparent branch cuts actually reduce to simple poles, the key to this important reduction is the small argument approximation for the sine function ($\sin(x) \approxeq x$ for $x << 1$). This is because no matter what value of p makes $\sinh(pd) = 0$, there is always ends up being a p^2 in the denominator which gives simple poles at $\eta = \pm\eta_0$.

By allowing η to be complex (ie. $\eta = \eta_{re} + j\eta_{im}$), the integrand in equation (C.71) becomes analytic in the entire complex η-plane, except at the simple pole singularities stated earlier. This allows Cauchy's integral theorem to be invoked by deforming the integration contour off the real axis, where the specific closed contour C is chosen based on an examination of the integrand. More specifically, the exponential terms $e^{\pm j\eta W_2}$ are considered since proper choice of the half-plane closure provides exponential decay and thus convergence of the integral. Splitting the integrand into two terms as follows

$$F(\xi) = \int\limits_{-\infty}^{\infty} d\eta \frac{e^{j\eta W_2}\cosh(pd)}{\eta p \sinh(pd)} - \int\limits_{-\infty}^{\infty} d\eta \frac{e^{-j\eta W_2}\cosh(pd)}{\eta p \sinh(pd)} \tag{C.74}$$

allows the ξ-dependent function to be defined as

$$F(\xi) = F^{UHP}(\xi) + F^{LHP}(\xi) \tag{C.75}$$

where UHP and LHP describe the half-plane closure used to ensure convergence of the integrand.

Figure C.1 shows the closed contour for the integrand of $F^{UHP}(\xi)$, where applying Cauchy's integral theorem leads to

$$\begin{aligned} F^{UHP}(\xi) = \oint_C F^{UHP}(\xi,\eta)\, d\eta = \int_{C_R + C_0^+ + C_\infty^+} F^{UHP}(\xi,\eta)\, d\eta \\ = 2\pi j \sum_i Res_i\left(F^{UHP}(\xi,\eta)\right) \end{aligned} \tag{C.76}$$

The infinite contour integral is examined, via inspection, by letting η tend to infinity. The hyperbolic sinusoidal terms are seen to cancel each other and the p term tends to η, giving

$$\int_{C_\infty^+} F^{UHP}(\xi,\eta)\, d\eta = \int_{C_\infty^+} d\eta \frac{e^{j\eta W_2}}{\eta^2} = 0 \tag{C.77}$$

where since η is complex and proper half-plane closure was chosen, the exponential term decays, driving the value of the integral to zero.

The contour integral around the pole at $\eta = 0$ is examined using Cauchy's residue theorem. The semi-circle arc has a negative orientation to ensure the desired integral has the proper sign. Since the arc in only half a circle, the residue is only multiplied

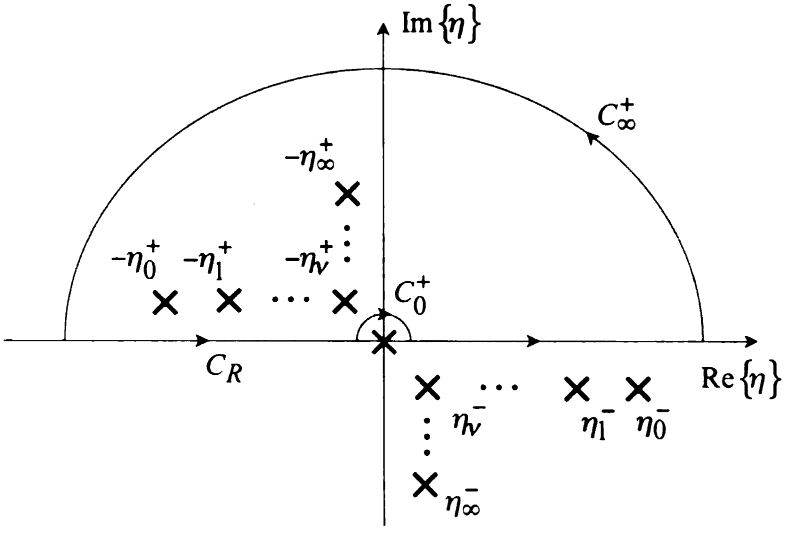

Figure C.1. Evaluation contour for UHP closure in the complex η-plane

by $-\pi j$ instead of $-2\pi j$, leading to

$$\int_{C_0^+} F^{UHP}(\xi,\eta)\,d\eta = -\pi j\left[Res\left(F^{UHP}(\xi,0)\right)\right] \tag{C.78}$$

where the residue is

$$Res\left(F^{UHP}(\xi,0)\right) = \frac{p_0^{UHP}(\eta=0)}{q_0'^{UHP}(\eta=0)} = \frac{\cosh(p_0 d)}{p_0\sinh(p_0 d)} \tag{C.79}$$

Substituting the results for (C.77) and (C.79) into (C.76) and rearranging the function to achieve the desired result in terms of the remaining residues, gives

$$\oint_C F^{UHP}(\xi,\eta)\,d\eta = \pi j\left[\frac{\cosh(p_0 d)}{p_0\sinh(p_0 d)}\right]$$
$$+2\pi j\left[Res\left(F^{UHP}(\xi,-\eta_0)\right) + \sum_{\nu=1}^{\infty} Res\left(F^{UHP}(\xi,-\eta_\nu)\right)\right] \tag{C.80}$$

where the remaining residues have full circle arcs orientated in the positive direction, thus they are multiplied by $2\pi j$ and are found as

$$Res\left(F^{UHP}(\xi, -\eta_0)\right) = \frac{p^{UHP}_{-\eta_0}(\eta = -\eta_0)}{q'^{UHP}_{-\eta_0}(\eta = -\eta_0)} = \frac{e^{-j\eta_0 W_2}}{\eta_0^2 2d} \tag{C.81}$$

and

$$Res\left(F^{UHP}(\xi, -\eta_\nu)\right) = \frac{p^{UHP}_{-\eta_\nu}(\eta = -\eta_\nu)}{q'^{UHP}_{-\eta_\nu}(\eta = -\eta_\nu)} = \frac{e^{-j\eta_\nu W_2}}{\eta_\nu^2 d} \tag{C.82}$$

respectively. Substituting (C.81) and (C.82) into (C.80) yields the final desired result as

$$F^{UHP}(\xi) = \pi j\left[\frac{\cosh(p_0 d)}{p_0 \sinh(p_0 d)} + \frac{e^{-j\eta_0 W_2}}{\eta_0^2 d} + \sum_{\nu=1}^{\infty} \frac{2e^{-j\eta_\nu W_2}}{\eta_\nu^2 d}\right] \tag{C.83}$$

where the various spectral wavenumbers are given as

$$\eta_\nu^2 = p_\nu^2 + k^2 - \xi^2 \quad ; \quad p_\nu = \frac{j\nu\pi}{d} \quad ; \quad \eta_0^2 = k^2 - \xi^2 \quad ; \quad p_0 = j\sqrt{k^2 - \xi^2} \tag{C.84}$$

Figure C.2 shows the closed contour for the integrand of $F^{LHP}(\xi)$, where applying Cauchy's integral theorem leads to

$$\begin{aligned} F^{LHP}(\xi) = \oint_C F^{LHP}(\xi, \eta)\, d\eta &= \int_{C_R + C_0^- + C_\infty^-} F^{LHP}(\xi, \eta)\, d\eta \\ &= -2\pi j \sum_i Res_i\left(F^{LHP}(\xi, \eta)\right) \end{aligned} \tag{C.85}$$

The infinite contour integral is evaluated in the same manner as the UHP, where η is allowed to tend to infinity. The hyperbolic sinusoidal terms are then seen to cancel each other and the p term tends to η, giving

$$\int_{C_\infty^-} F^{LHP}(\xi, \eta)\, d\eta = \int_{C_\infty^-} d\eta \frac{e^{-j\eta W_2}}{\eta^2} = 0 \tag{C.86}$$

where again since η is complex and the proper half-plane closure was chosen, the

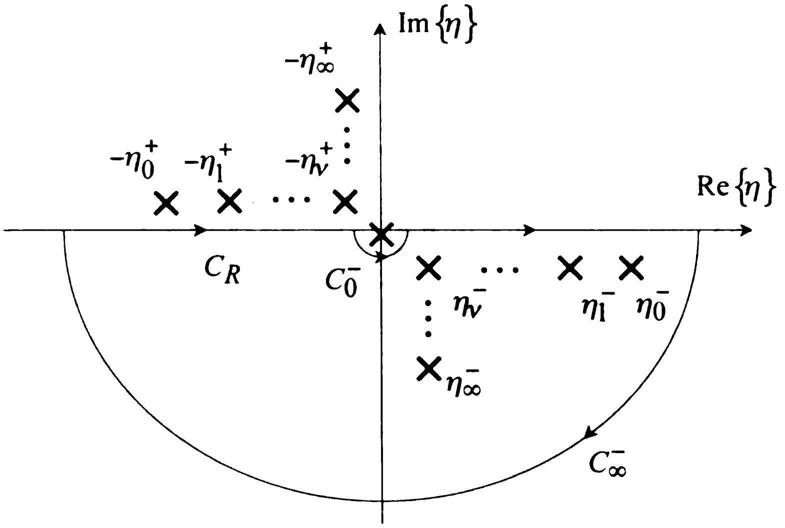

Figure C.2. Evaluation contour for LHP closure in the complex η-plane

exponential term decays, driving the value of the integral to zero.

The contour integral around the pole at $\eta = 0$ is again examined using Cauchy's residue theorem. The semi-circle arc has a positive orientation for the LHP to ensure the desired integral has the proper sign. Since this arc is also only half a circle, the residue is only multiplied by πj instead of $2\pi j$, leading to

$$\int_{C_0^-} F^{LHP}(\xi,\eta)\,d\eta = \pi j\left[Res\left(F^{LHP}(\xi,0)\right)\right] \tag{C.87}$$

where the residue is

$$Res\left(F^{LHP}(\xi,0)\right) = \frac{p_0^{LHP}(\eta=0)}{q_0'^{LHP}(\eta=0)} = -\frac{\cosh(p_0 d)}{p_0\sinh(p_0 d)} \tag{C.88}$$

Substituting the results for (C.85) and (C.87) into (C.84) and rearranging the function to achieve the desired result in terms of the remaining residues, gives

$$\oint_C F^{LHP}(\xi,\eta)\, d\eta = \pi j \left[\frac{\cosh(p_0 d)}{p_0 \sinh(p_0 d)}\right]$$
$$-2\pi j \left[Res\left(F^{LHP}(\xi,\eta_0)\right) + \sum_{\nu=1}^{\infty} Res\left(F^{LHP}(\xi,\eta_\nu)\right)\right] \tag{C.89}$$

where the remaining residues have full circle arcs orientated in the negative direction, thus they are multiplied by $-2\pi j$ and are found as

$$Res\left(F^{LHP}(\xi,\eta_0)\right) = \frac{p_{\eta_0}^{LHP}(\eta=\eta_0)}{q'^{LHP}_{\eta_0}(\eta=\eta_0)} = -\frac{e^{-j\eta_0 W_2}}{\eta_0^2 2d} \tag{C.90}$$

and

$$Res\left(F^{LHP}(\xi,\eta_\nu)\right) = \frac{p_{\eta_\nu}^{LHP}(\eta=\eta_\nu)}{q'^{LHP}_{\eta_\nu}(\eta=\eta_\nu)} = -\frac{e^{-j\eta_\nu W_2}}{\eta_\nu^2 d} \tag{C.91}$$

respectively. Substituting (C.90) and (C.91) into (C.89) yields the final desired result for the LHP as

$$F^{LHP}(\xi) = \pi j \left[\frac{\cosh(p_0 d)}{p_0 \sinh(p_0 d)} + \frac{e^{-j\eta_0 W_2}}{\eta_0^2 d} + \sum_{\nu=1}^{\infty} \frac{2e^{-j\eta_\nu W_2}}{\eta_\nu^2 d}\right] \tag{C.92}$$

Substituting (C.84) and (C.92) into (C.75) and combining like terms gives the following form of the ξ-dependent function

$$F(\xi) = 2\pi j \left[\frac{\cosh(p_0 d)}{p_0 \sinh(p_0 d)} + \frac{e^{-j\eta_0 W_2}}{\eta_0^2 d} + \sum_{\nu=1}^{\infty} \frac{2e^{-j\eta_\nu W_2}}{\eta_\nu^2 d}\right] \tag{C.93}$$

A more compact form of the ξ-dependent function is found by noticing that the middle term of (C.93) is the $\nu = 0$ term of the series in the last term of (C.93). The compact version of the ξ-dependent function is thus written as

$$F(\xi) = 2\pi j \left[\frac{\cosh(p_0 d)}{p_0 \sinh(p_0 d)} + \sum_{\nu=0}^{\infty} \frac{e^{-j\eta_\nu W_2 \epsilon_\nu}}{\eta_\nu^2 d}\right] \tag{C.94}$$

where the Neumann number is defined as

$$\epsilon_\nu = \begin{cases} 1 & for \quad \nu = 0 \\ 2 & for \quad \nu \neq 0 \end{cases} \tag{C.95}$$

The ξ-dependent function in (C.94) is then substituted back into (C.70) giving the parallel-plate admittance matrix elements in terms of only a ξ spectral integral. Splitting the matrix elements into two separate terms gives

$$\begin{aligned} l_{m,n}^{PP3} = & \frac{-j}{\omega\mu 2\pi W_2} \int_{-\infty}^{\infty} d\xi \frac{e^{j\xi\left(x_{2m_2} - x_{2n_2}\right)} \sin\left(\xi \Delta x_2/2\right)\left(\xi^2 - k^2\right)\cosh\left(p_0 d\right)}{\xi\left(\xi^2 - k_0^2\right) p_0 \sinh\left(p_0 d\right)} \\ & \cdot \frac{-j}{\omega\mu 2\pi W_2} \sum_{\nu=0}^{\infty} \epsilon_\nu \int_{-\infty}^{\infty} d\xi \frac{e^{j\xi\left(x_{2m_2} - x_{2n_2}\right)} \sin\left(\xi \Delta x_2/2\right)\left(\xi^2 - k^2\right) e^{-j\eta_\nu W_2}}{\xi\left(\xi^2 - k_0^2\right) \eta_\nu^2 d} \end{aligned} \tag{C.96}$$

Solving the ξ integrals in closed form would be the most advantageous computationally. However, if that is unfeasible to attain, then solving the integral numerically is the only option. In the case of (C.96) only the first term is able to be solved in closed form, because the second term has a branch cut due to the multi-valued η_ν term. The parallel-plate admittance matrix elements are thus redefined in terms of two functions as

$$l_{m,n}^{PP3} = \frac{-j}{\omega\mu 2\pi W_2} \left\{ \frac{1}{2j} F_1 + \frac{2}{d} \sum_{\nu=0}^{\infty} \epsilon_\nu F_2 \right\} \tag{C.97}$$

where F_1 corresponds to the first term in (C.96) and is evaluated in the next section. After expanding the sine function in terms of exponentials and simplifying the function, F_1 is given as

$$F_1 = \int_{-\infty}^{\infty} d\xi \frac{\left(e^{j\xi A} - e^{j\xi B}\right) p_0 \cosh\left(p_0 d\right)}{\xi\left(\xi^2 - k_0^2\right) \sinh\left(p_0 d\right)} \tag{C.98}$$

F_2 corresponds to the second term in (C.96) and is solved numerically, where noticing that the function is even in ξ and is written as

$$F_2 = \int_0^\infty d\xi \frac{\cos\left[\xi\left(x_{2_{m_2}} - x_{2_{n_2}}\right)\right]\sin\left(\xi\Delta x_2/2\right)\left(\xi^2 - k^2\right)e^{-j\eta_\nu W_2}}{\xi\left(\xi^2 - k_0^2\right)\eta_\nu^2} \tag{C.99}$$

thus simplifying the necessary compuatations. Other definitions include

$$\eta_\nu^2 = p_\nu^2 + k^2 - \xi^2 \quad ; \quad p_\nu = \frac{j\nu\pi}{d} \quad ; \quad p_0 = j\sqrt{k^2 - \xi^2} \tag{C.100}$$

and

$$\begin{aligned} A &= \left(x_{2_{m_2}} - x_{2_{n_2}} + \Delta x_2/2\right) = \Delta x_2\left(m - n + 1/2\right) \\ B &= \left(x_{2_{m_2}} - x_{2_{n_2}} - \Delta x_2/2\right) = \Delta x_2\left(m - n - 1/2\right) \end{aligned} \tag{C.101}$$

C.4.1.2 ξ Analysis

The ξ spectral integral analysis of (C.98) is carried out in almost exactly the same manner as the η spectral integral analysis of the last section. Splitting the integrand into two separate terms gives

$$F_1 = \int_{-\infty}^{\infty} d\xi \frac{e^{j\xi A}p_0\cosh\left(p_0 d\right)}{\xi\left(\xi^2 - k_0^2\right)\sinh\left(p_0 d\right)} - \int_{-\infty}^{\infty} d\xi \frac{e^{j\xi B}p_0\cosh\left(p_0 d\right)}{\xi\left(\xi^2 - k_0^2\right)\sinh\left(p_0 d\right)} \tag{C.102}$$

where depending on matrix element being filled, the upper or lower half-plane closure is defined for the first term as

$$\begin{aligned} A &= \Delta x\left(m - n + 1/2\right) \\ &= \begin{cases} > 0 \quad \forall \quad m \geq n \quad \therefore \quad UHP \quad Closure \\ < 0 \quad \forall \quad m < n \quad \therefore \quad LHP \quad Closure \end{cases} \end{aligned} \tag{C.103}$$

and for the second term as

$$\begin{aligned} B &= \Delta x \left(m - n - 1/2\right) \\ &= \begin{cases} > 0 \quad \forall \quad m > n \quad \therefore \quad UHP \quad Closure \\ < 0 \quad \forall \quad m \leq n \quad \therefore \quad LHP \quad Closure \end{cases} \end{aligned} \tag{C.104}$$

This leads to three different closure cases for the function F_1 given as

$$F_1\left(m > n\right) = F_{1_A}^{UHP} - F_{1_B}^{UHP} \tag{C.105}$$

$$F_1\left(m = n\right) = F_{1_A}^{UHP} - F_{1_B}^{LHP} \tag{C.106}$$

$$F_1\left(m < n\right) = F_{1_A}^{LHP} - F_{1_B}^{LHP} \tag{C.107}$$

Both the first and second terms have the need for upper and lower half-plane closure. Since they have the same integrand, except for the terms A and B, new functions in terms of a dummy variable (DV) are defined as

$$F_{1_{DV}}^{UHP} = \int_{-\infty}^{\infty} d\xi \frac{e^{j\xi(DV)} p_0 \cosh\left(p_0 d\right)}{\xi\left(\xi^2 - k_0^2\right)\sinh\left(p_0 d\right)} \tag{C.108}$$

and

$$F_{1_{DV}}^{LHP} = \int_{-\infty}^{\infty} d\xi \frac{e^{j\xi(-DV)} p_0 \cosh\left(p_0 d\right)}{\xi\left(\xi^2 - k_0^2\right)\sinh\left(p_0 d\right)} \tag{C.109}$$

for the upper and lower half-plane closure respectively. This is done so that the complex plane analysis only has to be calculated once instead of multiple times. The desired F_1 functions are then created by substituting in the appropriate term for the dummy variable.

Figure C.3 shows the closed contour for the integrand of $F_{1_{DV}}^{UHP}$, where applying

Cauchy's integral theorem leads to

$$
\begin{aligned}
F^{UHP}_{1_{DV}} = \oint_C d\xi F^{UHP}_{1_{DV}}(\xi) &= \int_{C_R+C_0^+ + C_\infty^+} F^{UHP}_{1_{DV}}(\xi)\, d\xi \\
&= 2\pi j \sum_i Res_i \left(F^{UHP}_{1_{DV}}(\xi) \right)
\end{aligned}
\tag{C.110}
$$

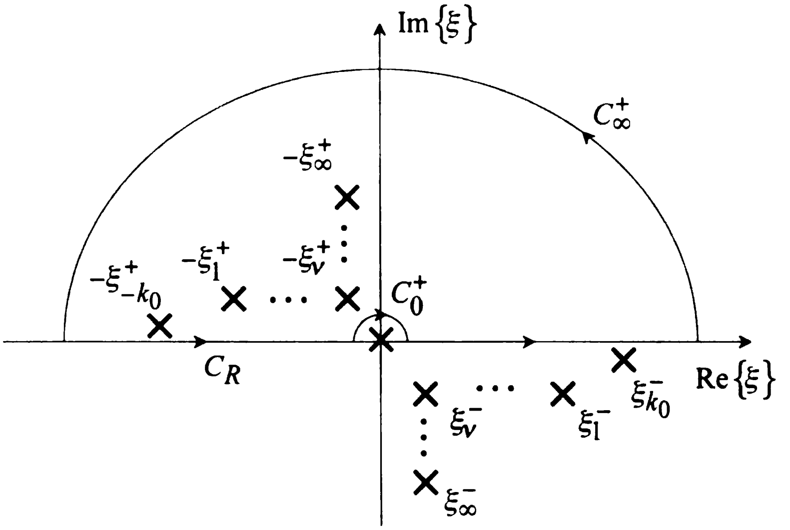

Figure C.3. Evaluation contour for UHP closure in the complex ξ-plane

The infinite contour integral is examined, through inspection, by letting ξ tend to infinity. The hyperbolic sinusoidal terms are seen to cancel each other and the p_0 term tends to ξ, giving

$$
\int_{C_\infty^+} F^{UHP}_{1_{DV}}(\xi)\, d\xi = \int_{C_\infty^+} d\xi \frac{e^{j\xi(DV)}}{\xi^2} = 0 \tag{C.111}
$$

where since ξ is complex and proper half-plane closure has been chosen, the exponential term decays, driving the value of the integral to zero.

The contour integral around the pole at $\xi = 0$ is examined using Cauchy's residue theorem. The semi-circle arc has a negative orientation to ensure the desired integral has the proper sign. Since the arc in only half a circle, the residue is only multiplied by $-\pi j$ instead of $-2\pi j$, leading to

$$\int_{C_0^+} F_{1_{DV}}^{UHP}(\xi)\, d\xi = -\pi j \left[Res\left(F_{1_{DV}}^{UHP}(0)\right)\right] \tag{C.112}$$

where the residue is

$$Res\left(F_{1_{DV}}^{UHP}(0)\right) = \frac{p_0^{UHP}(\xi = 0)}{q_0'^{UHP}(\xi = 0)} = -\frac{k\cos(kd)}{k_0^2 \sin(kd)} \tag{C.113}$$

Substituting the results for (C.111) and (C.113) into (C.110) and rearranging the function to achieve the desired result in terms of the remaining residues, gives

$$\begin{aligned} F_{1_{DV}}^{UHP} = \pi j \left[-\frac{k\cos(kd)}{k_0^2 \sin(kd)} \right] &+ 2\pi j \left[Res\left(F_{1_{DV}}^{UHP}(-k_0)\right) \right. \\ &\left. + \sum_{v=1}^{\infty} Res\left(F_{1_{DV}}^{UHP}(-\xi_v)\right) \right] \end{aligned} \tag{C.114}$$

where the remaining residues have full circle arcs orientated in the positive direction, thus they are multiplied by $2\pi j$ and are found as

$$Res\left(F_{1_{DV}}^{UHP}(-k_0)\right) = \frac{p_{-k_0}^{UHP}(\xi = -k_0)}{q'^{UHP}_{-k_0}(\xi = -k_0)} = \frac{e^{-jk_0(DV)}\overline{k}\cos\left(\overline{k}d\right)}{2k_0^2 \sin\left(\overline{k}d\right)} \tag{C.115}$$

and

$$Res\left(F_{1_{DV}}^{UHP}(-\xi_v)\right) = \frac{p_{-\xi_v}^{UHP}(\xi = -\xi_v)}{q'^{UHP}_{-\xi_v}(\xi = -\xi_v)} = \frac{e^{-j\xi_v(DV)} p_{0_v}^2}{\xi_v^2 \left(\xi_v^2 - k_0^2\right) d} \tag{C.116}$$

respectively. Substituting (C.115) and (C.116) into (C.114) yields the final desired

result as

$$F_{1_{DV}}^{UHP} = \pi j \left[-\frac{k\cos(kd)}{k_0^2 \sin(kd)} + \frac{e^{-jk_0(DV)}\bar{k}\cos\left(\bar{k}d\right)}{k_0^2 \sin\left(\bar{k}d\right)} + \sum_{v=1}^{\infty} \frac{e^{-j\xi_v(DV)}p_{0_v}^2}{\xi_v^2\left(\xi_v^2 - k_0^2\right)d} \right] \quad \text{(C.117)}$$

where

$$\xi_v^2 = p_{0_v}^2 + k^2 \quad ; \quad p_{0_v} = \frac{jv\pi}{d} \quad ; \quad \bar{k} = \sqrt{k^2 - k_0^2} \qquad \text{(C.118)}$$

Figure C.4 shows the closed contour for the integrand of $F_{1_{DV}}^{LHP}$, where applying Cauchy's integral theorem leads to

$$\begin{aligned} F_{1_{DV}}^{LHP} = \oint_C d\xi F_{1_{DV}}^{LHP}(\xi) &= \int_{C_R + C_0^- + C_\infty^-} F_{1_{DV}}^{LHP}(\xi)\, d\xi \\ &= -2\pi j \sum_i Res_i\left(F_{1_{DV}}^{LHP}(\xi)\right) \end{aligned} \qquad \text{(C.119)}$$

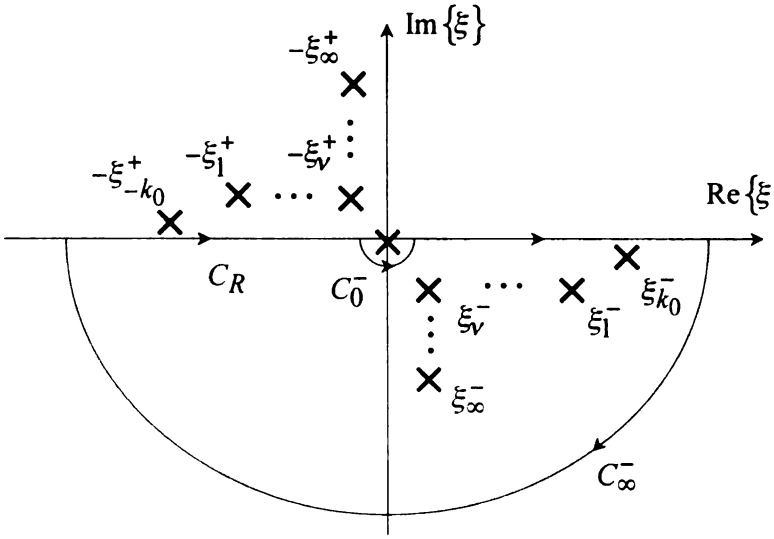

Figure C.4. Evaluation contour for LHP closure in the complex ξ-plane

The infinite contour integral is examined, through inspection, by letting ξ tend to infinity. The hyperbolic sinusoidal terms are seen to cancel each other and the p_0 term tends to ξ, giving

$$\int_{C_\infty^-} F_{1_{DV}}^{LHP}(\xi)\,d\xi = \int_{C_\infty^-} d\xi\,\frac{e^{j\xi(-DV)}}{\xi^2} = 0 \tag{C.120}$$

where since ξ is complex and proper half-plane closure has been chosen, the exponential term decays, driving the value of the integral to zero.

The contour integral around the pole at $\xi = 0$ is examined using Cauchy's residue theorem. The semi-circle arc a positive orientation to ensure the desired integral has the proper sign. Since the arc in only half a circle, the residue is only multiplied by πj instead of $2\pi j$, leading to

$$\int_{C_0^-} F_{1_{DV}}^{LHP}(\xi)\,d\xi = \pi j\left[Res\left(F_{1_{DV}}^{LHP}(0)\right)\right] \tag{C.121}$$

where the residue is

$$Res\left(F_{1_{DV}}^{LHP}(0)\right) = \frac{p_0^{LHP}(\xi = 0)}{q'^{LHP}_0(\xi = 0)} = -\frac{k\cos(kd)}{k_0^2\sin(kd)} \tag{C.122}$$

Substituting the results for (C.120) and (C.122) into (C.119) and rearranging the function to achieve the desired result in terms of the remaining residues, gives

$$\begin{aligned} F_{1_{DV}}^{LHP} = -\pi j\left[-\frac{k\cos(kd)}{k_0^2\sin(kd)}\right] - 2\pi j\Bigg[Res\left(F_{1_{DV}}^{LHP}(k_0)\right) \\ + \sum_{v=1}^{\infty} Res\left(F_{1_{DV}}^{LHP}(\xi_v)\right)\Bigg] \end{aligned} \tag{C.123}$$

where the remaining residues have full circle arcs orientated in the negative direction, thus they are multiplied by $-2\pi j$ and are found as

$$Res\left(F_{1_{DV}}^{LHP}(k_0)\right) = \frac{p_{k_0}^{LHP}(\xi = k_0)}{q'^{LHP}_{k_0}(\xi = k_0)} = \frac{e^{jk_0(-DV)}\bar{k}\cos\left(\bar{k}d\right)}{2k_0^2\sin\left(\bar{k}d\right)} \tag{C.124}$$

and

$$Res\left(F_{1_{DV}}^{LHP}(\xi_v)\right) = \frac{p_{\xi_v}^{LHP}(\xi = \xi_v)}{q'^{LHP}_{\xi_v}(\xi = \xi_v)} = \frac{e^{j\xi_v(-DV)}p_{0_v}^2}{\xi_v^2\left(\xi_v^2 - k_0^2\right)d} \tag{C.125}$$

respectively. Substituting (C.124) and (C.125) into (C.123) yields the final desired result as

$$F_{1_{DV}}^{LHP} = -\pi j\left[-\frac{k\cos(kd)}{k_0^2\sin(kd)} + \frac{e^{jk_0(-DV)}\bar{k}\cos\left(\bar{k}d\right)}{k_0^2\sin\left(\bar{k}d\right)} + \sum_{v=1}^{\infty}\frac{2e^{j\xi_v(-DV)}p_{0_v}^2}{\xi_v^2\left(\xi_v^2 - k_0^2\right)d}\right] \tag{C.126}$$

Substituting the results from (C.117) and (C.126), with the appropriate A, B term replacing the dummy variable, into equations (C.105-C.107) respectively, leads to the following set of three distinct groups of F_1 functions

$$\begin{aligned} F_1(m > n) = {} & \frac{2\pi j}{d}\sum_{v=1}^{\infty}\frac{p_{0_v}^2\left[e^{-j\xi_v A} - e^{-j\xi_v B}\right]}{\xi_v^2\left(\xi_v^2 - k_0^2\right)} \\ & +\pi j\frac{\bar{k}\cos\left(\bar{k}d\right)\left[e^{-jk_0 A} - e^{-jk_0 B}\right]}{k_0^2\sin\left(\bar{k}d\right)} \end{aligned} \tag{C.127}$$

$$\begin{aligned} F_1(m = n) = {} & \frac{2\pi j}{d}\sum_{v=1}^{\infty}\frac{p_{0_v}^2\left[e^{-j\xi_v A} + e^{j\xi_v B}\right]}{\xi_v^2\left(\xi_v^2 - k_0^2\right)} \\ & +\pi j\frac{\bar{k}\cos\left(\bar{k}d\right)\left[e^{-jk_0 A} + e^{jk_0 B}\right]}{k_0^2\sin\left(\bar{k}d\right)} - 2\pi j\frac{k\cos(kd)}{k_0^2\sin(kd)} \end{aligned} \tag{C.128}$$

$$F_1\left(m<n\right)=\frac{2\pi j}{d}\sum_{v=1}^{\infty}\frac{p_{0_v}^2\left[-e^{j\xi_v A}+e^{j\xi_v B}\right]}{\xi_v^2\left(\xi_v^2-k_0^2\right)} +\pi j\frac{\bar{k}\cos\left(\bar{k}d\right)\left[-e^{jk_0 A}+e^{jk_0 B}\right]}{k_0^2\sin\left(\bar{k}d\right)} \tag{C.129}$$

Substituting (C.127-C.129) into (C.97) and rearranging the terms leads to the final representation of the parallel-plate admittance matrix elements, given as

$$l_{m,n}^{PP3}=l_{m,n_{PP}}^{1}+l_{m,n_{PP}}^{2}+l_{m,n_{PP}}^{3} \tag{C.130}$$

where the first and second terms given as

$$l_{m,n_{PP}}^{1}=\frac{-j}{\omega\mu 4W_2}\left[\sum_{v=1}^{\infty}\frac{2p_{0_v}^2 F_1^{exp1}}{\xi_v^2\left(\xi_v^2-k_0^2\right)d}+\frac{\bar{k}\cos\left(\bar{k}d\right)F_1^{exp2}}{k_0^2\sin\left(\bar{k}d\right)}\right] \tag{C.131}$$

and

$$l_{m,n_{PP}}^{2}=\frac{jk\cos\left(kd\right)}{\omega\mu 2W_2 k_0^2\sin\left(kd\right)}\quad for\quad m=n \tag{C.132}$$

respectively, are associated with the F_1 function and the third term, given as

$$l_{m,n_{PP}}^{3}=\frac{-j}{\omega\mu\pi W_2 d}\sum_{\nu=0}^{\infty}\epsilon_\nu \cdot\int_0^{\infty}d\xi\frac{\cos\left[\xi\left(x_{2_{m_2}}-x_{2_{n_2}}\right)\right]\sin\left(\xi\triangle x_2/2\right)\left(\xi^2-k^2\right)e^{-j\eta_\nu W_2}}{\xi\left(\xi^2-k_0^2\right)\eta_\nu^2} \tag{C.133}$$

is associated with the F_2 function. Other definitions include

$$F_1^{exp1}=\begin{cases}\left[e^{-j\xi_v A}-e^{-j\xi_v B}\right] & for\quad m>n\\ \left[e^{-j\xi_v A}+e^{j\xi_v B}\right] & for\quad m=n\\ \left[-e^{j\xi_v A}+e^{j\xi_v B}\right] & for\quad m<n\end{cases} \tag{C.134}$$

and

$$F_1^{exp2} = \begin{cases} \left[e^{-jk_0 A} - e^{-jk_0 B}\right] & for \quad m > n \\ \left[e^{-jk_0 A} + e^{jk_0 B}\right] & for \quad m = n \\ \left[-e^{jk_0 A} + e^{jk_0 B}\right] & for \quad m < n \end{cases} \tag{C.135}$$

where the terms A, B are given as

$$\begin{aligned} A &= \triangle x \left(m - n + 1/2\right) \\ B &= \triangle x \left(m - n - 1/2\right) \end{aligned} \tag{C.136}$$

and the various spectral constants are

$$\xi_v^2 = p_{0_v}^2 + k^2 \quad ; \quad p_{0_v} = \frac{jv\pi}{d} \quad ; \quad \xi_v = -j\sqrt{-\left(\xi_v^2\right)} \tag{C.137}$$

$$\eta_\nu^2 = p_\nu^2 + k^2 - \xi^2 \quad ; \quad p_\nu = \frac{j\nu\pi}{d} \quad ; \quad \eta_\nu = -j\sqrt{-\left(\eta_\nu^2\right)} \tag{C.138}$$

$$\overline{k}^2 = k^2 - k_0^2 \quad ; \quad \overline{k} = \sqrt{k^2 - k_0^2} \tag{C.139}$$

with the Neumann number given as

$$\epsilon_\nu = \begin{cases} 1 & for \quad \nu = 0 \\ 2 & for \quad \nu \neq 0 \end{cases} \tag{C.140}$$

BIBLIOGRAPHY

BIBLIOGRAPHY

[1] W. Williams, and K. O'Malley, "A lightweight composite shielding material for electromagnetic gun launchers," *Magnetics, IEEE Transactions on*, vol. 33, no. 1, pp. 625-629, Jan. 1997.

[2] D. C. Smith, C. Herring, and R. Haynes, "An improved method of characterizing shielding materials," *Electromagnetic Compatibility, 1994. Symposium Record. Compatibility in the Loop. IEEE International Symposium on,* pp. 224-226, Aug. 1994.

[3] P. F. Wilson, J. W. Adams, and M. T. Ma, "Measurement o the electromagnetic shielding capabilities of materials," *Proceedings of the IEEE,* vol. 74, no. 1, pp. 112-115, Jan. 1986.

[4] S. O. Nelson, S. Trabelsi, and S. J. Kays, "Correlating Dielectric Properties of Melons with Quality," *2006 APS International Symposium-URSI Meetings, Albuquerque, NM*, Session 564.6, Paper 4849, 2006.

[5] A. M. Nicolson, and G. F. Ross, "Measurement of the Intrinsic Properties of Materials by Time-Domain Techniques," *IEEE Trans. Instrum. Meas.,* vol. IM-19, pp. 377-382, Nov. 1970.

[6] W. B. Weir, "Automatic Measurement of Complex Dielectric Constant and Permeability at Microwave Frequencies," *Proc. IEEE,* vol. 62, pp. 33-36, Jan. 1974.

[7] M. J. Havrilla, *Analytical and Experimental Techniques for the Electromagnetic Characterization of Materials,* Doctoral Dissertation, Michigan State University, 2001.

[8] K. Vinoy, and R. Jha, *Radar Absorbing Materials: From Theory to Design and Characterization,* Norwell, MA: Kluwer Academic Publishers, 1996.

[9] R. Zoughi, *Microwave Non-Destructive Testing and Evaluation,* The Netherlands: Kluwer Academic Publishers, 2000.

[10] B. Clarke, ed., *A Guide to the Characterization of Dielectric Materials at RF and Microwave Frequencies,* London: Institute of Measurement and Control, 2003.

[11] L. Chen, C. Ong, C. Neo, and V. Varadan, eds., *Microwave Electronics: Measurement and Materials Characterization,* Hoboken, NJ: John Wiley and Sons, 2004.

[12] C. Grosvenor, R. Johnk, D. Novotny, S. Canales, J. Baker-Jarvis, M. Janezic, J. Drewniak, M. Koledintseva, J. Zhang, and P. Rawa, "Electrical material property measurements using a free-field, ultra-wideband system," *2004 Annual Report Conference on Electrical Insulation and Dielectric Phenomena (CEIDP),* pp. 174-177, Oct. 2004.

[13] F. Smith, B. Chambers, and J. Bennet, "Methodology for accurate free-space characterization of radar absorbing materials," *IEE Proceedings on Scientific Measurement Technology,* vol. 141, pp. 538-546, Nov. 1994.

[14] R. G. Nitsche, J. Preifner, and E. M. Biebl, "A free space technique for measuring the complex permittivity and permeability in the millimeter wave range," *IEEE MTT-S Digest,* pp. 1465-1468, 1994.

[15] D. Ghodgaonkar, V. Varadan, and V. Varadan, "Free-space measurement of complex permittivity and complex permeability of magnetic materials at microwave frequencies," *IEEE Transactions on Instrumentation and Measurement,* vol. 39, pp. 387-394, Apr. 1990.

[16] H. Alenkowicz, and B. Levitas, "Measurement of complex permittivity and complex permeability of materials," *Microwaves and Radar, MIKON '98., 12th International Conference on* vol. 2, pp. 668-672, May 1998.

[17] H. Alenkowicz, and B. Levitas, "Time domain measurement of complex permittivity and complex permeability of materials," *Microwaves, Radar and Wireless Communications, MIKON '02., 14th International Conference on* vol. 1, pp. 302-305, 2002.

[18] C. L. Pournaropoulos, and D. Misra, "A study on the coaxial aperture electromagnetic sensor and its application in the material characterization," *IEEE Transactions on Instrumentation and Measurement,* vol. 43, no. 2, pp. 111-115, 1994.

[19] NASA-95-TM110147, "Capabilities to measure the dielectric properities of materials," *Electromagnetic Properties Measurement Laboratory (EPML),* 1995.

[20] C. -L. Li, and K. -M. Chen, "Determination of electromagnetic properties of materials using flanged open-ended coaxial probe full-wave analysis," *IEEE Transactions on Instrumentation and Measurement,* vol. 44, pp. 19-27, Feb. 1995.

[21] W. R. Scott Jr., "A new technique for measuring the constitutive parameters of planar materials," *IEEE Transactions on Instrumentation and Measurement*, vol. 41, no. 5, pp. 639-645, 1992.

[22] J. Baker-Jarvis, and M. D. Janezic, "Analysis of a two-port flanged coaxial holder for shielding effectiveness and dielectric measurements of thin films and thin materials," *IEEE Transactions on Electromagnetic Compatibility,* vol. 38, pp. 67-70, Feb. 1996.

[23] S. I. Ganchev, "Non-destructive microwave measurements of dielectric materials," *Microwaves and Radar, 1998. MIKON '98., 12th International Conference on,* vol. 3, pp. 687-691, May 1998.

[24] O. Tantot, M. Chantart-Moulin, and P. Guillon, "Measurement of complex permittivity and permeability and thickness of multilayered medium by an open-ended waveguide method," *IEEE Transactions on Microwave Theory and Techniques,* vol. 46, pp. 519-522, Apr. 1997.

[25] J. Villemazet, M. Chatard-Moulin, P. Guillon, and H. Jallageas, "Non-destructive complex permittivity measurement of absorbing materials," *IEEE Conference on Instrumentation and Measurement, Conference Record,* pp. 232-235, 1991.

[26] M. C. Decreton, and F. E. Gardiol, "Reflection form a metallic or dielectric sheet into an open-ended waveguide," *IEEE Transactions on Antennas and Propagation,* pp. 362-365, Oct. 1976.

[27] T. J. Park, and H. J. Eom, "Scattering and reception by a flanged parallel-plate waveguide: TE-mode analysis," *IEEE Transactions on Microwave Theory and Techniques,* vol. 41, pp. 1458-1460, Aug. 1993.

[28] S. I. Ganchev, S. Bakhtiari, and R. Zoughi, "A novel numerical technique for dielectric measurement of general lossy dielectrics," *IEEE Transactions on Instrumentation and Measurement,* vol. 41, pp. 361-365, Jun. 1992.

[29] S. Bakhtiari, S. I. Ganchev, and R. Zoughi, "Open-ended rectangular waveguide for non-destructive thickness measurement and variation detection of lossy dielectric slabs backed by a conducting plate," *IEEE Transactions on Instrumentation and Measurement,* vol. 42, pp. 19-24, Feb. 1993.

[30] L. Cairo, and T. Kahan, eds., *Variational Techniques in Electomagnetism,* New York: Gordon and Breach, 1965.

[31] J. A. Encinar, and J. M. Rebollar, "Convergence of numerical solutions of open-ended waveguide by modal analysis and hybrid modal-spectral techniques," *IEEE Tranactions on Microwave Theory and Techniques*, vol. 34, pp. 809-814, Jul. 1986.

[32] Z. Shen, and R. H. MacPhie, "A simple method for calculating the reflection coefficient of open-ended waveguides," *IEEE Transactions on Microwave Theory and Techniques*, vol. 45, pp. 546-548, Apr. 1997.

[33] V. Teodoridis, T. Sphicopoulos, and F. E. Gardiol, "The reflection from an open-ended rectangular waveguide terminated by a layered dielectric medium," *IEEE Transactions on Microwave Theory and Techniques*, vol. 33, pp. 359-366, May 1985.

[34] C. -W. Chang, K. -M. Chen, and J. Qian, "Non-destructive measurements of complex tensor permittivity of anisotropic materials using a waveguide probe system," *IEEE Transactions on Microwave Theory and Techniques*, vol. 44, pp. 1081-1090, Jul. 1996.

[35] C. -W. Chang, K. -M. Chen, and J. Qian, "Non-destructive determination of electromagnetic parameters of dielectric materials at X-band frequencies using a waveguide probe system," *IEEE Transactions on Instrumentation and Measurement*, vol. 46, pp. 1084-1092, Oct. 1997.

[36] K. J. Bois, A. D. Benally, and R. Zoughi, "Multimode solution for the reflection properties of an open-ended rectangular waveguide radiating into a dielectric half-space: The forward and inverse problem," *IEEE Transactions on Instrumentation and Measurement,* vol. 48, pp. 1131-1140, Dec. 1999.

[37] G. Roussy, H. Chaabane, and H. Esteban, "Permittivity and permeability measurement of microwave packaging materials," *IEEE Transactions on Microwave Theory and Techniques,* vol. 52, pp. 903-907, Mar. 2004.

[38] J. Lai, D. Hughes, E. Gallaher, and R. Zoughi, "Determination of the thickness and dielectric constant of a dielectric slab backed by free-space or a conductor through inversion of the reflection coefficient of a rectangular waveguide probe," *IMTC 2004 - Instrumentation and Measurement Technology Conference*, pp. 56-60, May 2004.

[39] S. Wang, M. Niu, and d. Xu, "A frequency-varying method for simultaneous measurement of complex permittivity and permeability with an open-ended coaxial

probe," *IEEE Transactions on Microwave Theory and Techniques*, vol. 46, pp. 2145-2147, Dec. 1998.

[40] J. Baker-Jarvis, M. D. Janezic, P. D. Domich, and R. G. Geyer, "Analysis of an open-ended coaxial probe with lift-off for non-destructive testing," *IEEE Transactions on Instrumentation and Measurement*, vol. 43, pp. 711-718, Oct. 1994.

[41] J. W. Stewart, *Simultaneous Extraction of the Permittivity and Permeability of Conductor-Backed Lossy Materials Using Open-Ended Waveguide Probes*, Doctoral Dissertation, Air Force Institute of Technology, 2006.

[42] R. J. Mailloux, "Radiation and near-field coupling between two collinear open-ended waveguides," *IEEE Transactions on Antennas and Propagation*, vol. 17, pp. 476-481, Apr. 1999.

[43] T. S. Bird, "Analysis of mutual coupling in finite arrays of different-sized rectangular waveguide," *IEEE Transactions on Antennas and Propagation*, vol. 38, pp. 166-172, Feb. 1990.

[44] T. S. Bird, "Cross-coupling between open-ended coaxial radiators," *IEE Proceedings on Microwave, Antennas and Propagation*, vol. 143, pp. 265-271, Aug. 1996.

[45] T. S. Bird, "Mutual coupling in arrays of coaxial waveguides and horns," *IEEE Transactions on Antennas and Propagation*, vol. 52, pp. 821-829, Mar. 2004.

[46] A. F. Stevenson, "Theory of slots in rectangular waveguides," *J. Appl. Phys.*, vol. 19, pp. 24-38, Jan. 1948.

[47] A. A. Oliner, "The impedance properties of narrow radiating slots in the broad face of rectangular waveguide, Part I - Theory, Part II - Comparison with Measurement," *IRE Trans. Antennas Propagat.*, vol. AP-5, pp. 4-20, Jan. 1957.

[48] L. Josefsson, "A waveguide transverse slot for array applications," *IEEE Trans. Antennas Propagat.*, vol. AP-41, pp. 845-850, July 1993.

[49] L. Josefsson, "Analysis of longitudinal slots in rectangular waveguides," *IEEE Trans. Antennas Propagat.*, vol. 35, pp. 1351-1357, Dec. 1987.

[50] J. Joubert and J. A. G. Malherbe, "Moment method calculation of the propagation constant for leaky-wave modes in slotted rectangular waveguide," *IEE Proceedings - Microwaves, Antennas and Propagation*, vol. 146, pp. 411-415, Dec 1999.

[51] J. Jacobs, J. Joubert, and J. W. Odendaal, "Radiation efficiency of broadside conductor-backed CPW-fed twin slot antennas on two-layer dielectric substrate," *IEEE AFRICON - Africon Conference in Africa*, vol. 2, pp. 531-533, Oct. 2002.

[52] J. Joubert, "A transverse slot in the broad wall of inhomogeneously loaded rectangular waveguide for array applications," *IEEE Microwave and Guided Wave Letters*, vol. 5, pp. 37-39, Feb. 1995.

[53] J. Joubert and D. A. McNamara, "Analysis of radiating slots in a rectangular waveguide inhomogeneously loaded with a dielectric slab," *IEEE Transactions on Antennas and Propagation*, vol. 41, pp. 1212-1221, Sept. 1993.

[54] V. V. S. Prakash, S. Christopher and N. Balakrishnan, "Method-of-moments analysis of the narrow-wall slot array in a rectangular waveguide," *IEE Proceedings on Microwaves, Antennas and Propagation*, vol. 147, pp. 242-246, June 2000.

[55] S. Silver, *Microwave Antenna Theory and Design* (MIT Rad. Lab. Series, vol. 12) New York: McGraw-Hill, 1949, p. 286-301

[56] R. S. Elliott, *Antenna Theory and Design,* Englewood Cliffs, N.J.: 1981.

[57] E. J. Rothwell, and M. J. Cloud, *Electromagnetics,* Boca Raton, FL: 2001.

[58] R. F. Harrington, *Time-Harmonic Electromagnetic Fields,* New York: McGraw-Hill, 1961.

[59] W. E. Boyce, and R. C. Diprima, *Elementary Differential Equations,* New York, John Wiley and Sons, 1986.

[60] D. P. Nyquist, *ECE929B Advanced Topics in Electromagnetics; Antenna Theory,* Course Notes, Michigan State University, 1989.

[61] C. T. Tai, *Dyadic Green's Functions in Electromagnetic Theory,* 2nd ed. Piscataway, NJ: IEEE Press, 1994.

[62] R. E. Collin, *Field Theory of Guided Waves,* 2nd ed. Piscataway, NJ: IEEE Press, 1991.

[63] C. T. Tai; P. Rozenfeld, "Different Representations of Dyadic Green's Functions for a Rectangular Cavity," *IEEE Trans. Microwave Theory and Techniques,* Vol.24, Iss.9, Sep 1976, Pages: 597- 601

[64] J. W. Brown, and R. V. Churchill, *Complex Variables and Applications*, 6th ed. New York, McGraw-Hill, 1996.

[65] G. F. Engen, and C. A. Hoer, "Thru-Reflect-Line: An Improved Technique for Calibrating the Dual Six-Port Automatic Network Analyzer," *IEEE Trans. Microwave Theory and Techniques*, 1979.

[66] M. Microwave, "TRL Calibration Defined," vol. 2004: Maury Microwave.

[67] A. Technologies, "Agilent Specifying Calibration Standards for the Agilent 8510 Network Analyzer," March 1986.

[68] A. E. Bogle, *Electromagnetic Material Characterization using a Partially Filled Rectangular Waveguide*, Masters Thesis, Michigan State University, 2004.

[69] J. A. Berrie, *Measurement of Electrical Parameters for Planar Materials*, Dissertation, The Ohio State University, 1992.

[70] P. De Langhe, K. Blomme, L. Martens, and D. De Zutter, "Measurement of low-permittivity materials based on a spectral-domain analysis for the open-ended coaxial probe," *IEEE Transactions on Instrumentation and Measurement*, vol. 42, no. 5, pp. 879-886, Oct 1993.

[71] D. Zwillinger, *CRC Standard Mathematical Tables and Formulae*, 31st ed. New York, Chapman and Hall/CRC, 2003.